714

TABLE OF CONTENTS

INTRODUCTION

The conference whose minutes are reported in this volume was the fourth in a series, previous conferences having been held in 1961 and 1962 at Brookhaven National Laboratory and in 1963 at Yale University. These conferences have been informal in nature, stressing primarily the progress made in the design of proton linear accelerators. This conference was sponsored by the Midwestern Universities Research Association and supported by the U. S. Atomic Energy Commission.

The interest in these conferences has grown appreciably, as evidenced by the increased participation and number of contributions. Starting from 20 participants and 17 contributions in 1961, we have reached a level of 96 participants and 54 contributions. The participants at this conference represented 24 institutions coming from seven different countries. Even with this size, it was possible to preserve informality and to allow speakers sufficient time to make their presentations and to hold adequate discussion. Fortunately, it was not necessary to turn away any worthy contribution or to hold concurrent sessions.

The conference was held at an especially opportune time for linac enthusiasts. In the U. S. there were three proposals for construction of linacs of energy 200 MeV or greater, these being the 500 MeV injector for the AGS at Brookhaven National Laboratory, the 200 MeV injector for the ZGS at Argonne National Laboratory, and the 800 MeV meson factory at Los Alamos Scientific Laboratory. On the foreign scene, there are plans for meson factories at Strasbourg and Karlsruhe, a new injector for the PS at CERN, and plans for an injector for a high energy AGS (Jupiter) at Saclay. Within the U. S., design studies of linacs have been closely coordinated under the auspices of the AEC by the Linac Coordination Committee. This conference gave the working members of the design teams a chance to interact freely.

The new linacs being designed require increased beam current and pulse length. This has spurred interest in beam loading phenomena and improved design of preinjectors. Much progress was reported at the conference in those areas but neither has yet arrived at a satisfactory state. For linacs whose energy is greater than 200 MeV the question of choice of rf structure remains unresolved although considerable progress has been reported. Renewed interest in the design of superconducting linacs was in evidence, particularly as reported from Karlsruhe.

We would like to take this opportunity to thank the many people, both MURA staff members and visitors, who helped make the conference run smoothly. We would particularly like to thank Lloyd Smith, Rolland Perry, Keith Symon, John O'Meara, Jim Leiss, George Wheeler, and John Blewett who assisted by serving as session chairmen.

F. E. Mills

LIST OF PARTICIPANTS

Argonne National Laboratory

Abraham, J.
Castor, R. W.
Goodrich, R. R.
Livdahl, P. V.
Martin, J. H.
Myers, W. W.
Nordby, D. H.
Perry, R.
Rihel, R. K.
Teng, L. C.

Atomic Energy of Canada Ltd., Chalk River, Canada

Schneider, H. R.

William M. Brobeck and Associates

Eukel, W.

Brookhaven National Laboratory

Blewett, J. P.
Keane, J. T.
Larson, R.
Oleksiuk, L.
Parzen, G.
Polk, I. J.
Shaylor, H. R.
Spiro, J.
Van Steenbergen, A.

Centre D'Etudes Nucleaires de Saclay

Parain, J.
Prome, M.

CERN

Lapostolle, P.
Sluyters, Th.
Taylor, C. S.

Compagnie Generale de Telegraphie Sans Fil, France

Guilbaud, G.
Jean, R.

Ecole Normale Superieure Orsay

Burnod, L.

Edgerton, Germeshausen and Grier, Inc.

Norris, N. J.

Eitel-McCullough, Inc.

Priest, D. H.

Institut de Recherches Nucleaires
Strasbourg, France

Armbruster, R.
Frick, G.
Gorodetzky, S.

Der Technischen Hochschule Karlsruhe

Schopper, H.

Lawrence Radiation Laboratory

Hubbard, E. L.
Lamb, W. A. S.
Smith, L.
Voelker, F.

Los Alamos Scientific Laboratory

Butler, H.
Hagerman, D. C.
Hart, V.
Hoyt, H. C.
Jameson, R. A.
Knapp, B.
Knapp, E.
Mueller, D. W.
Nagle, D.
Parker, J.
Potter, J.
Putnam, T. M.
Stokes, R. H.
Turner, T. F.
Visscher, W.
Worstell, H. G.

Midwestern Universities Research Association

Curtis, C. D.
Edwards, T.
Kriegler, F. J.
Meads, P. F.
Mills, F. E.
O'Meara, J. E.
Otte, R. A.
Owen, C. W.
Palmer, M.
Pruett, C. H.
Radmer, C. A.
Rowe, E. M.
Shea, M. F.
Snowdon, S. C.
Swenson, D. A.
Symon, K. R.
Young, D. E.

University of Minnesota

Featherstone, R. P.
Hendricks, R. H.

National Bureau of Standards

Leiss, J. E.

Oak Ridge National Laboratory

Kelley, G. G.
Martin, J. A.
Morgan, O. B.
Worsham, R. E.

Rutherford High Energy Laboratory

Carne, A.
Dickson, J. M.
Walkinshaw, W.
Wroe, H.

University of Southern California

Waddell, C. N.
White, E. I.

Stanford Linear Accelerator Center

Johnston, L. H.
Loew, G. A.

University of Tokyo

Nishikawa, T.

U. S. Atomic Energy Commission

McGee, R. P.
Reardon, P.
Wallenmeyer, W. A.

Yale University

Giordano, S.
Gluckstern, R. L.
Grand, P.
Ohnuma, S.
Wheeler, G. W.

R. F. ACCELERATING STRUCTURES: THE CROSS-BAR STRUCTURE

A. Carne
Rutherford High Energy Laboratory, Chilton, England

1. Introduction

Interest in the Cross-Bar Structure is now centred on the energy range 100-200 MeV. Here it is being considered as an alternative to the Alvarez structure for the 200 MeV, 200 Mc/s, Pre-Injector Linac for the CERN 300 GeV A. G. S. project (1). The Cross Bar structure offers several advantages over the Alvarez Guide: Comparable shunt impedance, wide bandwidth and high group velocity in π-mode operation, physical compactness and good mechanical tolerances. In this energy range, focusing is a structure design requirement (though no specific calculations have been done so far), so that drift tube diameter must be chosen on the familiar basis of focusing, and r.f. breakdown capability in conflict with shunt impedance.

It is the purpose of this paper to report on the theoretical work, practical measurements on $\beta = .4$, $\beta = .56$ models, corresponding to 85 and 200 MeV, and further work on the early 400 Mc/s Cross-Bar Structure described elsewhere (2).

2. Theoretical

The major theoretical work is being carried out by Georges Dôme at CERN, and some of the conclusions are presented here.

The formation of field patterns has been derived on a basis of rectangular or square guide (where the side of the square equals the liner diameter), and the fields computed as if the currents were carried on the centres of the bars. Shunt impedance and Q at π-mode have been found as functions of bar diameter d_s and β, by assuming losses in the current carrying bars and side walls only. Losses in drift tubes and the non (total) current carrying bars are not included. If L, D, d, have meanings given in figure 8, and if $k = \omega/c$, $\ell = (D-d)/2$, we have

$$Q = Q_o \left\{ 1 + \frac{8}{\pi} \log\left(\frac{2L}{Kd_s}\right) \beta \left(\frac{\pi d_s}{4L}\right) F + \left(\frac{\pi d_s}{4L}\right) \frac{16 e^{-\pi D/L}}{1+2e^{-\pi D/L}} \right\}^{-1} \quad \ldots \text{ i)}$$

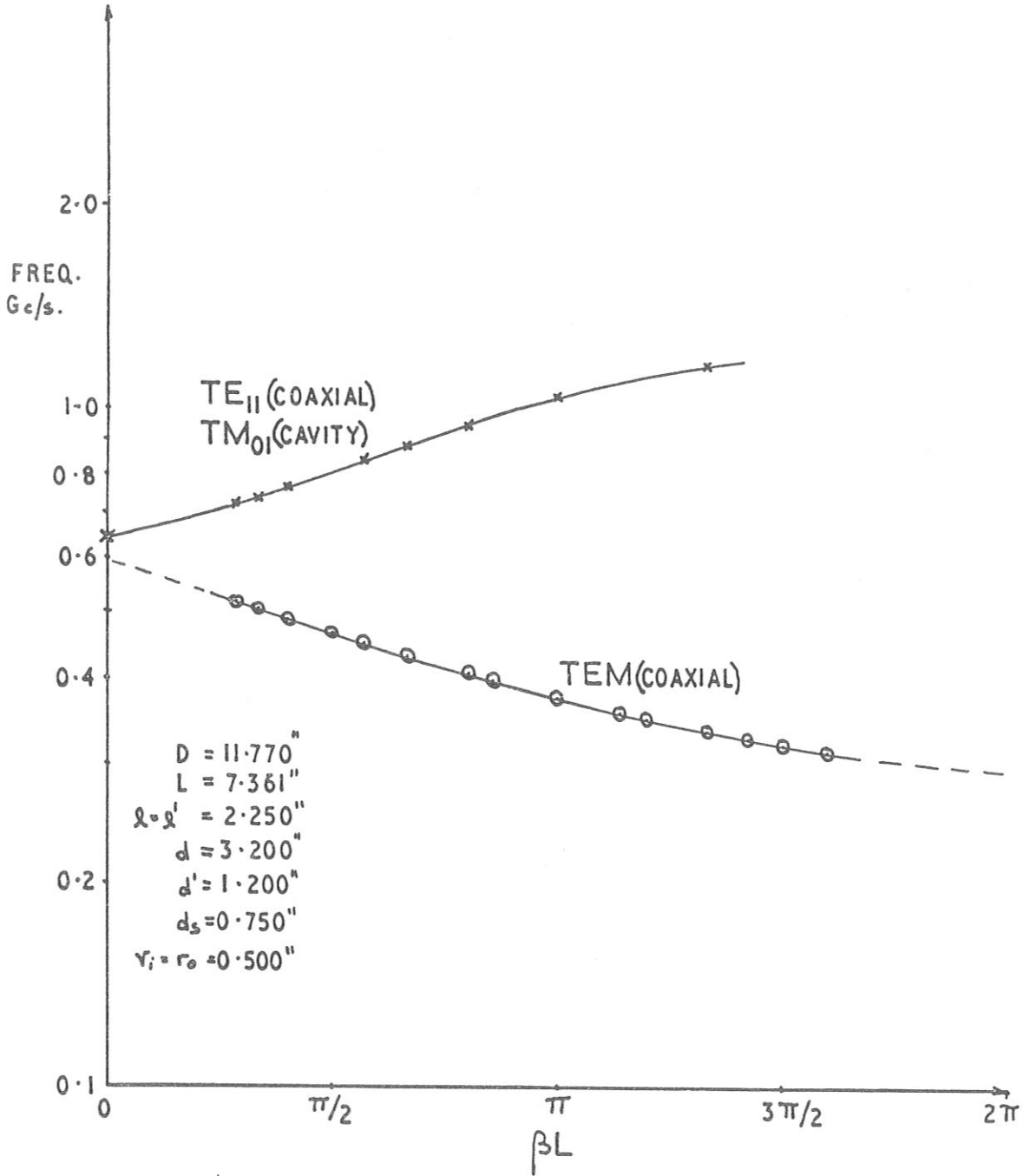

ω/β DIAGRAM FOR SYMMETRICAL CROSS-BAR

FIG. 1

where K is the complete elliptic integral: $K = \pi/2 \left(1 + 2e^{-\pi D/L} + \ldots\right)^2$;

$Q_o = \mathrm{Log}\left(\frac{2L}{Kd_s}\right) \frac{\pi d_s}{\lambda} \sqrt{\frac{\sigma}{\pi \epsilon f}}$ is the Q-value for losses on bars only ...

and $F = \pi/2 \left(k\ell + \sin k\ell \cos k\ell\right)^{-1} \geq 1$. Since D/L is usually >> 1,

$K \sim \pi/2$, and equation i) reduces to

$$Q \sim Q_o \left\{1 + \frac{8\beta}{\pi} \left(\frac{\pi d_s}{4L}\right) F \,\mathrm{Log}\left(\frac{4L}{\pi d_s}\right)\right\}^{-1} \quad \ldots \text{ iii)}$$

Equation iii) has been checked against the early 400 Mc/s model to give Q = 11, 200 against a measured 11, 900 (scaled from brass). This is very good agreement. Shunt impedance is given by:

$$\eta = \frac{QZ_o}{L} \frac{8M^2}{k\ell\,(1+\cot^2 k\ell) + \cot k\ell} = \frac{16}{\pi}\left(\frac{QZ_o}{L}\right)\left[M^2 F \sin^2 k\ell\right] \quad \ldots \text{ iv)}$$

where $Z_o = 60 \log\left(\frac{2L}{Kd_s}\right)$ is the characteristic impedance of a coaxial line, centre conductor d_s, (square) side L; and M is the transit time factor (the experimental approach to T. T. F. is given in section 4b). The variation of maximum shunt impedance with bar diameter and velocity is found by considering the maximum value of $(Q\,Z_o/L)$ with d_s and β. (The term inside the square bracket of eqn. iv) is proportional to (particle energy gain)^2/(stored energy), again discussed in section 4b). Considering only the second terms inside the bracket of eqn. i), we must maximise the function

$$\left(\frac{QZ_o}{L}\right) = \left(\frac{Q}{Q_o}\right)\frac{Q_o Z_o}{L} \propto \frac{\pi d_s}{4L} \frac{\left[\mathrm{Log}\left(\frac{\pi d_s}{4L}\right) - 2\,\mathrm{Log}\left(1+2e^{-\pi D/L}+\ldots\right)\right]^2}{1 + \frac{8}{\pi} F\beta\left(\frac{\pi d_s}{4L}\right)\mathrm{Log}\left(\frac{4L}{\pi d_s}\right)}$$

A good approximation to the maximum is given when

$$\mathrm{Log}\left(\frac{4L}{\pi d_s}\right) = 1 + \xi + \sqrt{1 + 0.541\gamma}$$

where $\xi = 2 \log (1 + 2e^{-\pi D/L} + \ldots) = 2 \log \left[1 + 2e^{-\frac{\pi D}{D-d}\left(\frac{2k\ell}{\pi}\right)\frac{1}{\beta}}\right]$, and

$\gamma = \frac{8}{\pi} F\beta$. Since ξ and γ increase with β, η decreases (slowly)

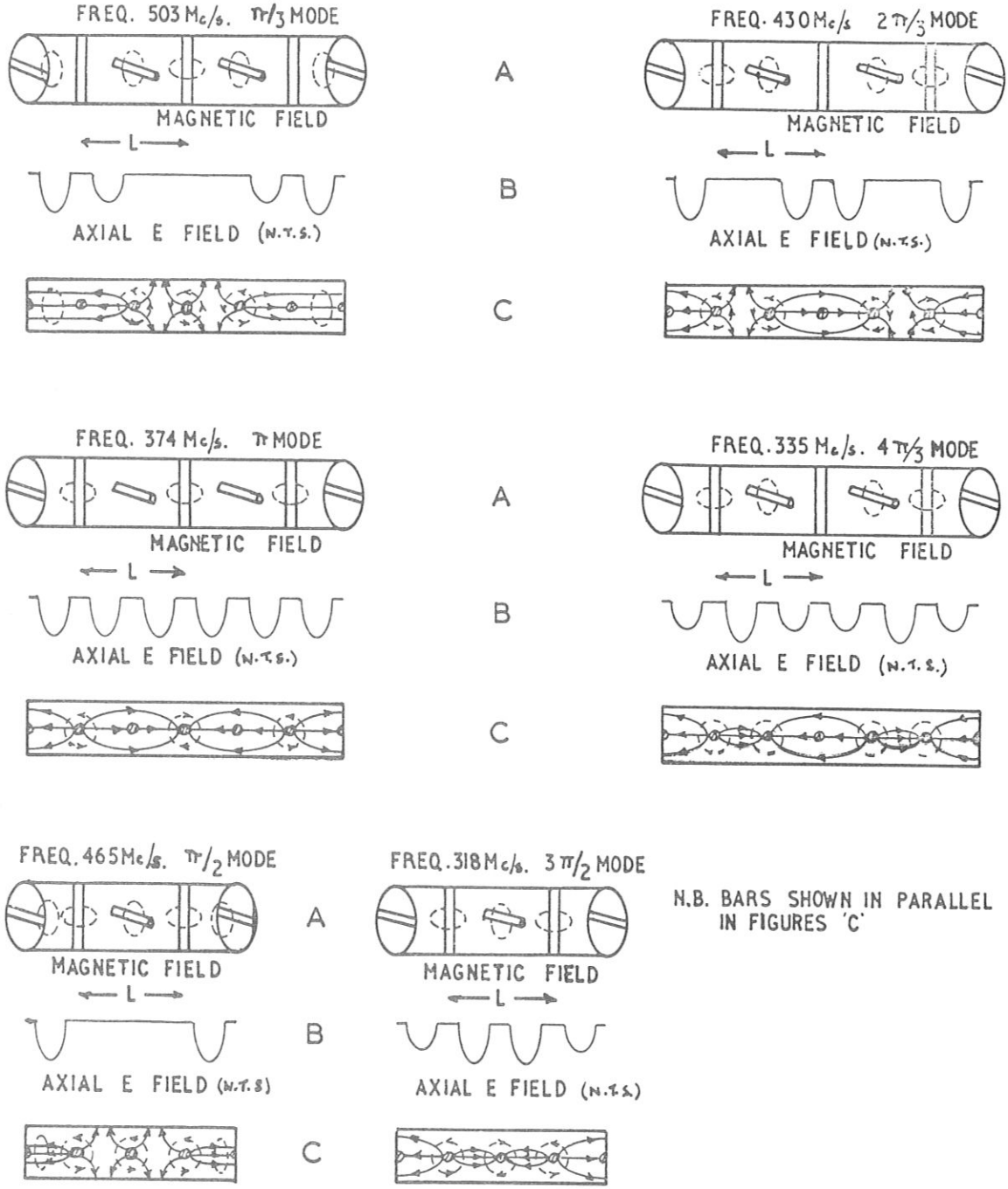

FIELD PATTERNS INSIDE CROSS-BAR STRUCTURE

FIG. 2

with β. If the optimum shunt impedance at $\beta = 0$ is given by unity, then we have for η and (L/d_s) opt:

β	(L/d_s) opt.	$\eta_{max.}$
0	5.8	1
.5	8.7	0.69
1	16.6	0.42

It is of interest to note that the bar need not be changed for $\beta = 0.5$ to 1.0. Over the energy range of interest (100-200 MeV), the fall of η max is 12%.

3. Field Patterns in the Cross-Bar Structure

Further measurements have been carried out on the early, symmetrical, 400 Mc/s model to determine field patterns in the various modes. This was done by axial field perturbation, and by magnetic loops through holes in the liner. The results are summarized in figures 1 and 2. In addition to the two $\omega - \beta$ branches shown in figure 1, there were many other resonances, all of them very much smaller than those plotted (of the order 30 db down) and may be H-modes, cable resonances, or harmonic resonances from the signal generator used.

The upper branch of the $\omega - \beta$ curve is obtained when the guide behaves as coupled coaxial resonators in the TE_{11} mode, giving rise to the TM_{01} mode along the guide. In this mode the magnetic field lines are purely circumferential, but distorted into oval, rather than circular, loops. Note also that for the TE_{11} mode (coax.) or TM_{01} guide, the zero mode can exist as the boundary conditions at the end plates can be satisfied. (The zero mode point in Figure 9, reference 2, is in fact the zero mode point for the upper branch). This mode has a forward fundamental, and is similar to the fundamental mode for the Alvarez structure. That this is so can be seen by linking together a series of coaxial resonators in the TE_{11} mode. Distorting the outside diameters to give a cylindrical waveguide with partitions reduces both 0 and π mode frequencies. Note the current flow is in opposite directions, 0-mode, and in the same direction in π-mode on either side of a partition. Cutting slots in the outside edges of the partitions in the direction perpendicular to the plane of the bars, does not affect the current lines in 0-mode, but shortens them in π-mode, i.e. causes the π-mode frequency to increase. The same effect can be seen by considering the capacitive effect of the slots. Putting in drift tubes loads down the two frequencies by roughly the same amount.

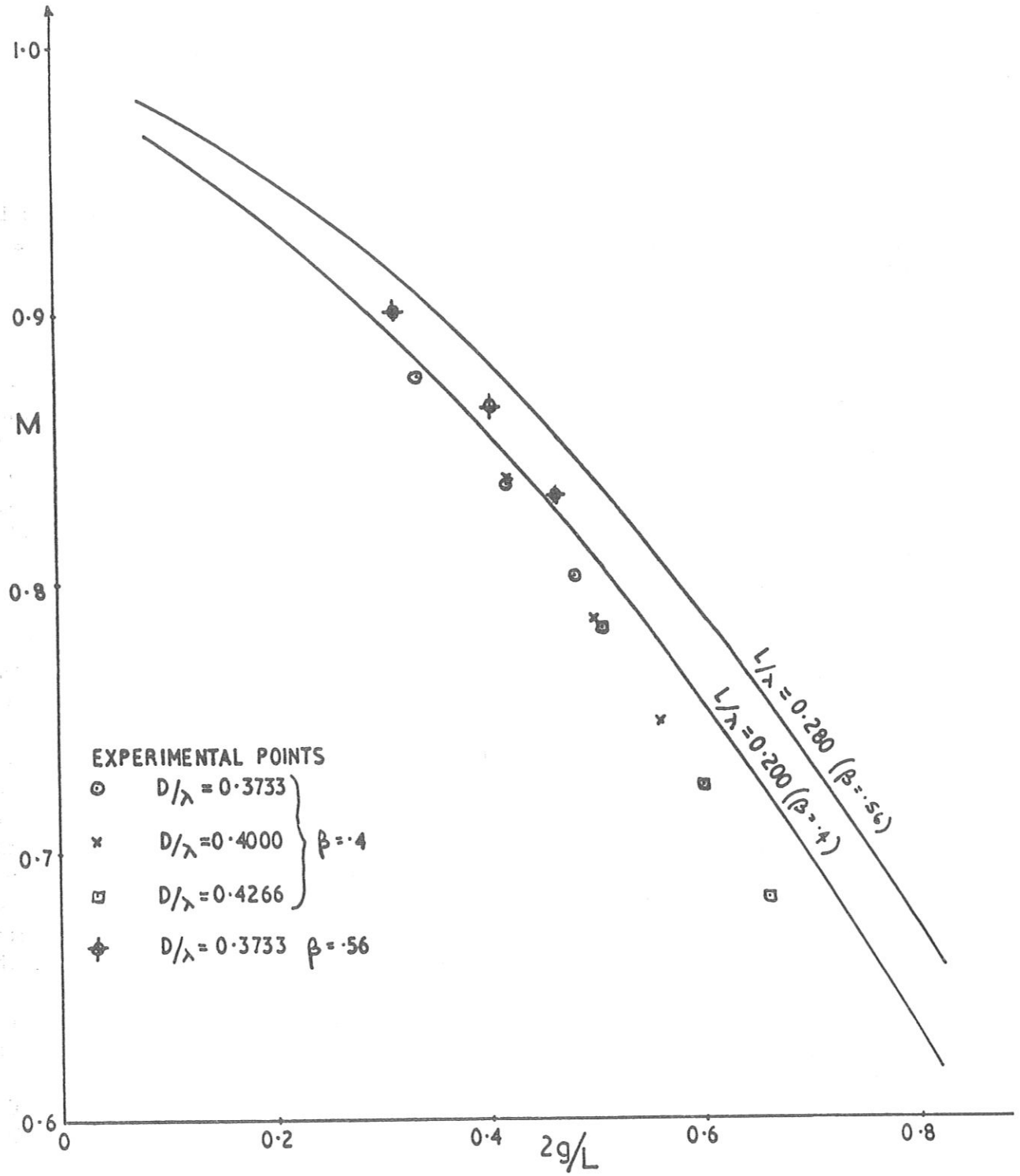

TRANSIT TIME vs., 2g/L IN CROSS BAR MODELS

FIG. 3

The "Cross-Bar Mode" is the lower branch in the $\omega - \beta$ diagram, and has been previously (2) described in terms of coupled coaxial resonators in the TEM (fundamental) mode*. (It should be remarked that this synthesis of modes in terms of partitioned coaxial resonators, rather than by starting with cylindrical guide with thin partitions, is preferable since it does allow for the effect of the finite thickness of the structure components). As such it is not possible to terminate the structure in 0 or 2π (i.e. when all the bars act as coaxial resonators) modes. On the 4 whole section model used with terminations in half bars, in π-mode the magnetic field was seen to exist in loops round one set of bars, and none at all in the second set containing the terminations. Figure 2 shows the magnetic field patterns, and the axial field plots (N.T.S.) in some of the modes measured in the model. It can be seen that for modes $\theta < \pi$, circumferential as well as coaxial H fields can exist. How much the circumferential components of H fields depend on the terminations than perhaps on some hybrid coaxial mode is not clear at present. Further measurements on the model with flat-plate terminations are to be done to clarify this (and, more important, to enable us to find the characteristics of the structure with one set of bars removed). For modes $2\pi > \theta \geq \pi$ H-lines coaxial with the bars only were found. In this short symmetrical model no degeneracy was seen (but not surprisingly). A long 30-cell model, without drift tubes, with bars whose diameters are in the ratio 2:1, has been made to study the π-mode region, but there are no results to report as yet. Although there is a physical asymmetry in a long structure, it should be possible to have a continuous $\omega - \beta$ curve at π mode and hence a high group velocity. For small gaps with resulting uniform E fields, asymmetries in the drift tube lengths will have only a second order effect on capacitance, referred to one set of drift tubes or the other. Equalizing the bar diameters (or nearly so) to give the same π-mode resonant frequencies has only a small effect on the shunt impedance. Fine tuning can be obtained by use of tuners in the neighbourhood of one set of bars.

---

*NB. In Yale Conference Report P121, figure 9A '0'-mode, ALL E-lines should go from bars to liner, and not only alternate bars as drawn.

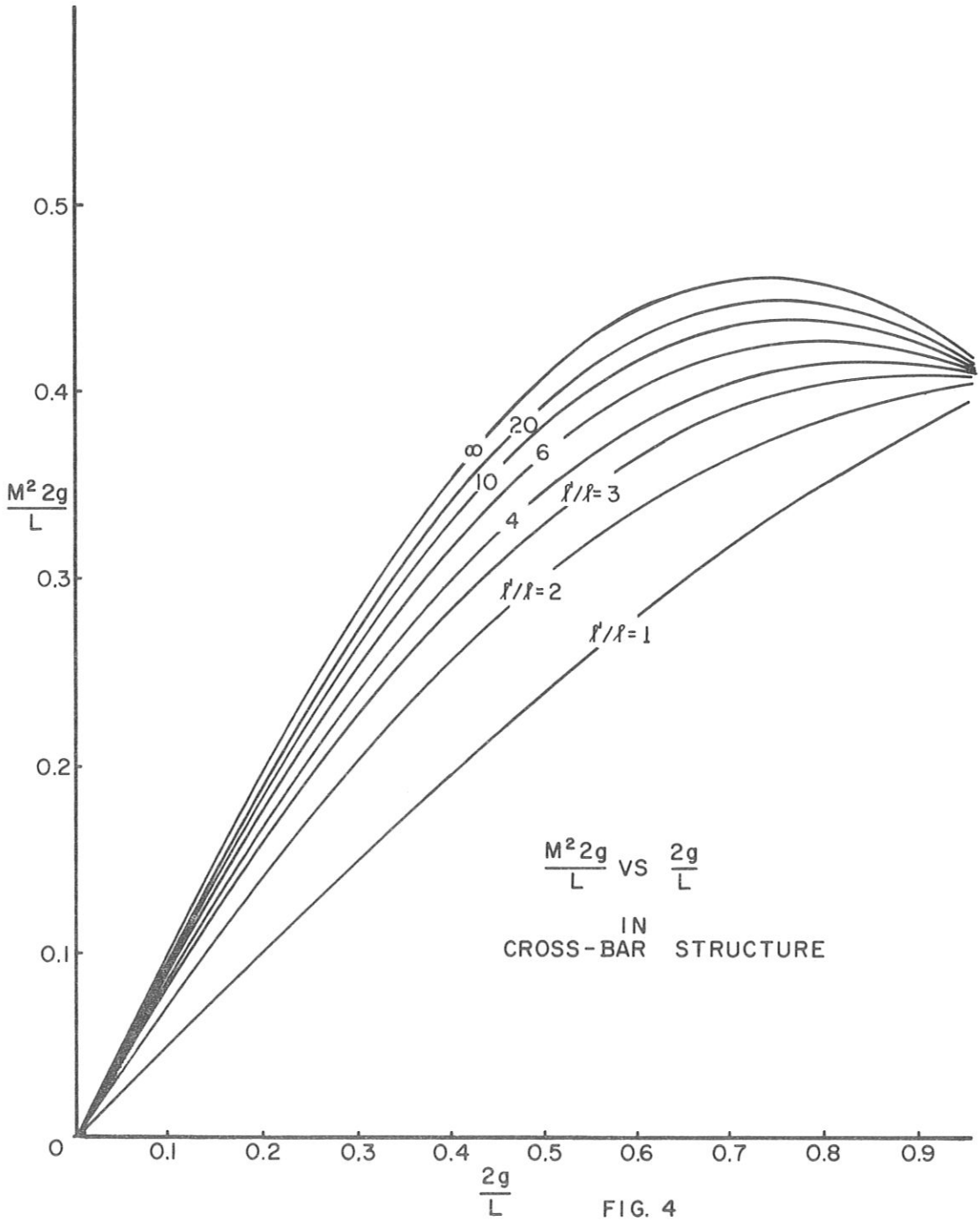
0.5
0.4
0.3
0.2
0.1
0
M²2g/L
∞
20
10
6
4
ℓ'/ℓ=3
ℓ'/ℓ=2
ℓ'/ℓ=1
M²2g/L VS 2g/L
IN
CROSS-BAR STRUCTURE
0.1
0.2
0.3
0.4
0.5
0.6
0.7
0.8
0.9
2g/L

FIG. 4

4. Quarter-Scale Models for CERN 200 MeV Linac

Two 800 Mc/s (1+2 (1/2)) cell models have been made, for velocities $\beta = .4$ ($\sim$ 85 MeV) and $\beta = .56$ ($\sim$ 200 MeV). The two sets of drift tubes are of different lengths but constant diameters $d/\lambda = 0.0868$, corresponding to d = 5.125 inches, full scale, to enable them to house quadrupoles; drift tube bores $d'/\lambda = 0.0233$, as the value taken for the stage 1 design for the Alvarez structure. In each model, 3 different diameters for the current carrying bars (corresponding to $L/d_s = 6, 8, 10$) and 3 values of liner diameter ($D/\lambda = 0.373, 0.4, 0.427$, i.e. 14, 15, 16 cm at 800 Mc/s) were used. For a given liner diameter, for each diameter bar, the length of the 'large' drift tubes was adjusted to give a π-mode resonant frequency within 2 Mc/s of 800 Mc/s, and the η/Q measured. The liner was then bored out and the measurements repeated. The same sets of drift tubes and bars could be used, since boring out the liner increases the cavity inductance, and reducing the lengths of drift tubes (i.e. increasing gap lengths) reduces the capacitance and restores the resonant frequency. Bandwidths, defined here by $(f_{2\pi} - f_o)/f_\pi$ cannot be measured directly for the reasons given previously, but extrapolation from the modes measured give values of the order of 100%.

Further aspects of these models are discussed under separate headings..

(a) R.F. Breakdown

As yet there is no detailed information on the field distribution across the drift tubes, so that r.f. breakdown capabilities are not known. To this end, high power measurements are to be carried out in the near future. However, rough estimates on performance can be obtained from data given by Wilkins (3) for re-entrant cavities. Treating each half-cell as a separate cavity, for which T.T.F. (measured) and E_o (the mean gap field, assumed uniform) are known, then for the drift tubes for the given diameter and profiles given by $r_o/\lambda = 0.0127$, $r_1/\lambda = 0.0062$, (i.e. the same as the Rutherford Lab. or CERN 50 MeV Linacs), values of E_s/E_o in the range 1.2 - 1.5 for $\beta = .4$ - .56 can be expected, and for $E_s \geq 14.7$ Mv/m (Kilpatrick's Criterion at 200 Mc/s) acceleration rates of the order 4 MeV/m could be achieved. Alternatively, and subject to the practical requirements of quadrupole focusing, smaller drift tube diameters could be used with a lower acceleration rate, with an improvement in shunt impedance. (Maximum shunt impedance requires that d/L and ℓ/d be as small as possible for a given (g/d), where the terms have the meanings given in figure 8).

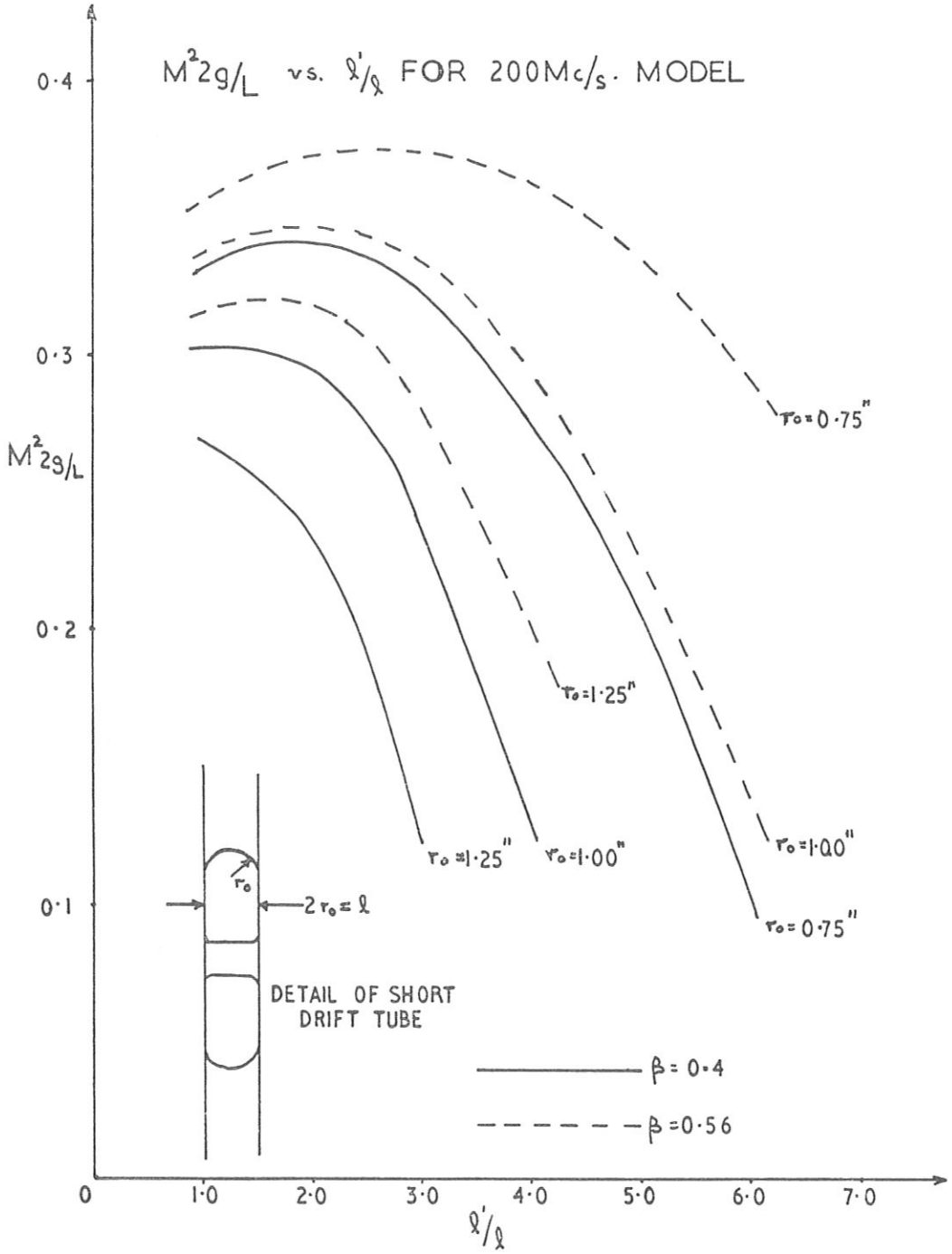
$M^2 2g/L$ vs. ℓ'/ℓ FOR 200Mc/s. MODEL
0·4
0·3
0·2
0·1
$M^2 2g/L$
$r_o = 0.75''$
$r_o = 1.25''$
$r_o = 1.00''$
$r_o = 1.25''$
$r_o = 1.00''$
$r_o = 0.75''$
r_o
$2r_o = \ell$
DETAIL OF SHORT DRIFT TUBE
$\beta = 0.4$
$\beta = 0.56$
0
1·0
2·0
3·0
4·0
5·0
6·0
7·0
ℓ'/ℓ

FIG. 5

(b) Transit Time Factor, and η/Q

It was clear from the measurements on the early 400 Mc/s model that although the shunt impedance was high, so too was the content of higher order space harmonics. Since these contribute only to the losses, and not to acceleration, the Cross-Bar Structure is from this point of view still somewhat inefficient. By changing the lengths of drift tubes, but keeping the gap lengths constant so that the effect on resonant frequency is only second order, a change in harmonic content can be obtained. The π -mode wave form is given in the sketch, where

ℓ is the length of the small drift tube
ℓ' is the length of the large drift tube
L, periodic length, $= \ell+\ell'+2g$;
$\beta_o L = \pi$ for π -mode

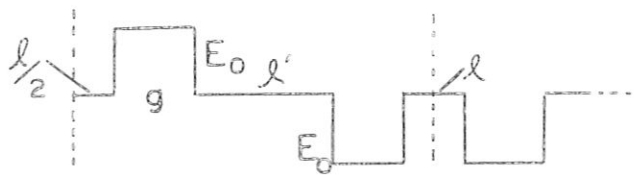

The field is assumed uniform in the region of the gaps (a fair assumption providing the gaps are small), and zero inside the drift tubes ℓ, ℓ'. The amplitude of the n^{th} harmonic is given by

$$(T.T.F.)_n = \int_0^L E(z)\cos\beta_n z\, dz \Big/ \int_0^L E(z)\, dz$$

$$= \frac{\sin\left(\frac{\beta_n g}{2}\right)}{\frac{\beta_n g}{2}} \sin\left(\frac{\beta_n L}{2}\right) \sin\frac{\beta_n}{2}\left(g+\ell'\right),$$

and for the fundamental, the T. T. F. is

$$M = \sin\frac{\pi g}{2L} \sin\frac{\pi}{2L}(g+\ell') \Big/ \pi g/2L .$$

Clearly the smaller the gap, the larger the T. T. F. (practically obtainable by use of small diameter drift tubes), and the smaller the drift tube ℓ,

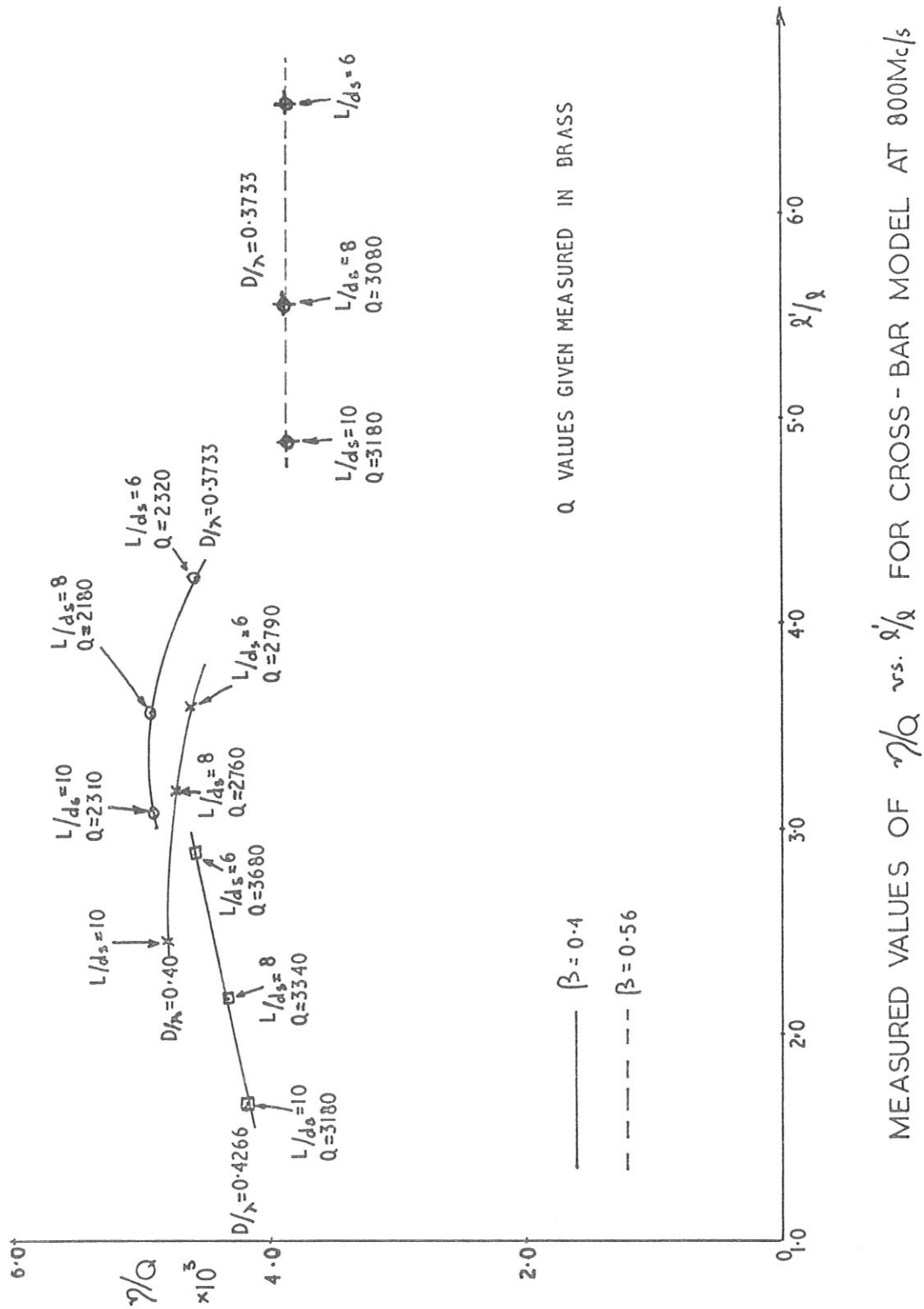

MEASURED VALUES OF η/Q vs. λ'/λ FOR CROSS-BAR MODEL AT 800Mc/s

FIG. 6

the greater the T. T. F.. Curves of T. T. F. to include the drift tubes geometries of the two models are given in figure 3, and compared with measured values: agreement is good for small gaps, $\sim 3/4\%$, but for larger gaps the error is larger, $\sim 5\text{-}1/2\%$, as to be expected since the gap field becomes non-uniform (but more like $1/r$ variation from the large drift tubes, as for a coaxial field).

The optimum efficiency for the structure is when the ratio (Energy gain per unit length)^2/(Stored energy per unit length) is a maximum, i.e. the stored energy needed to produce a required accelerating field in a minimum. This ratio is proportional to η/Q, and for small gaps, proportional to $M^2(2g/L)$. Curves of $M^2(2g/L)$ against $(2g/L)$ for values of ℓ'/ℓ are plotted in figure 4. For most values of ℓ'/ℓ the optimum ratios are for $(2g/L) \sim 0.7\text{-}0.8$. Note that the maximum value is for $\ell'/\ell = \infty$, i.e. when there are no small drift tubes, and $(2g/L) = 0.74$, but since field lines exist round these bars and drift tubes in the $(\pi, 2\pi)$ region, doing this removes some capacitive loading, with a consequent reduction in bandwidth. For ℓ'/ℓ 3-4 there is little variation in $M^2(2g/L)$ with $(2g/L)$ in the range 0.6-0.8. For a given small drift tube length ℓ (as used in both models where ℓ = stem diam. = 2 x outer profile radius, equal to 1-1/2 inches at 200 Mc/s) $M^2(2g/L)$ is given in figure 5, where the optimum values are for $\ell'/\ell \sim 2$, $\beta = .4$; $\ell'/\ell \sim 3$, $\beta = .56$.

For a given liner diameter, for each value of bar diameter, the large drift tubes were machined to give the correct frequency, and the (η/Q) value was measured, according to the formula

$$\eta/Q = A \left(\int_0^L E(z) \cos \beta_n z \, dz \right)^2 / \omega \epsilon L, \quad \beta_n = \beta_0 = \pi/L$$

where ϵ is the stored energy, and A = 2 for T. W. operation, = 1 for S. W. (e.g. π). (Results given previously (2) were in fact for T. W. operation, so that π-mode values should be reduced by a factor 2). Results obtained so far are given in figure 6, and scaled to 200 Mc/s ($\eta/Q \propto 1/\lambda$), in table 1 below. Values of η/Q are between 2 (at $\beta = .4$) and 3 ($\beta = .56$) times greater than corresponding values for the Alvarez structure (1). That there is a change of shape in the sets of points ($\beta = .4$) is in agreement with figure 5, where for D = 14, 15 cm (model) all points are to one side of the peak, but for D = 16 cm. includes the peak.

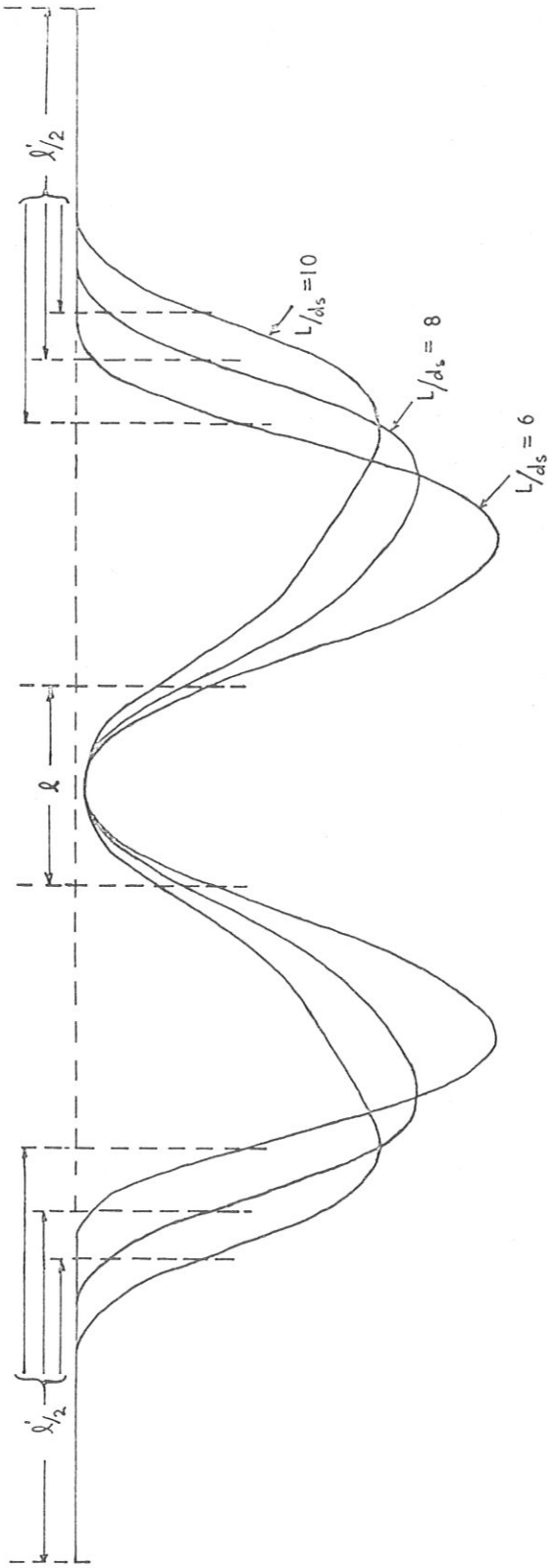

FIG. 7 PLOT OF $\Delta f \propto |E|^2$ AT $\beta = 0.4$ (D=14cm)

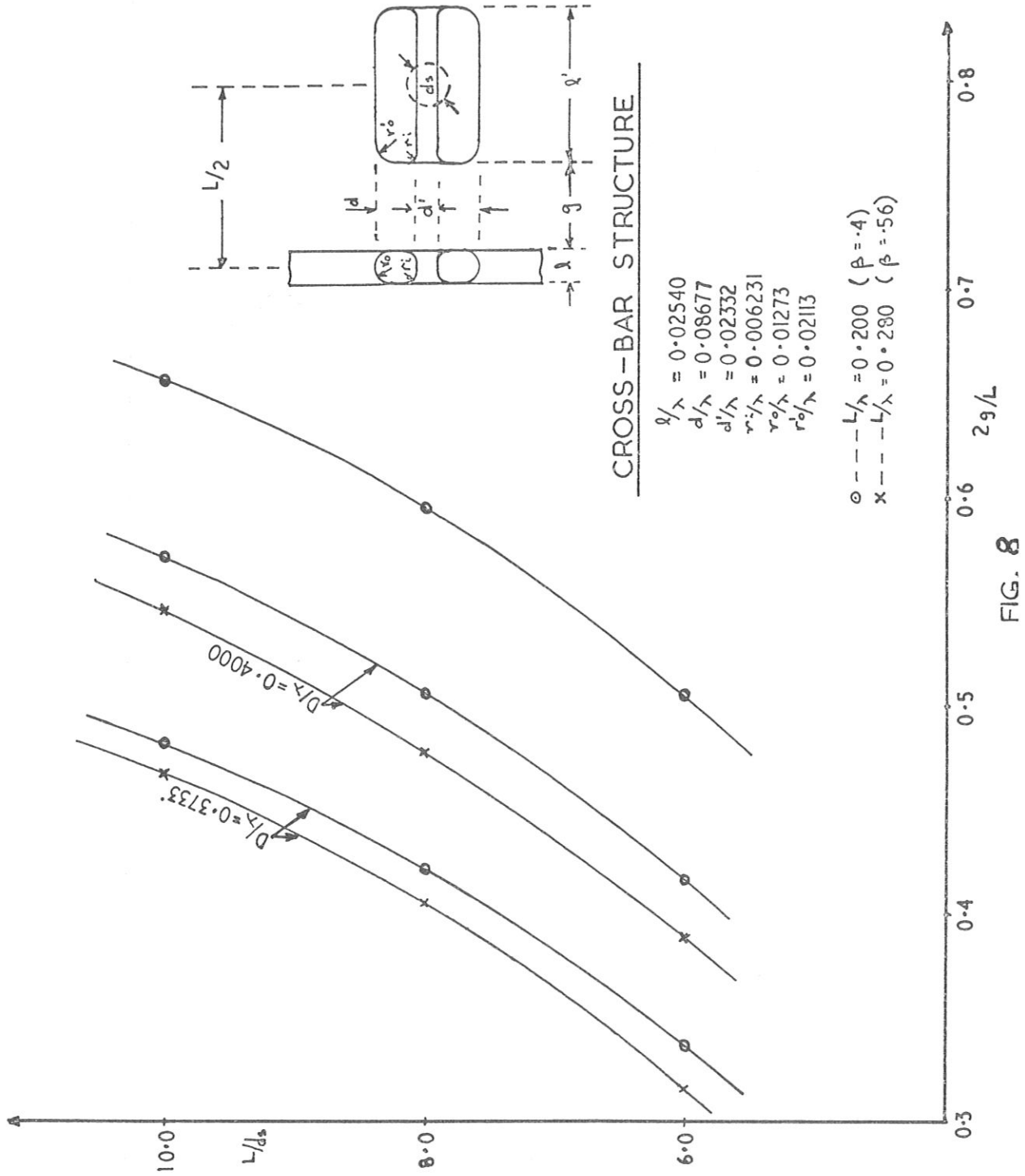
L/d*
10·0
8·0
6·0
0·3
0·4
0·5
0·6
0·7
0·8
2g/L
D/λ=0·4000
D/λ=0·3733
L/2
d
d'
g
l'
l
CROSS-BAR STRUCTURE
ℓ/λ = 0·02540
d/λ = 0·08677
d'/λ = 0·02332
r'i/λ = 0·006231
r'o/λ = 0·01273
r''o/λ = 0·02113
○ - - - L/λ = 0·200 (β=·4)
× - - - L/λ = 0·280 (β=·56)

FIG. 8

TABLE 1

800 Mc/s CROSS BAR MODEL MEASUREMENTS

$\beta = 0.4$ $\quad \ell = 0.375''$

D (cm)	L/d_s	2g/L	ℓ'/ℓ	M	M(cal)	η/Q	Q (Brass)	η/Q (Scaled to 200 Mc/s)	η/Q th. 800 Mc/s
14	6	0.337	4.219	0.8757	0.8845	4.55×10^3	2,320	1.14×10^3	4.50×10^3
14	8	0.421	3.560	0.8371	0.8472	4.91×10^3	2,180	1.23×10^3	4.72×10^3
14	10	0.482	3.080	0.8026	0.8178	4.87×10^3	2,130	1.22×10^3	4.83×10^3
15	6	0.417	3.592	0.8390	0.8486	4.58×10^3	2,790	1.15×10^3	
15	8	0.501	2.931	0.7866	0.8080	4.68×10^3	2,760	1.18×10^3	
15	10	0.561	2.453	0.7481	0.7764	4.78×10^3	-	1.20×10^3	
16	6	0.507	2.880	0.7821	0.8050	4.55×10^3	3,680	1.14×10^3	
16	8	0.597	2.176	0.7246	0.7565	4.30×10^3	3,340	1.07×10^3	
16	10	0.661	1.666	0.6816	0.7195	4.16×10^3	3,180	1.04×10^3	
$\beta = 0.56$		$\ell = 0.375$							
14	6	0.317	6.533	0.9008	0.9155	3.83×10^3	-	0.96×10^3	
14	8	0.405	5.560	0.8652	0.8808	3.86×10^3	3,080	0.97×10^3	
14	10	0.466	4.885	0.8315	0.8537	3.82×10^3	3,180	0.96×10^3	
15	6	0.388	5.747				3,610		
15	8	0.479	4.739				3,630		
15	10	0.543	4.035				3,290		

Of particular interest is the set of perturbation curves shown in figure 7, for the $\beta = .4$, D = 14 cm model. The distorting effect on gap field of increasing gap length can be seen. Comparison of the $L/d_s = 6$ and 10 curves shows that for $L/d_s = 6$, η/Q is 7% greater and the peak total E-field 18% LESS than for $L/d_s = 10$. Generally as the gap increases (i.e. ℓ' gets smaller), the peak total E-field decreases, but not necessarily (η/Q).

Q values on the models are also included in figure 6 and the table, showing generally that as the volume of the cavity is increased (increasing D for a given L, or vice versa) Q increases, and for a given model, Q increases more rapidly than (η/Q) decreases with D. For a given D and L, Q decreases slowly with increasing L/d_s. The actual Q values are low due to the multiplicity of dry (demountable) joints: in particular the joints of the current carrying bars with liner used indium rings in grooves in the liner. (Since these joints will carry a heavy current in high power conditions, their quality becomes a major problem). The final 800 Mc/s model will have soldered joints to give a more representative Q-value. Scaled to 200 Mc/s and copper, the model values become of the order 12-14000. At least a doubling of this value is hoped for in the high power structure with good joints.

(c) Dimensional Tolerances

As already stated, for given D, d_s the large drift tubes ℓ' were machined to give the correct frequency. A summary of dimensions for constant frequency in the models is given in figure 8. From the data obtained we deduce the following tolerances per thousandth inch

	$\beta = .4$	200 Mc/s	$\beta = .56$
D	7 kc/s		7.3 kc/s
bar d_s	25 kc/s		21 kc/s
ℓ' (or total gap)	11 kc/s		8.75 kc/s

These tolerances are generally very similar to the Alvarez structure at 200 Mc/s and can be seen to get easier with increasing energy.

5. Conclusions

Model measurements show the Cross-Bar Structure to have (η/Q) values between 2 and 3 times greater than the Alvarez Structure in the range 100-200 MeV. Providing the theoretical Q-values can be achieved - and this requires attention to r.f. joints, particularly between the current carrying bars and line - then the Cross-Bar Structure should have shunt impedances

(200 Mc/s, $\phi_s = 0$) of the order 25-20 M Ω/m between 80-100 and 200 MeV. These values are comparable with the Alvarez structure at 80-100 MeV, and certainly better at 200 MeV. (At much higher energies ($\beta \sim 1$), the shunt impedance would be of the order 30%-50% less than the values quoted (i.e. $\sim$ 25 M Ω/m at v = 0, 800 Mc/s).) Further enhancement of these figures can be achieved by increasing D and reducing d, ℓ to obtain ratios nearer (2 g/L) $\sim$. 7, (ℓ'/ℓ) $\sim$ 3 - 4, giving optimum values for M^2 (2 g/L). Reduction of ℓ, d now depends on requirements for focusing, and r.f. breakdown capabilities. Future work will include high power model measurements to assess the r.f. voltage breakdown performance, and to check the design of r.f. joints.

Further advantages of the Cross-Bar Structure are its physical size (where the liner diameter is now of the order 60 cm, compared with the $\sim$80 cm Alvarez guide at β = .4), its mechanical tolerances (certainly no worse than the Alvarez guide), and its high group velocity v_g. If the structure is symmetrical, then at π-mode $v_g \neq 0$ (and on the early 400 Mc/s model v_g = 0.193 c); if the structure is asymmetric (as is required by transit time considerations above), a continuous $\omega - \beta$ curve at π-mode is still possible by selective tuning. Again, future work will include a study of the region around π-mode to determine the magnitude of mode splitting in an asymmetric structure and the effects of correction.

6. Acknowledgments

The author would like to express his thanks to Dr. George Dôme of CERN for making freely available his theory of the Cross-Bar Structure, and for much stimulating discussion, and Mr. Normal Fewell who carried out the experimental measurements.

NAGLE: Did you say your practical value for shunt impedance was 20 megohms per meter?

CARNE: Yes, 20 megohms per meter at 200 MeV and 200 Mc is a value that we expect to achieve. This includes all losses.

KNAPP: How did you scale that result?

CARNE: Taking the Q values that we have in the 800 Mc model, Q's of around 3000 to 3500, and scale from brass to copper, and from 800 to 200 Mc, we get Q's of about 14,000. Experience suggests that we can increase this value by a factor 1-1/2, by making the models with better joints. An important point about these model measurements is that the cavities were demountable in many ways in order to change the outside

diameter, stem diameter and drift tube length. In particular, the cross section of the joint of a current-carrying bar with the liner is shown in the sketch. Contact was made by compressing indium rings in grooves in the body of the liner. (Three grooves were cut: one for each of the three liner diameters, D, used). It was hoped that this system would give good rf contact, but, in fact, it turned out to be rather poor. This is similar to the experience that we also had on the original 400 Mc/s model (described at the Yale Conference). There we had dry joints, and the Q's were poor. As we increased the number of cells, instead of the Q increasing as expected, we found it actually went down due to the increase in number of joints. We have really to make good soldered rf joints to get good Q values.

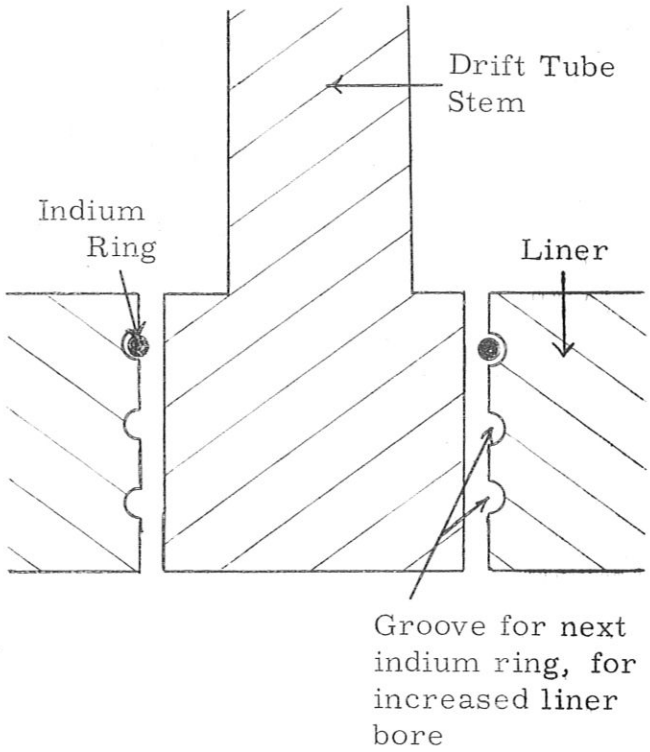

HUBBARD: How many cells are there in your model?

CARNE: On the 800 Mc models we have one full cell and two half cells for doing the R/Q measurements. We are not taking end plate losses into account for the Q values, it not being necessary in the cross-bar structure.

GIORDANO: As you increased the drift tube diameter, you found an increase in shunt impedance and a decrease in field intensity. Was this decrease in field intensity on the axis? And were there any other regions where the field was higher?

CARNE: That I don't know. The actual plot you saw was just that of an axial field perturbation.

References

(1) "Design of a High Current 200 MeV Proton Linear Accelerator".

A Carne, K. Batchelor, NIRL/R/55 March 1964, and Yale Linac Conference Report, p 404, October 1963.

(2) "Structures for High Energy Proton Linear Accelerators". A Carne.

International Conference, Dubna, August 1963; also Yale Conference, October 1963.

(3) "Design Notes on Resonators for P.L.A.'s" J. J. Wilkins. AERE GP/R 1613, 1955.

COUPLED RESONATOR MODEL OF LINEAR ACCELERATOR TANKS*

D. E. Nagle
Los Alamos Scientific Laboratory, University of California
Los Alamos, New Mexico

I. Introduction

This paper will review the coupled resonator model of the linear accelerator resonant tanks, in the form in which we have applied it for understanding our experimental results, both with the computers and with experimental models. The present form of the model has grown out of discussions with Ed Knapp, Bruce Knapp, and others. The steady state results will be discussed by E. Knapp in the following paper. R. Jameson in a talk to be given later in the week will discuss his theory and measurements of the transient behavior of the tanks and the design of a servo control system for rf amplitude and phase. In his talk you will see that many purely algebraic properties connected with the symmetry of the system are common to the transient and to the steady state theory.

The dispersion relations for the simple and for the doubly periodic ring or chain of coupled oscillators are familiar results of lattice vibration theory; see, for example, Brillouin's book.[1]

Some results are perhaps novel, particularly those concerned with phase shifts, effects of perturbations, and locking phenomena. Also, the discussion of the relation between ring and chain has been used extensively in our work.

Although pictorially we often refer to the familiar lumped circuits, which suggests a severe limitation on generality, this is only a convenience. The important equations refer to the resonant frequencies, their widths, amplitudes, and phases, and to the strength of coupling, quantities which at these frequencies are directly or indirectly easily measurable. The approach is useful so long as it is possible to describe the behavior using separated modes of a single cavity as they develop into bands of the coupled system. (We always refer to a tank as a chain of coupled cavities.) The agreement with measurement, as you will see in the following paper, is remarkably good.

Figure 1 illustrates the correspondence between coupled cavities, coupled circuits, and a linear lattice. The correspondence between

---

*Work performed under the auspices of the U. S. Atomic Energy Commission.

circuits and cavities is direct as shown if we talk in terms of the amplitude and resonant frequency, a single mode of oscillation of the single cavity, and the coupling strength of this mode to the next cavity. Of course, k can be given in terms of overlap integrals of field quantities. The analogy with the linear lattice with next-nearest-neighbor coupling is familiar. For most of the talk we consider only a single cavity mode at a time; this describes most of the experimental data.

II. Circuit Equations

The circuit equations are $n = 1 \ldots . 2N$

$$\epsilon_n = (2 j \omega L + R + \frac{1}{j \omega C}) i_n + j k \omega L (i_{n-1} + i_{n+1}) \qquad (1)$$

$$\frac{\epsilon_n}{2 j \omega L} \equiv I_n \cong (1 - \frac{\omega_o^2}{\omega^2}) i_n + \frac{k}{2} (i_{n-1} + i_{n+1}) \qquad (2)$$

where $\omega_o^{-2} = 2 L C (1 + \frac{1}{j Q})$; $Q = \frac{2 \omega L}{R}$. (3)

There are $2N$ solutions to homogeneous equations ($I_n = 0$) of the form

$$i_n^{(q)} \cong \text{const.} \times e^{2\pi j \frac{qn}{2N}} \qquad (4)$$

(q is the mode number, n is the circuit number). Provided that

$$0 = (1 - \frac{\omega_o^2}{\omega_q^2}) e^{\frac{2\pi j q n}{2N}} + \frac{k}{2} (e^{\frac{2\pi j q [n-1]}{2N}} + e^{\frac{2\pi j q [n+1]}{2N}})$$

as may be seen by substituting (4) into (2), or

$$\omega_o^{-2} - \omega_q^{-2} + k \omega_o^{-2} \cos \frac{\pi q}{N} = 0 . \qquad (5)$$

This is the dispersion relation for the simple ring of $2N$ circuits, or for the lattice with periodic boundary conditions. It is plotted as Fig. 2.

$\pi q/N = \varphi$ is the mode phase shift per cell; e.g., $q = N$ is called the π-mode.

III. Matrix Form at Circuit Equations

We had

$$(\omega_o^{-2} - \omega^{-2}) i_n + \frac{k}{2} \omega_o^{-2} (i_{n-1} + i_{n+1}) = \omega_o^{-2} I_n .$$

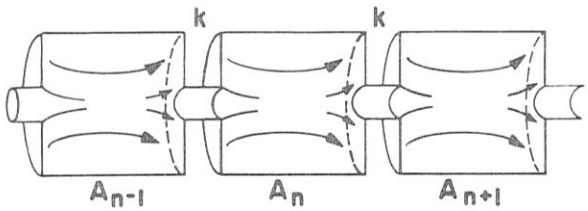

COUPLED CAVITIES

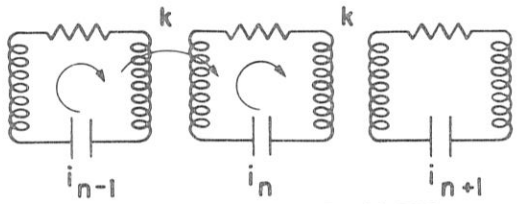

COUPLED CIRCUITS

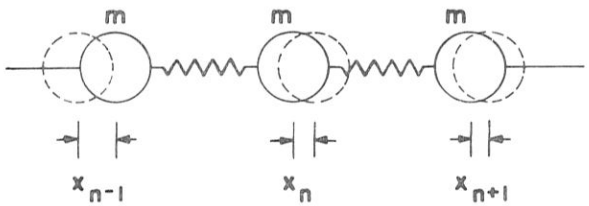

LINEAR LATTICE

LINEAR MODEL OF COUPLED CAVITIES

FIG. 1

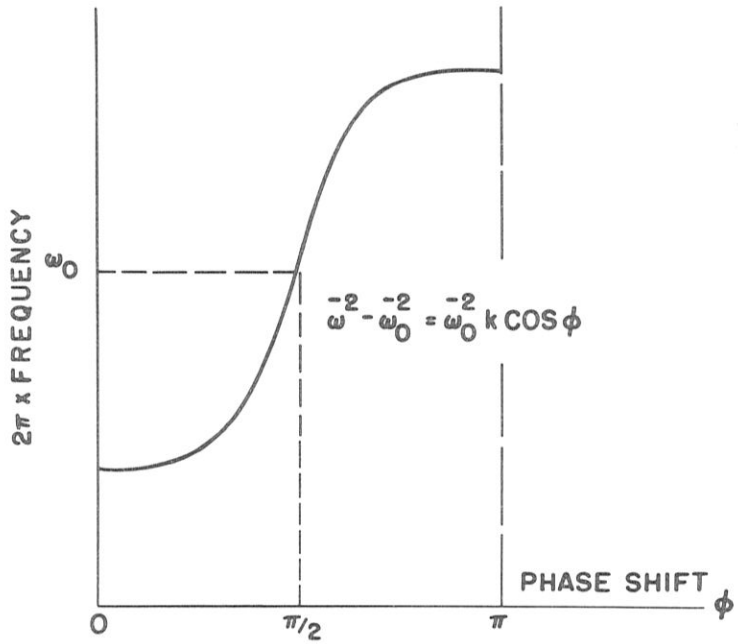

DISPERSION CURVE FOR SIMPLE CHAIN

FIG. 2

$$\text{Let } \vec{i} = \begin{pmatrix} i_1 \\ \cdot \\ \cdot \\ \cdot \\ i_N \end{pmatrix} \qquad \vec{I} = \begin{pmatrix} I_1 \\ \cdot \\ \cdot \\ \cdot \\ I_n \end{pmatrix}$$

$$\Omega = \begin{bmatrix} 1 & \frac{k}{2} & 0 & 0 & & \frac{k}{2} \\ \frac{k}{2} & 1 & \frac{k}{2} & 0 & & 0 \\ 0 & \frac{k}{2} & 1 & \frac{k}{2} & 0 & 0 \\ & & & & & \\ & & & & & \\ \frac{k}{2} & 0 & & 0 & \frac{k}{2} & 1 \end{bmatrix} \qquad \text{(ring)} \tag{6}$$

Circuit equations are

$$\omega_o^{-2}\, \Omega\, \vec{i} - \omega^{-2}\, \vec{i} = \omega_o^{-2}\, \vec{I}. \tag{7}$$

The normal modes $\vec{i^q}$ are the eigenvectors of the homogeneous problem, and the resonant frequencies of the modes are the eigenvalues.

Solution to inhomogeneous problem $I_s = 1 \times \omega_o^2$ is the Green's Function

$$G(r, s) = \sum_{\substack{\text{all} \\ \text{modes}}} \frac{\varphi^q(r)\, \varphi^q(s)\, w(q)}{\omega_q^{-2} - \omega^{-2}}$$

$w(q) = 1/2 \qquad q = 0 \text{ or } N$

$w(q) = 1 \qquad q = 1, 2, \cdots, (N - 1)$

i.e., this is the response of the tank at the r^{th} cavity to unit drive at cavity number s.

IV. Relation Between Travelling Waves in a Ring and Standing Waves in a Tank

Figure 3 illustrates the relation between travelling waves on a ring and standing waves in a tank. The circumference of the circle is divided into 2 N equal segments, representing 2 N cavities connected in a ring. The travelling wave solutions, eq. (4), satisfy the periodic boundary condition $i_{2N+1} = i_1$. They represent waves travelling counterclockwise around the ring. Now imagine the ring bisected by the line cutting cavities number 2 N and number N in half, fold the figure along this line and straighten out the half circle to get a line segment. Number the line so that

2 N	⟶	0
1	⟶	1
2 N - 1	⟶	1
2	⟶	2
2 N - 2	⟶	2
	etc.	

The line represents the tank, with caviites of 1/2 length at each end. The solutions (eq. (4)) map into

$$(i_p^q + i_p^{q*}) = \frac{1}{\sqrt{N/2}} \cos \frac{\pi p q}{N} \quad . \tag{8}$$

The running wave solutions (4) satisfy

$$\sum_{p=1}^{2N} i_p^{q*} i_p^r = \delta_{2N}(r - q) \tag{4'}$$

where $\delta_{2N}(x) = 1 \quad x = 0, \quad 2N, \quad 4N \cdots$

$= 0 \quad$ otherwise,

and the standing wave solutions satisfy

$$2 \sum_{p=o}^{N} w_p \cos \frac{\pi p q}{N} \cos \frac{\pi r p}{N} = \delta_{2N}(r - q) + \delta_{2N}(r + q) \tag{4''}$$

where $\begin{cases} w_p = 1 & p = 1 \cdots N - 1 \\ = 1/2 & p = 0 \text{ or } N . \end{cases}$

For the chain the circuit matrix is

$$\Omega = \begin{bmatrix} 1 & k & 0 & \cdot & \cdot & 0 \\ \frac{k}{2} & 1 & \frac{k}{2} & 0 & \cdot & 0 \\ 0 & \frac{k}{2} & 1 & \frac{k}{2} & \cdot & 0 \\ \cdot & & & & & \\ 0 & 0 & \cdot & \cdot & k & 1 \end{bmatrix} . \qquad (6')$$

V. Deviations from the Floquet Law

$$\varphi = \pi q/N .$$

In the presence of losses in the cavities, the above wave functions (8) are not exact. For example, in the π-mode, the first-order correction requires

$$\varphi_n = \frac{\pi q}{N} + \Delta\varphi_n \text{ where}$$

$$\Delta\varphi_{n+1} - 2\Delta\varphi_n + \Delta\varphi_{n-1} = \frac{2}{k Q \pi} .$$

This is plotted in Fig. 4. With the drive in the center, the cell-to-cell phase shift is a maximum in the center and decreases linearly. For $k = 0.1$, $Q = 20,000$ and a tank of 65 cells, the center-to-end phase shift is 28°. By cutting the cavities halfway between beam loaded and unloaded, the over-all change in phase shift would be 2.8°. Visscher's program shows 10° is quite all right.

VI. Perturbation Theory

We can use the ordinary first-order perturbation theory to calculate the effect of deviations in cavity geometry:

Unperturbed Circuit Equation

$$\omega_o^{-2} \Omega \vec{i} = \omega^{-2} \vec{i} . \qquad (7')$$

Now perturb resonant frequencies of cavities

$$\omega_o^{-2} (\Omega + \delta\Omega)(\vec{i} + \delta\vec{i}) = (\omega^{-2} + \delta\omega^{-2})(\vec{i} + \delta\vec{i}) ;$$

define

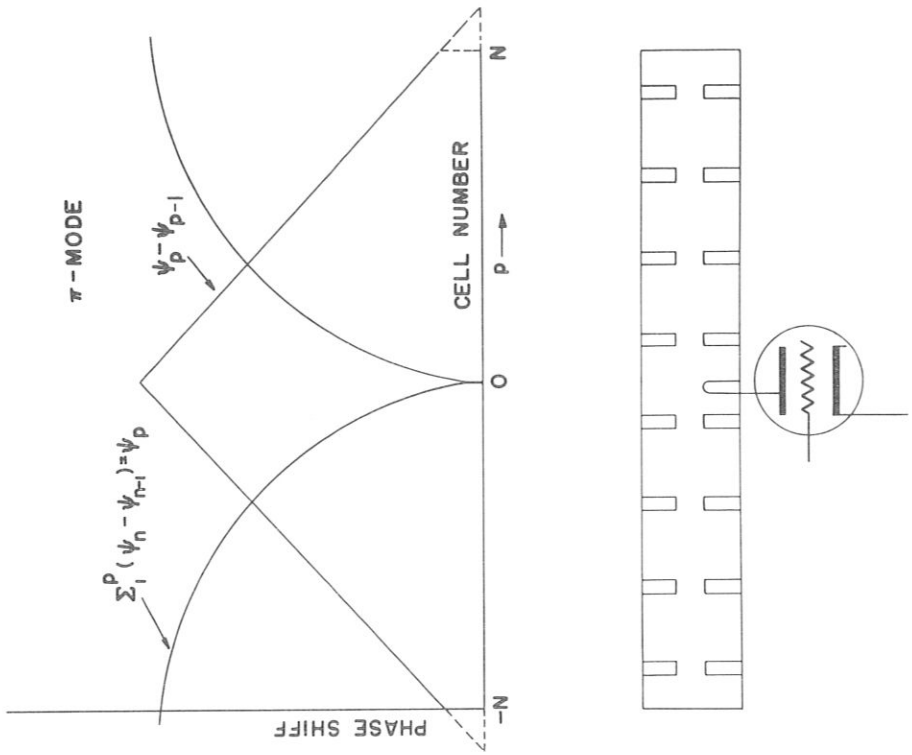

FIG. 4

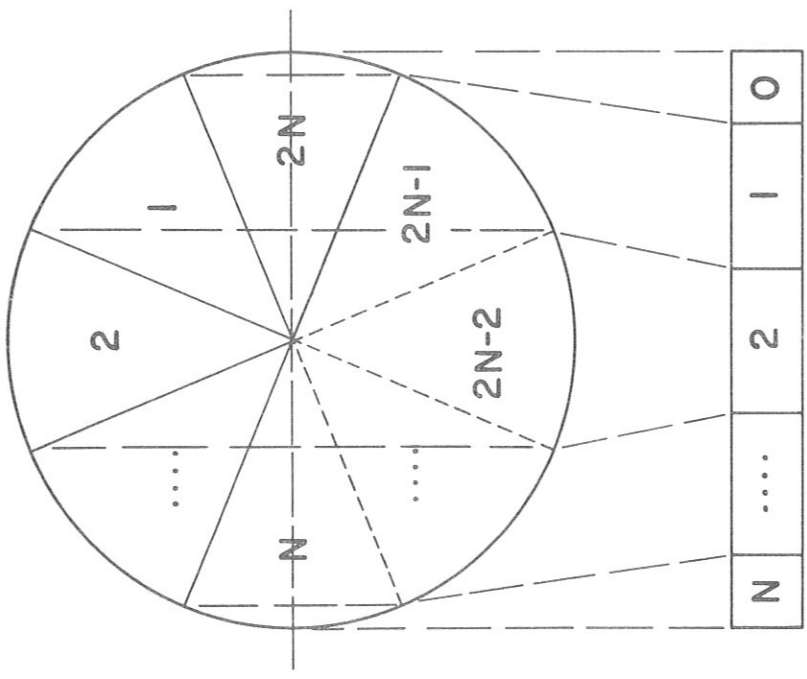

MAPPING OF THE RING
ONTO THE CHAIN

FIG. 3

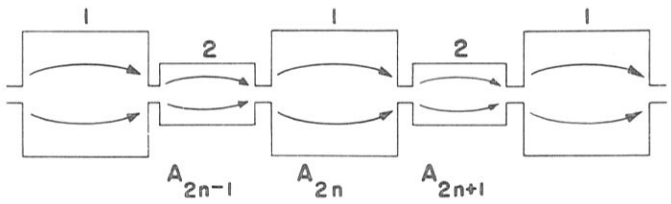

CAVITIES OF TWO KINDS

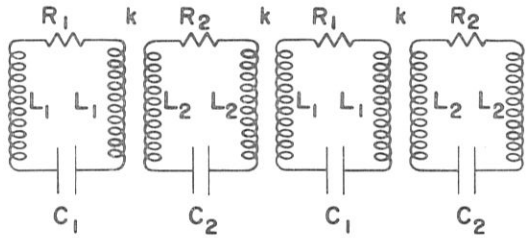

CIRCUITS OF TWO KINDS

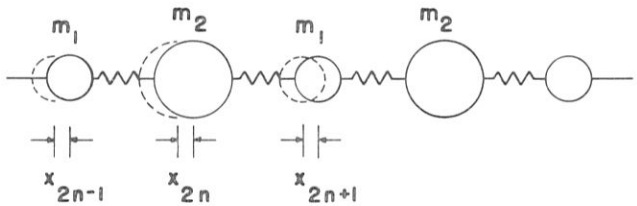

DIATOMIC LINEAR LATTICE

Fig. 5

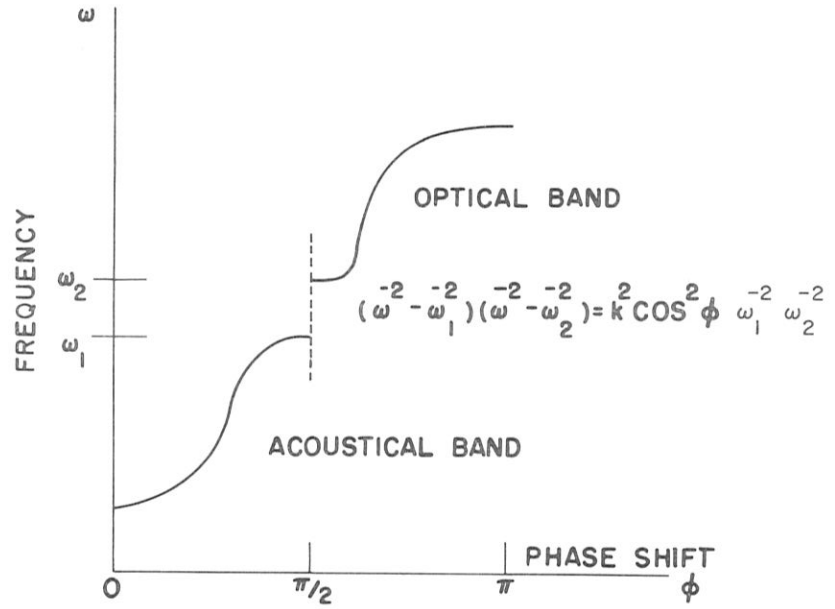

DISPERSION RELATION FOR CAVITIES OF TWO KINDS

Fig. 6

$$\omega_n^{-2} = \omega_o^{-2} (1 + \epsilon_n) .$$

First-Order Solutions

$$\delta\omega_\ell^{-2} = \omega_\ell^{-2} \left(\frac{1}{N} \sum_o^N \epsilon_n\right) \tag{9}$$

$$\delta \vec{i}^{\ell} = \sum_r \frac{\vec{i}^{\ell+r} \tilde{\epsilon}_r \left\{-1 + \frac{k}{2}\left(\cos\frac{2\pi Q}{N} - \cos\frac{2\pi r}{N}\right)\right\}}{k\left(\cos\frac{2\pi\ell}{N} - \cos\frac{2\pi r}{N}\right)} \tag{10}$$

where $\tilde{\epsilon}_r$ is the r^{th} Fourier Transform of the error. This is written for a ring, but the application to the line is straightforward. One sees k must be kept large.

VII. Circuits of Two Kinds

Many of the structures of interest, cloverleaf, crossbar, side coupled iris, loop coupled iris, etc., are of doubly resonant character. The cavities useful mode resonates at frequency ω_1, say, and the coupling region itself resonates at frequency ω_2. Thus in the cloverleaf the slots themselves have a resonance at the frequency ω_2. We may represent approximately the actual behavior by a very simple model, namely of circuits of two kinds, as shown in Fig. 5. The equations now become

$$\begin{aligned}
&(\omega_1^{-2} - \omega^{-2}) i_{2n} + \frac{k}{2}\omega_1^{-1}\omega_2^{-1}(i_{2n-1} + i_{2n+1}) = I_{2n}\omega_1^{-2} ; \\
&(\omega_2^{-2} - \omega^{-2}) i_{2n+1} + \frac{k}{2}\omega_1^{-1}\omega_2^{-1}(i_{2n} + i_{2n+2}) = I_{2n+1}\omega_2^{-2} .
\end{aligned} \tag{11}$$

There are solutions to $\vec{I} = 0$ of the form

$$\begin{aligned}
i_{2n} &= i_2 e^{2njq\varphi} \\
i_{2n+1} &= i_1 e^{(2n+1)jq\varphi} ,
\end{aligned} \tag{12}$$

if

$$(\omega_1^{-2} - \omega^{-2})(\omega_2^{-2} - \omega^{-2}) = k^2\omega_1^{-2}\omega_2^{-2}\cos^2 q\varphi . \tag{13}$$

This is the dispersion relation for the ring or chain of such resonators. It is shown in Fig. 6. It has two branches, known in lattice dynamics as the acoustical and optical branches.

There is a forbidden band of frequencies between the two branches. For $\omega_1 < \omega_2$ the lower $\pi/2$ mode corresponds to excitation of the main cavities +, -, +, -, $\cdots$, and zero energy in the coupling cells. This mode is called the π-mode if we use the simple model. The upper $\frac{\pi}{2}$ mode (energy in the coupling cells and none in the cavities) is missing for $\omega_1 < \omega_2$ because of the boundary conditions at the ends. The top of the acoustical band $\omega = \omega_1$, $\varphi = \pi/2$ turns out to be a useful operating point, as will be explained in the following paper. The fit of the measured points to this very simple model is remarkably close.

REFERENCES

1. L. Brillouin, Wave Propagation in Periodic Structures, Dover, New York (1953).

800 MEV RF STRUCTURES*

E. Knapp
Los Alamos Scientific Laboratory, University of California
Los Alamos, New Mexico

I would first like to say that the people who have been working on this are Bruce Knapp, Bill Shlaer, Jim Potter and myself. This report is certainly that of a joint effort.

For the successful construction of a high energy proton linear accelerator, anrf structure which provides an electromagnetic wave traveling with the velocity of the accelerating proton, which is insensitive to beam level in the accelerator, is easily monitored and controlled by the driving amplifier, and which has a minimum of power loss in its walls is necessary. It appears that a chain of cavities operating as a resonant structure, whose lengths are adjusted to provide the changing phase velocity required for the acceleration, best fulfills the above requirements. Due to the resonant cavity nature of the system, the axial dependence of the amplitude of the accelerating wave is not cirtically dependent on beam level as it would be in a traveling wave accelerator. It also has been possible to obtain structures which have good shunt impedances in a resonant mode and thus fulfill the efficiency requirement mentioned above.

Many structures which may be operated in π-mode have been proposed as accelerator elements. Among the possibilities are 1) an iris-loaded structure such as is used in a traveling wave application in the Stanford linear electron accelerators, 2) a crossed-bar structure suggested by Walkinshaw at Harwell and investigated by A. Carne there, 3) the cloverleaf structure discussed by Chodorow and Craig and investigated by A. Carne at Harwell, 4) a basket-weave structure such as has been suggested by Chodorow and Craig, 5) alternatively a set of loop-coupled pill-box cavities as have been discussed by the Harwell group, 6) modifications of many of the traveling wave amplifier tube structures, such as slow wave helices, which have been used successfully in that application. Structures which basically operate in the $\pi/2$ mode (resonant coupling, are also considered in this paper. Some work has been done on structures with resonant coupling loops by the Harwell group. A series of measurements on model cavities of the above types has been undertaken in order to choose a structure for use in the proposed linear accelerator meson facility at Los Alamos. In the following we will discuss in detail

---

*Work performed under the auspices of the U. S. Atomic Energy Commission.

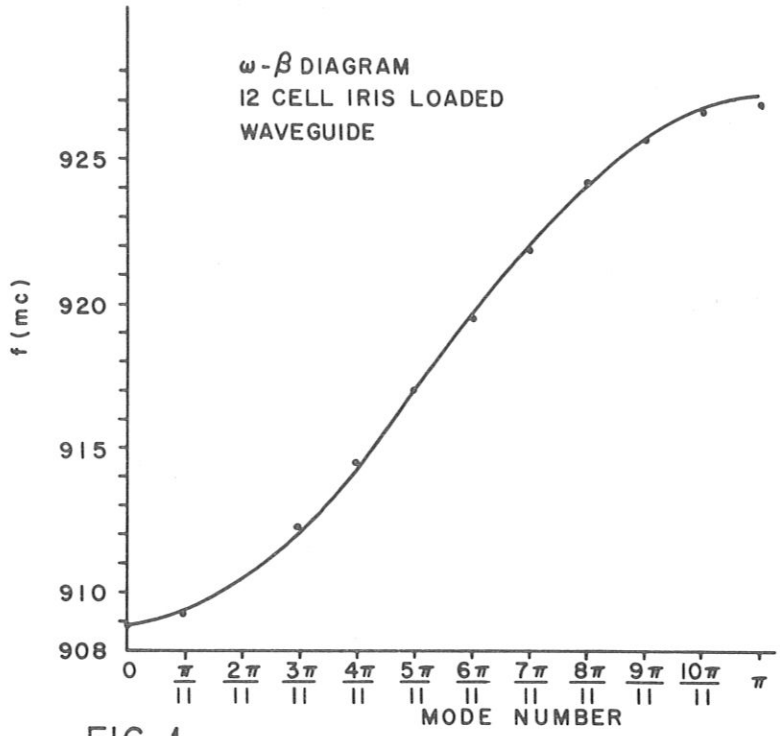
ω - β DIAGRAM
12 CELL IRIS LOADED
WAVEGUIDE
f (mc)
925
920
915
910
908
0
π/11
2π/11
3π/11
4π/11
5π/11
6π/11
7π/11
8π/11
9π/11
10π/11
π
MODE NUMBER

FIG. 1

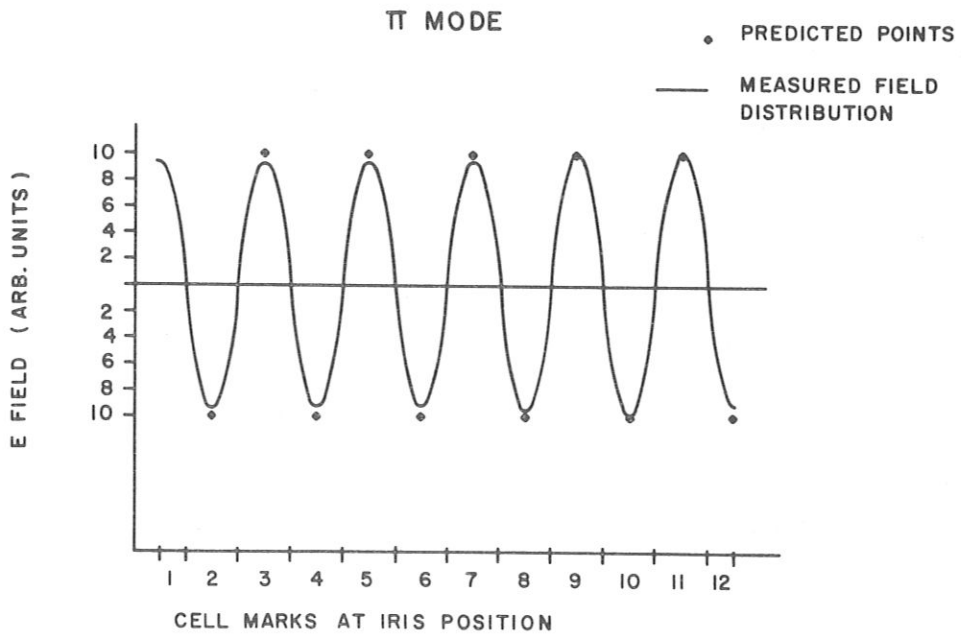
π MODE
PREDICTED POINTS
MEASURED FIELD DISTRIBUTION
E FIELD (ARB. UNITS)
10
8
6
4
2
2
4
6
8
10
1 2 3 4 5 6 7 8 9 10 11 12
CELL MARKS AT IRIS POSITION

FIG. 2

the cloverleaf structure mentioned above, and a possible $\pi/2$ mode configuration which exhibits good shunt impedance.

Electrical Properties of N Coupled Cavities

The electrical properties of n magnetically coupled lumped constant resonant circuits may be taken as a guide to the properties of n coupled cavities, with the appropriate identification of properties of the circuits to characteristics of the cavities. Such an analysis has been carried out and has been described in the previous paper. If there are N cells or cavities coupled together with a mutual inductance $M = k L$ where L is the self-inductance in each loop of the equivalent circuit, then there will be N resonant frequencies for the circuit as a whole, distributed in frequency as

$$1 - \frac{\omega_o^2}{\omega^2} + k \cos \phi = 0 \qquad (1)$$

where ω_o = individual cell frequency. The circulating currents in the individual loops have amplitudes

$$i_n = \cos \frac{\pi q n}{N} ,$$

where n is the cell number and q the mode number. In π mode for a lossless case (q = N) all currents are equal, there is a π phase change from cell to cell, and the separation of the $\frac{(N - 1)}{N}\pi$ mode from the π mode is

$$\frac{\Delta \omega}{\omega_o} = \frac{k \pi^2}{4 N^2}$$

for $k << 1$. Cleraly the coupling from cell to cell must be made as great as possible in order to keep good mode separation. If there are losses in the individual circuits, the phase change from cell to cell is no longer π, but $\pi - \Delta\phi$ where

$$\phi_{n, n+1} = \frac{2 (1 - k)}{k Q} \left(n + \frac{1}{2} \right)$$

or the phase shift across n cells is

$$\phi_{o, n} = \frac{(1 - k)}{k Q} n^2 \qquad (3)$$

where n = 0 is the cell furthest from the drive and the numbering is toward the cell into which energy is introduced. In order to keep the phase velocity of the accelerating wave correct, $\Delta\phi$ must not change appreciably with beam level, which means k must be as high as possible. Finally, in order to be able to effectively tune or flatten the tank, the theory also indicates k must be as large as possible. First-order perturbation theory indicates that the amplitude error associated with a frequency error distribution

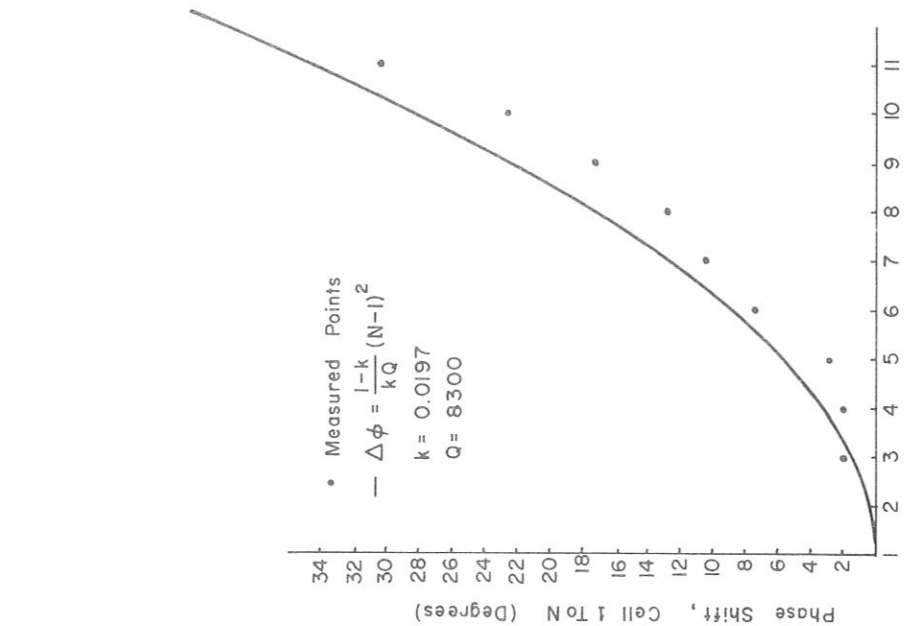

FIG. 3 Cell Number

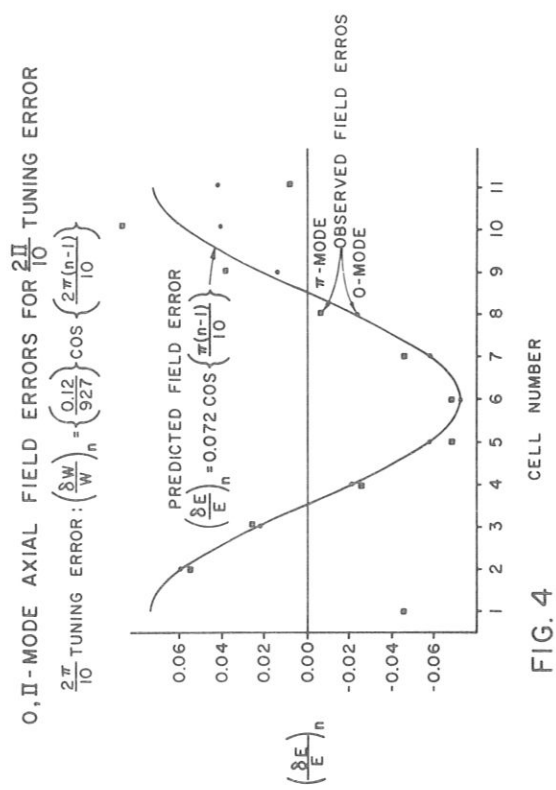

FIG. 4

$$\tilde{\epsilon}_r = \frac{2\,W(r)}{N} \sum_{p=0}^{N} W(p)\ \epsilon_p \cos\frac{\pi p r}{N} \tag{4}$$

where $W(p) = \frac{1}{2}$, $p = 0, N$

$$W(p) = 1, \quad p \neq 0, N$$

$$\epsilon_p = \left(\frac{\omega_{op}^2 - \omega_o^2}{\omega_o^2} \right)_{p^{th}\ \text{cell}}$$

is

$$\delta i_n^q = \sum_{r=1}^{N} \tilde{\epsilon}_r \frac{1}{2} \left\{ \frac{W(q-r)}{W(r)}\ a_r \cos\frac{\pi(q+r)n}{N} + \frac{W(q+r)}{W(r)}\ a_{-r} \cos\frac{\pi(q-r)n}{N} \right\} \tag{5}$$

where $a_r = \left\{ \left(\frac{\omega_o}{\omega_{q+r}} \right)^2 - \left(\frac{\omega_o}{\omega_q} \right)^2 \right\}^{-1}$.

For a π mode

$$\frac{\delta I_n^N}{I_n^N} = \frac{1}{k} + \sum_{r=1}^{N} \tilde{\epsilon}_r \frac{\cos\frac{\pi r n}{N}}{1 - \cos\frac{\pi r}{N}} \tag{6}$$

and for $\pi/2$ mode we have

$$\frac{\delta I_n^{n/2}}{I_o^{N/2}} = -\frac{1}{k} \sum_{r=1}^{N} \tilde{\epsilon}_r \frac{W(N/2 - r)}{\sin\frac{\pi r}{N}} \sin\frac{\pi n}{2} \sin\frac{\pi r n}{N}. \tag{7}$$

These relationships have been verified for a 12-cell iris-loaded cavity to better than 5% accuracy. Here k is identified with the bandwidth of the structure

$$k = \frac{\omega_{(\pi)} - \omega_{(o)}}{\omega_{AVE}}$$

as would be indicated by Eq. (1). The current in Eq. (2) has been experimentally identified with the electric field at the center of individual cells.

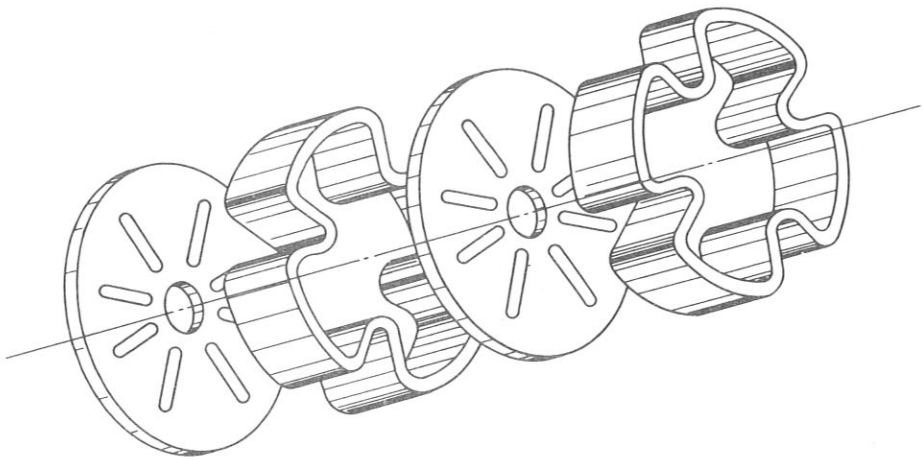

800 MEGACYCLE
CLOVERLEAF COMPONENTS

FIG. 5

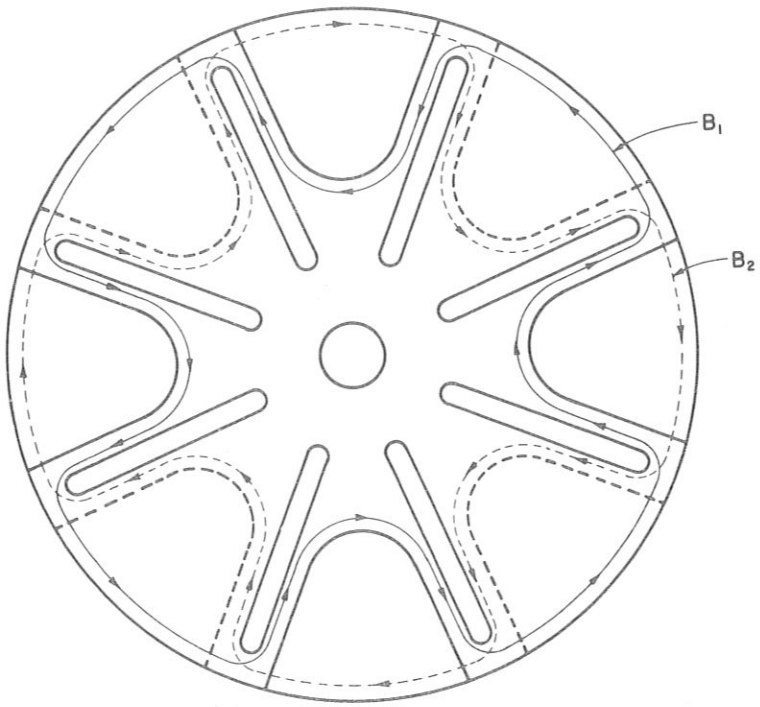

FIG. 6

Figure 1 shows the dispersion curve for a 12-cell iris-loaded waveguide resonator, compared to the predicted curve for k = 0.0197. Figure 2 shows the predicted center cell amplitudes vs measured field distributions for the π mode in the structure. Figure 3 shows the measured phase shift vs predicted phase shift for Q = 8300. Figure 4 shows a comparison of the measured and predicted ampltiude distributions for programmed tuning errors in the cavities.

The above theory suffices for an iris-loaded waveguide. However, in many instances the coupling mechanism itself may have resonances near the cavity resonant frequency. For this reason we have considered a chain of coupled resonators as before, but now alternating with frequencies ω_1 and ω_2, as also described in the previous paper. We then find a dispersion relation

$$\left(\omega^2 - \omega_1^2\right)\left(\omega^2 - \omega_2^2\right) = \omega^4 K^2 \cos^2 \phi \qquad (8)$$

where now ϕ is the phase change from cell to slot, say, and K is identified with the coupling of slot to cell. K may be identified with the full passband width if $\omega_1 = \omega_2$. The dispersion curve for a structure of this type displays a stop band as discussed in the previous paper. While the behavior of a chain of circuits such as this is somewhat more complex for the general case, an effective coupling constant k_{eff} may be defined to allow use of the single resonant frequency theory of phase shifts near the $\pi/2$ mode of the multiply resonant structures. This coupling constant may be defined by making a Taylor expansion of the dispersion curve near the $\pi/2$ mode for the multiply-periodic circuit and matching this to a symmetric dispersion curve as obtained in the theory for a chain of resonant cavities with a single resonant frequency. Carrying this out we find that

$$k = \frac{K^2}{2\,(P - 1) + K^2} \qquad (9)$$

where $P = \omega_1^2 / \omega_2^2$.

The validity of this approximation has been investigated for the phase shift problem with computer runs and on experimental models and agrees very well with the observed results. For the perturbation theory, agreement with experiment seems excellent also.

In general, we find k's considerably bigger than the measured bandwidth, which would intuitively be the case since the dispersion curves are quite asymmetric. We shall refer to these expressions often as we describe the experimental results obtained.

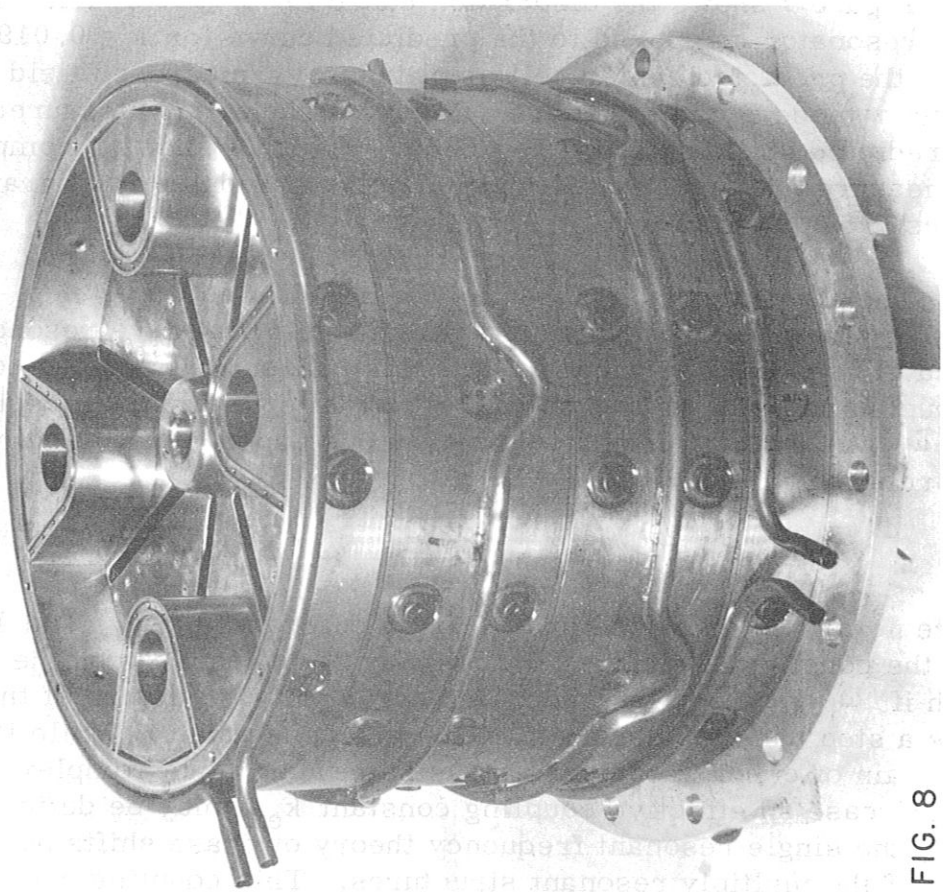

FIG. 8

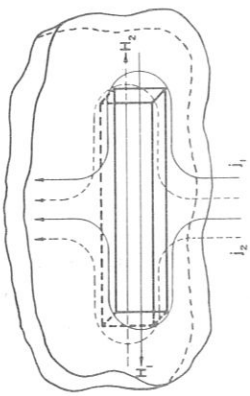

MAGNETIC FIELD OPPOSITE ON EACH SIDE OF SLOT

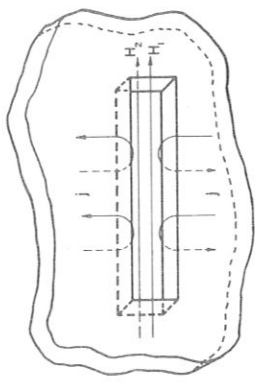

MAGNETIC FIELD IN SAME DIRECTION ON EACH SIDE OF SLOT

FIG. 7

Accelerator Efficiency

The efficiency of a resonant cavity as a particle accelerating device may be measured by considering the power required to provide a given acceleration; it is usually expressed in terms of the effective shunt impedance

$$ZT^2 = \frac{(\text{energy gain/meter})^2}{\text{power dissipated/meter}} = \frac{\text{ohms}}{\text{meter}}$$

where the energy gain is taken for a particle located in the center of the accelerating gap at peak electric field.

$$ZT^2 = \frac{\left(\int E(z,t)\, dz\right)^2}{P\, L} \qquad (10)$$

where P = power dissipated in cavity, L = cavity length, and the integral is taken with the particle at the center of the cell at peak field.

The two most important criteria to be met by a π mode accelerating structure are that it have a large bandwidth (large k), and that the shunt impedance ZT^2 be as great as possible. In addition to these two criteria, it is reasonable also to expect the structure to develop no large electric fields in the mechanism used for coupling from cell to cell and not to present unsurmountable alignment or fabrication problems.

Structures Considered

Most of the mentioned type structures have been at least given a cursory examination with models using reasonable geometrical parameters. However, we have defined our principal investigation to two structures which look most promising to us, the cloverleaf π-mode structure and a version of a $\pi/2$ mode structure. Other laboratories are investigating most of the other structures more thoroughly than we could, so we will not comment on our results with these structures at this time.

CLOVERLEAF STRUCTURE

Historically the cloverleaf structure was invented for a traveling wave tube application by Chodorow and Craig and has been used commercially (Varian Assoc.) as an active element in a high power S-band traveling wave tube (types VA 125, VA 126, VA 145). Tube type VA 145 amplifies to 7 MW peak over an 8% bandwidth near 3 kMc. Other commercial tubes may be available of which we are not aware.

FIG. 9

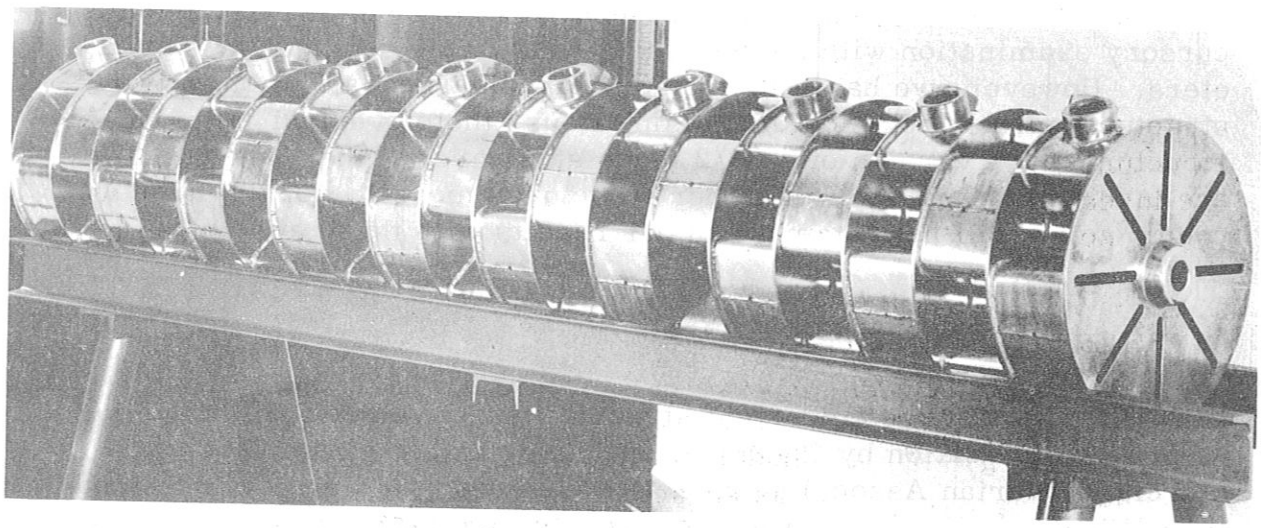

FIG. 10

Alan Carne from the Rutherford Laboratory has reported some studies on this structure as a possible element for a proton linear accelerator (Dubna Conference), and it was these measurements which drew our attention to this structure. As far as we know, no other measurements have been made for proton accelerator application of this structure.

Figure 5 shows an exploded view of the cloverleaf chain as envisioned by Chodorow and Craig. The periodicity operation in the cloverleaf is a translation by a cell length L and a rotation by 45°, as is indicated in more detail in Fig. 6.

Electromagnetically, the cloverleaf operates qualitatively as follows: Radial magnetic field lines are produced in the TM_{010} mode of a cylinder by deformations or noses in the walls of a cylindrical cavity at 90° intervals around its circumference. These radial fields may then be used to efficiently couple energy from one cell of the cloverleaf to the next by placing slots along these field lines. Eight slots are radially placed at 45° intervals straddling the noses protruding into the volume. On the other side of the septum we may have a 45° rotation of the cavity (forward wave structure) or 0° rotation of the structure (backward wave structure). For use as a standing wave accelerator structure, it is immaterial whether the structure is forward or backward wave. However, slot field levels and effective coupling strengths are important, and these are both favorable in the forward wave configuration for π-mode operation. In π mode with 45° rotation of the noses the radial fields are in the same direction on both sides of the slot. Figure 7 illustrates the current configurations near the slots in the cloverleaf for the zero mode (magnetic field opposite across slot) and π mode (magnetic field in same direction on each side of slot) in the forward wave configuration. The wall currents are clearly strongly perturbed in the zero mode and virtually unperturbed in the π mode, indicating a lowering of the zero mode frequency relative to that of the π mode (forward wave structure), and indicating that in π mode very little electric field will be developed across the slot. Energy transfer may be considered as a current interchange through the slot with almost no perturbation of the cavity mode fields in the process. The advantages we see in the cloverleaf as a standing wave accelerator structure are:

1. Coupling not dependent on beam aperture configuration.
2. Strong coupling available in π mode standing wave operation.
3. No strong electric fields present in coupling mechanisms.
4. Excellent shunt impedance possible, especially with capacitive loading in the cavities.

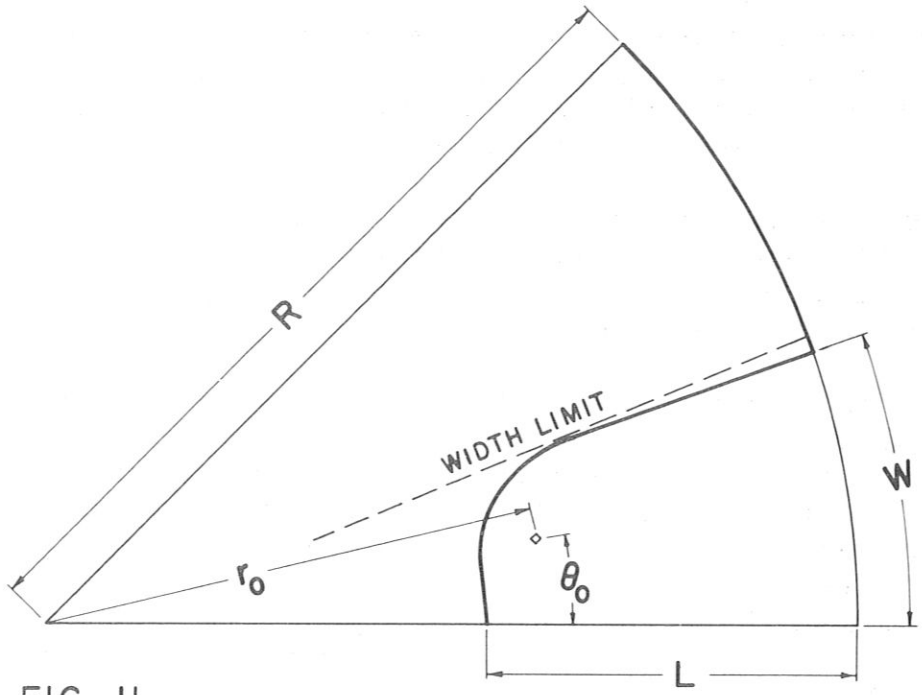
R
WIDTH LIMIT
W
r_o
θ_o
L

FIG. 11

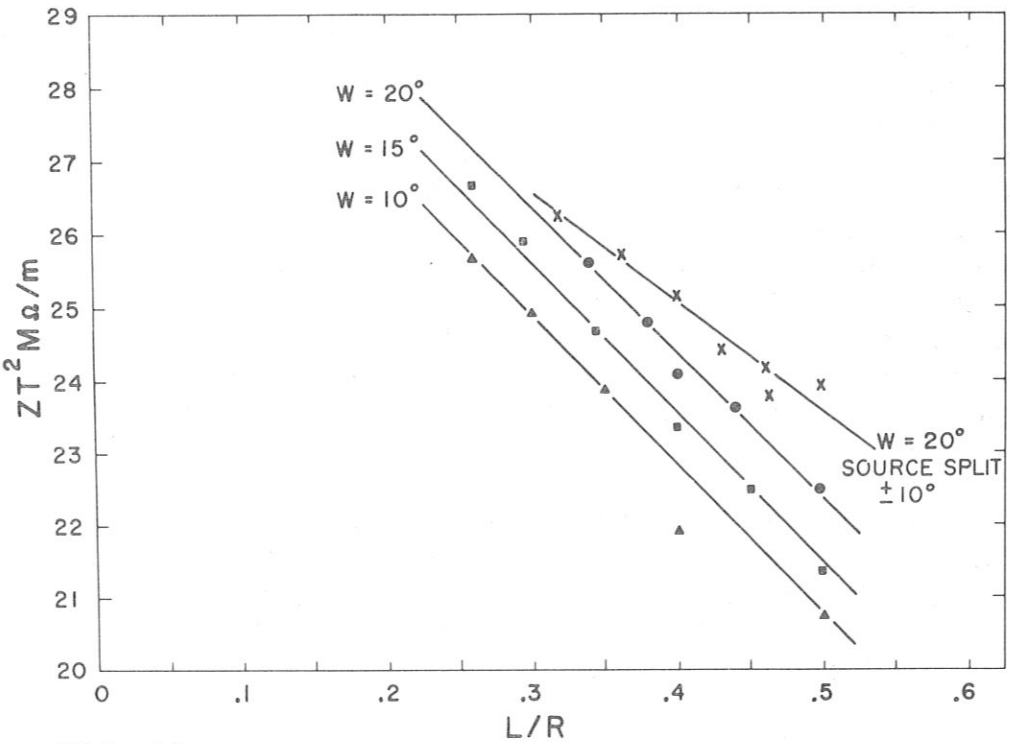
29
28
27
26
25
24
23
22
21
20
ZT^2 MΩ/m
0
.1
.2
.3
.4
.5
.6
L/R
W = 20°
W = 15°
W = 10°
W = 20°
SOURCE SPLIT
±10°

FIG. 12

In order to investigate the properties of the cloverleaf more fully, we have constructed several models and measured their properties. Figure 8 shows a photograph of a demountable carefully machined model on which most of the optimizing studies have been done. This model allows the septum configuration to be changed at will, allowing studies of slot dimensions, beam hole size and configuration, and so on to be made. This model does not allow changes to be made in nose dimension. Also this model, because of its demountable joints, does not allow reliable Q measurements to be made; however, Z/Q measurements are quite reliable.

In order to make reliable Q measurements, several models were made up of two cells and two half cells (similar to the demountable configuration) in which all joints were brazed. These were manufactured by pressing 1/16-inch copper sheet in quadrants to form the cloverleaf walls, and heli-arc brazing the parts together with Sil-Fos solder. Using this same technique several single cell cloverleaf cavities were constructed also. Figure 9 shows a representative cavity of this type.

Figure 10 shows a 21-cell tank made by the same technique as above. This tank has been designed rather conservatively and has been used so far to check out the results of the shorter model studies and the predictions of the coupled circuit theory.

OPTIMIZATION OF NOSE SHAPE

Bill Shlaer at this laboratory has developed a computational program that allows calculation of electric and magnetic fields in a resonator similar to the cloverleaf. The fields in these resonators are generated by line currents oscillating at 800 Mc and located symmetrically in quadrants of a metal cylinder. The fields are assumed z-independent. In many respects this calculation is similar to that done by R. Gluckstern for drift tube and iris structures. Figure 11 shows the configuration of line currents (shown at position r_o and θ_o in an octant). The resultant fields may be varied by varying the cylinder radius and source radius. For certain ranges of these parameters, there is a zero of the electric field along which a new boundary may be drawn that will separate the currents from the rest of the cylinder. This remainder is resonant at 800 Mc with the same field distribution and may have the shape of a cloverleaf. These calculations do not include slots, beam holes, or any z-asymmetries. However, they do allow optimization of lobe shape for a given lobe penetration. Figure 12 shows shunt impedances calculated vs nose penetration L/R with nose width as a parameter. One family of flat-nosed lobes is included. It appears that for minimum losses, flat-nosed lobes are to be preferred with maximum width possible. These

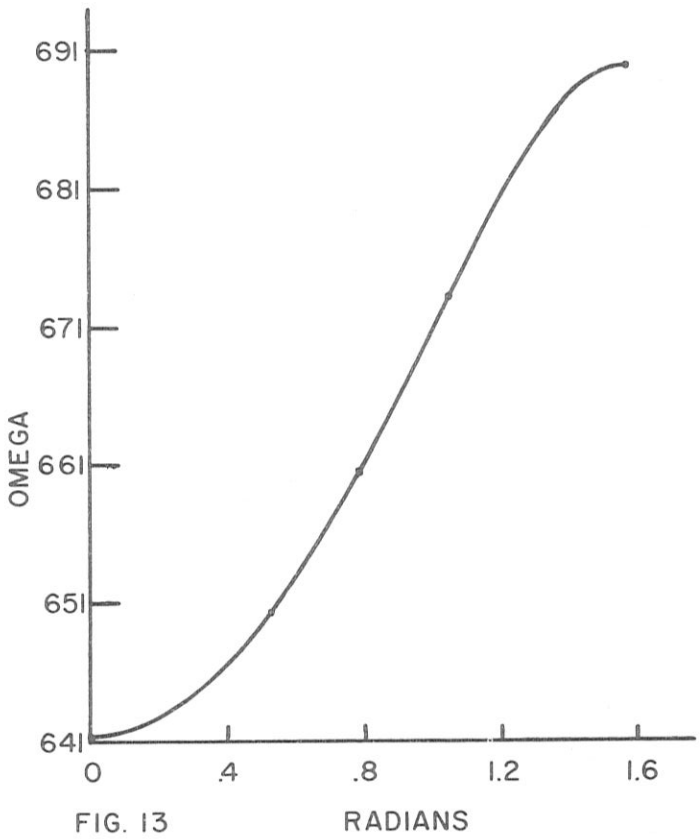
691
681
671
661
651
641
OMEGA
0
.4
.8
1.2
1.6
RADIANS

FIG. 13

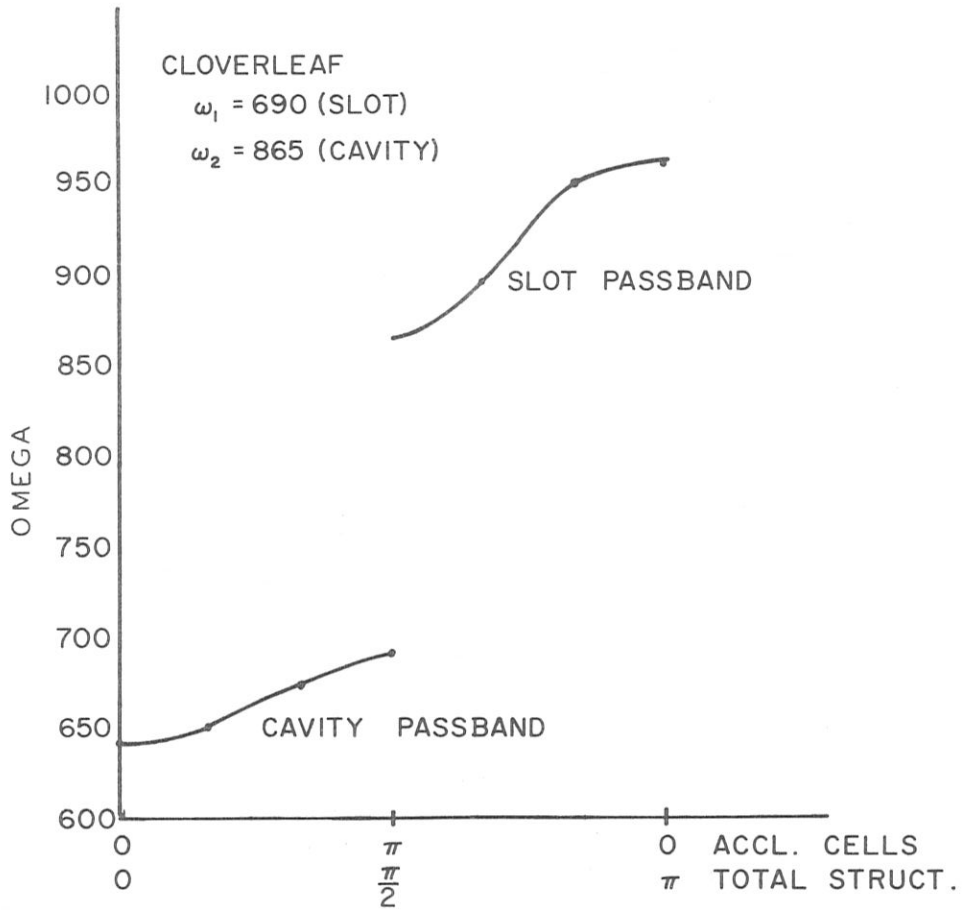
CLOVERLEAF
ω_1 = 690 (SLOT)
ω_2 = 865 (CAVITY)
1000
950
900
850
800
750
700
650
600
OMEGA
SLOT PASSBAND
CAVITY PASSBAND
0
0
π
$\frac{\pi}{2}$
0 ACCL. CELLS
π TOTAL STRUCT.
MODE

FIG. 14

calculations have been checked at two points with single cell cloverleaf cavities, and the quantities measured agree with calculated values quite well.

COUPLING STUDIES

The coupled circuit theory has been used extensively to analyze the behavior of the cloverleaf as far as its dispersion curve, tuning sensitivity, phase shifts and other electrical behaviors are concerned. It should be clear that the coupled circuits of two kinds with frequencies ω_1 and ω_2 certainly approximate the cloverleaf, with frequencies ω_1 associated with the cavities and ω_2 associated with the slots. Figure 13 shows a dispersion curve fitted to five data points taken from the demountable cloverleaf model. In this case, the cavity was capacitively loaded so that π mode frequency was 690 Mc/sec. This is a five-point fit to a three-parameter function (ω_1, ω_2, K); the maximum deviation of any point from the fitted curve is 28 kc which is only a little larger than measurement accuracy (full Q width at 3 db = 50 kc). We would thus say the theory fits the performance of this cloverleaf model exceedingly well. Many other model configurations have been fit and almost all agree this well with the theory. The upper branch of the passband may also be observed, and although the fit is no longer as good if these data points are included, indications are that the theory does adequately describe the observations. Fits with deviations to about 1 Mc are observed for this procedure. The presence of higher cavity modes not orthogonal to the slot mode, which couples the cavities in the TM_{010} mode, can effectively change the position of the upper branch somewhat. Figure 14 shows a fit of this type. In this case, the data are the same as in Fig. 13, but the slot mode points have been included. If ω_{cavity} is greater than ω_{slot}, the relative positions of the passbands are reversed and the structure becomes a backward wave device. Figure 15 illustrates this.

The important parameter as far as coupling is concerned is the effective bandwidth k_{eff} defined previously. As was mentioned this parameter enters strongly in the mode separation, phase shifts, and flattening sensitivity of the structure. Figure 16 shows a plot of k_{eff} vs slot length and width for the demountable cloverleaf, this time with no capacitive loading. The π mode frequency is 840 Mc. This curve is derived from the dispersion curve data points by fitting these points to the theoretical expressions to obtain K, ω_1 and ω_2, and then calculating k_{eff} from these parameters. It is found that the parameter K, yielding the coupling from slot to cavity, is virtually independent of slot configuration. This might be expected since the slot is very tightly coupled to the cavity fields, almost independent of its dimensions. With this information, it is clear from the figure that the effective coupling

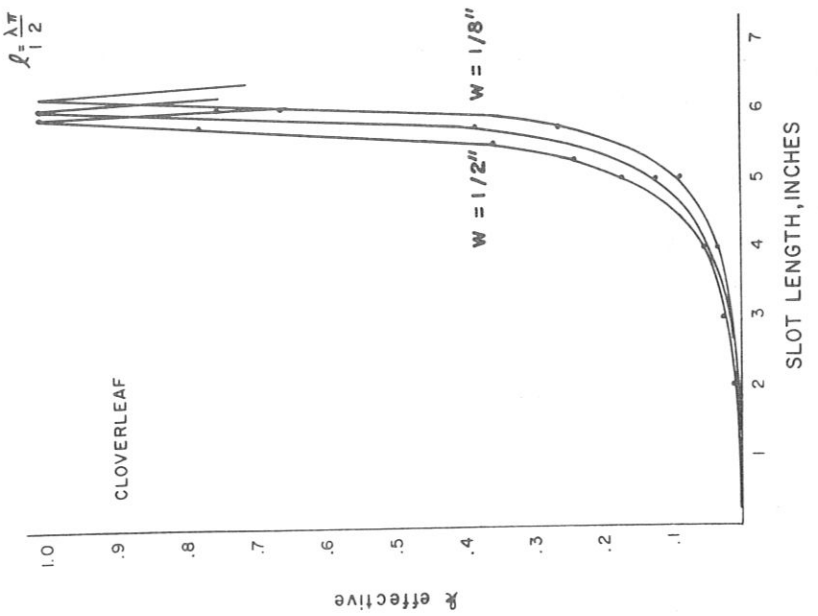
$\beta = \frac{\lambda\pi}{l\,2}$
CLOVERLEAF
W = 1/2"
W = 1/8"
β effective
SLOT LENGTH, INCHES

FIG. 16

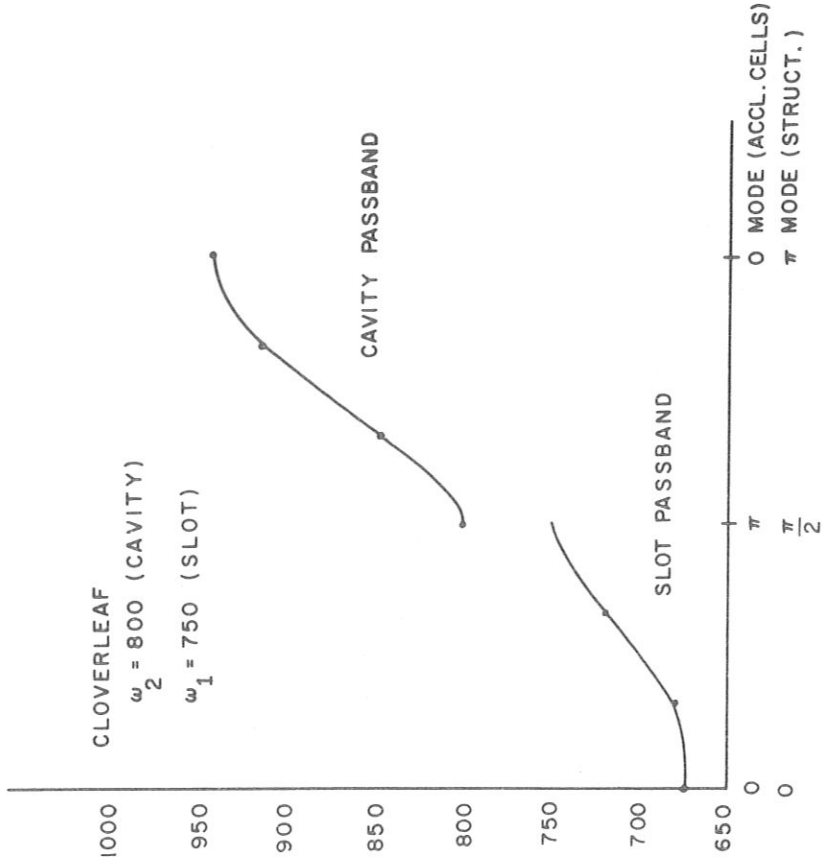
CLOVERLEAF
ω_2 = 800 (CAVITY)
ω_1 = 750 (SLOT)
CAVITY PASSBAND
SLOT PASSBAND
OMEGA
0 MODE (ACCL. CELLS)
π MODE (STRUCT.)

FIG. 15

depends almost entirely on the resonant frequency of the slot. The dependence on width appears only as a change in resonant frequency with length (the effective length of the slot being somewhat longer than the actual length, the wider the slot the longer the effective length). At the slot length where the cavity frequency and the slot frequency are equal $k_{eff} = 1$, there are no phase shifts down the system, and the structure behaves as a $\pi/2$ mode structure as far as flattening and stability are concerned. It might be noted at this juncture that at resonance the slots should not have any appreciable electric field present, for a $\pi/2$ mode structure stores no energy in alternate cells in standing wave operation. For slot lengths giving resonant frequencies higher than the cavity frequency, very reasonable effective coupling constants may be obtained. Computer studies indicate very loose tolerance requirements are necessary on slot dimensions in order to get satisfactory performance. Even at resonance, variations of several megacycles in slot resonant frequency (like 0.025" in slot length) should have virtually no effect on performance.

As the accelerating cells get shorter, we should expect K to increase, yielding somewhat higher k_{eff} for the same slot length at lower energies.

Optimization of Shunt Impedance

The equation for shunt impedance may be written

$$ZT^2 = \frac{\left(\int E(z,t)\,dz\right)^2}{P\,L} = \frac{\left(n\int_o^{\ell} E(z)\sin\frac{\pi z}{\ell}\,dz\right)^2 Q}{\omega U\, n\ell}$$

where $Q = \frac{\omega U}{P}$, U = total stored energy in cavity, ℓ = cell length, L = cavity length, $n\ell = L$. The quantity ZT^2/Q may be evaluated using standard perturbation techniques (1). For a spherical metallic bead of radius r_o on the axis of a cavity of the type considered,

$$\frac{ZT^2}{Q} = \frac{\left(\int \left(\frac{\Delta f}{f}\right)^{1/2} \sin\frac{\pi z}{\ell}\,dz\right)^2 n}{\epsilon_o\,\pi\, r_o^3\,\omega} \qquad (11)$$

where $\frac{\Delta f}{f}$ = fractional resonant frequency shift produced at position z. It should be noted that this quantity is dependent upon geometrical factors only; losses in the cavity walls do not enter the expression. From a practical point of view, this means that errors in the values of ZT^2/Q

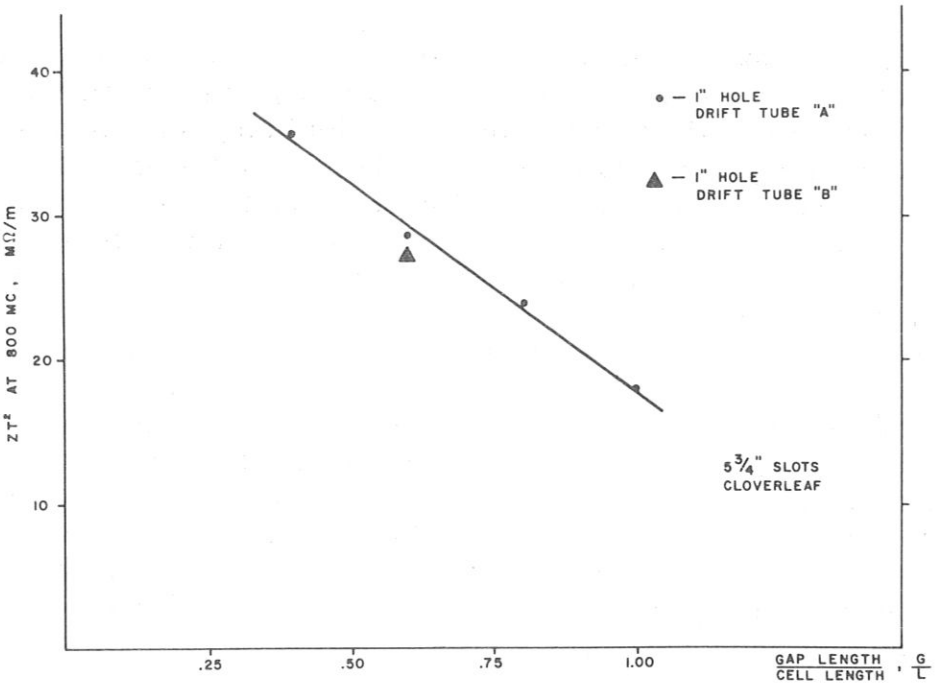

VARIATION OF SHUNT IMPEDANCE WITH DRIFT TUBE PARAMETERS

FIG. 17

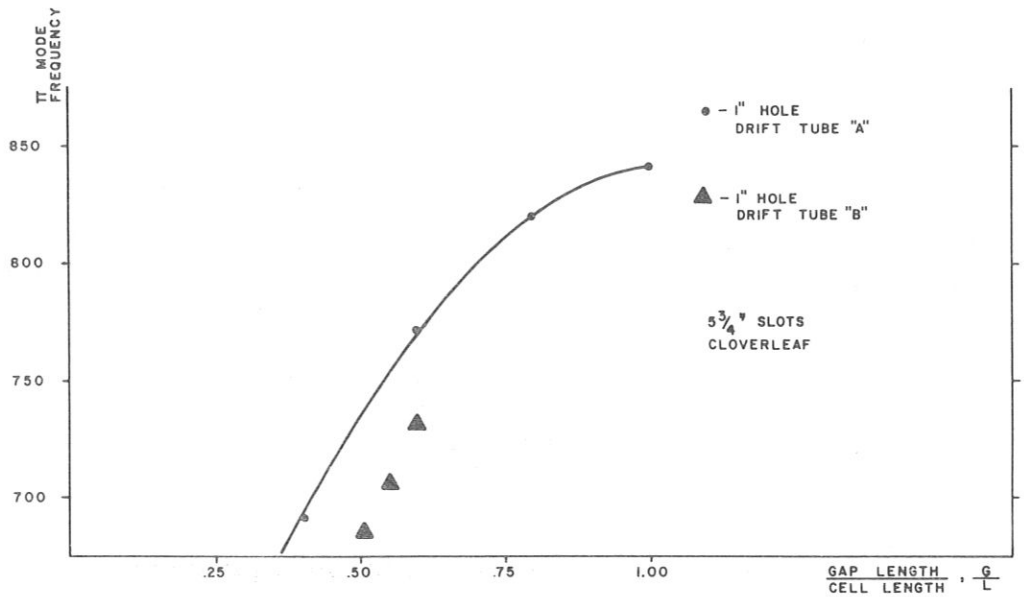

VARIATION OF π MODE FREQUENCY WITH DRIFT TUBE PARAMETERS

FIG. 18

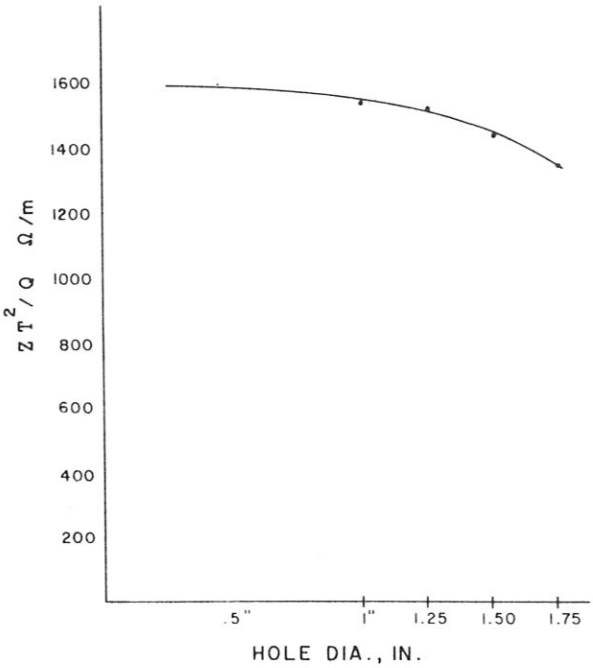
1600
1400
1200
1000
800
600
400
200
ZT^2/Q Ω/m
.5"
1"
1.25
1.50
1.75
HOLE DIA., IN.

FIG. 19

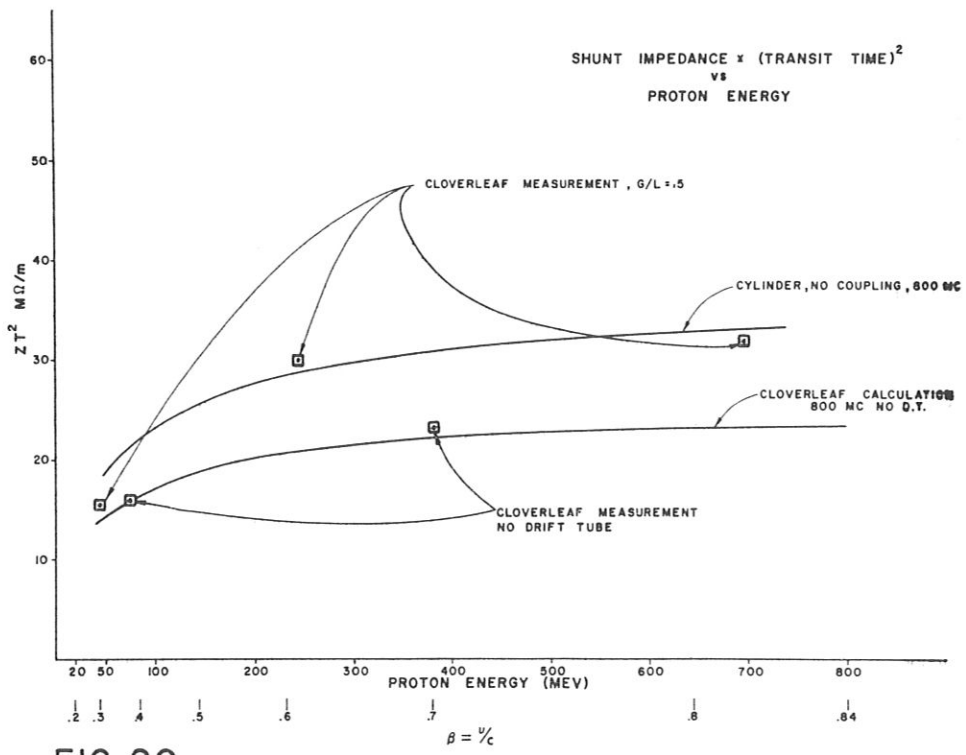
SHUNT IMPEDANCE x (TRANSIT TIME)^2
vs
PROTON ENERGY
CLOVERLEAF MEASUREMENT, G/L = .5
CYLINDER, NO COUPLING, 800 MC
CLOVERLEAF CALCULATION
800 MC NO D.T.
CLOVERLEAF MEASUREMENT
NO DRIFT TUBE
ZT^2 MΩ/m
60
50
40
30
20
10
20 50 100 200 300 400 500 600 700 800
PROTON ENERGY (MEV)
.2 .3 .4 .5 .6 .7 .8 .84
$\beta = v/c$

FIG. 20

FIG. 21

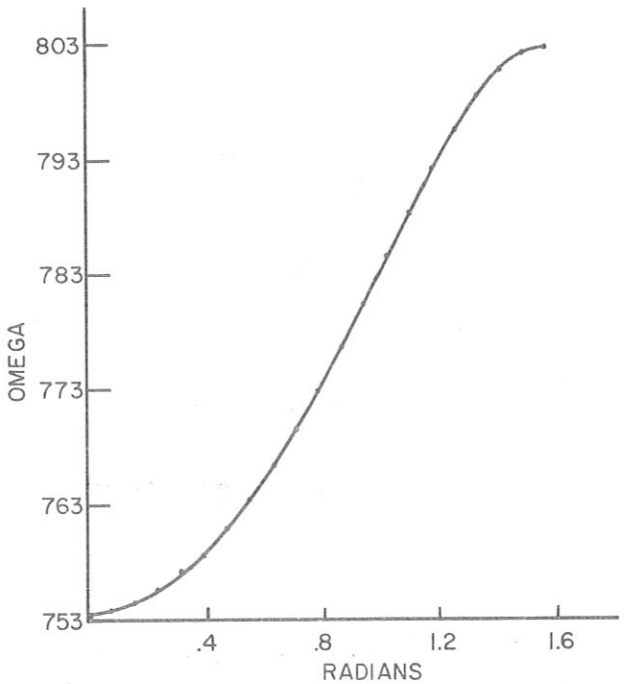

FIG. 22 21 Cell Air Model Cloverleaf Axial Field Flat To 1 Per Cent

obtained with demountable models are not dependent to any great extent upon the quality of the current joints attainable, and a relatively great trust may be placed in values obtained in somewhat crude models. However, to determine the effective shunt impedance accurately, an accurate determination of Q as well as ZT^2/Q is necessary. This is not a trivial problem, for the Q of a cavity depends very critically on the quality of the current joints in that cavity. Great pains have been taken to make high quality current joints in the demountable models tested, and even then variations on the order of 10% may be observed from one assembly to the next for identical configurations. In general, we can say that the values of ZT^2 quoted are lower than those realizable in cavities with all brazed joints, perhaps as much as 10% low. Q has been measured by measuring the power transmitted through a cavity as a function of frequency. With a highly undercoupled situation (small coupling loops) the frequency width of the half power points yields Q directly.

$$\left(\frac{\Delta f}{f}\right)_{1/2 \text{ power}} = \frac{1}{Q}$$

Other methods have been used, but this is the simplest and is accurate enough for the measurements we wish to make.

Variation of Shunt Impedance with Drift Tube Parameters

A reasonable way to increase the shunt impedance of the cloverleaf structure is to add drift tubes to the center of the septum walls in order to increase the transit time factor T^2 and to concentrate the stored energy in the cavity near the axis, effectively increasing Z/Q as well as T^2. Measurements have been made on the demountable model for two different shaped drift tubes. Figure 17 shows the variation of shunt impedance observed with g/ℓ (the ratio of gap length to cell length) for a 1" beam aperture. These results have been scaled to 800 Mc. Figure 18 shows the variation of π mode frequency. Figure 19 shows the variation of shunt impedance with hole size for $g/\ell = 0.6$. It is apparent that a large improvement in shunt impedance may be produced with the addition of drift tubes to the structure.

Several models with formed walls and all brazed construction have been fabricated to get reliable values of Q and ZT^2 for geometries which might be considered as elements in an accelerator. These models show Q's within 5% of theoretical for geometries where calculations are available.

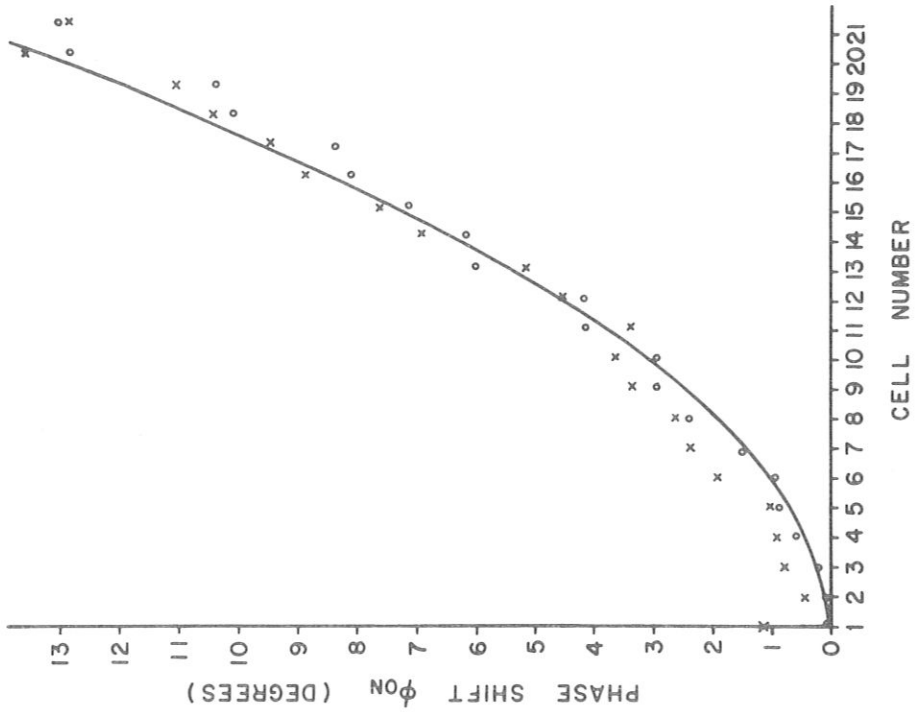
PHASE SHIFT ϕ_{ON} (DEGREES)
0
1
2
3
4
5
6
7
8
9
10
11
12
13
1 2 3 4 5 6 7 8 9 10 11 12 13 14 15 16 17 18 19 2021
CELL NUMBER

FIG. 24

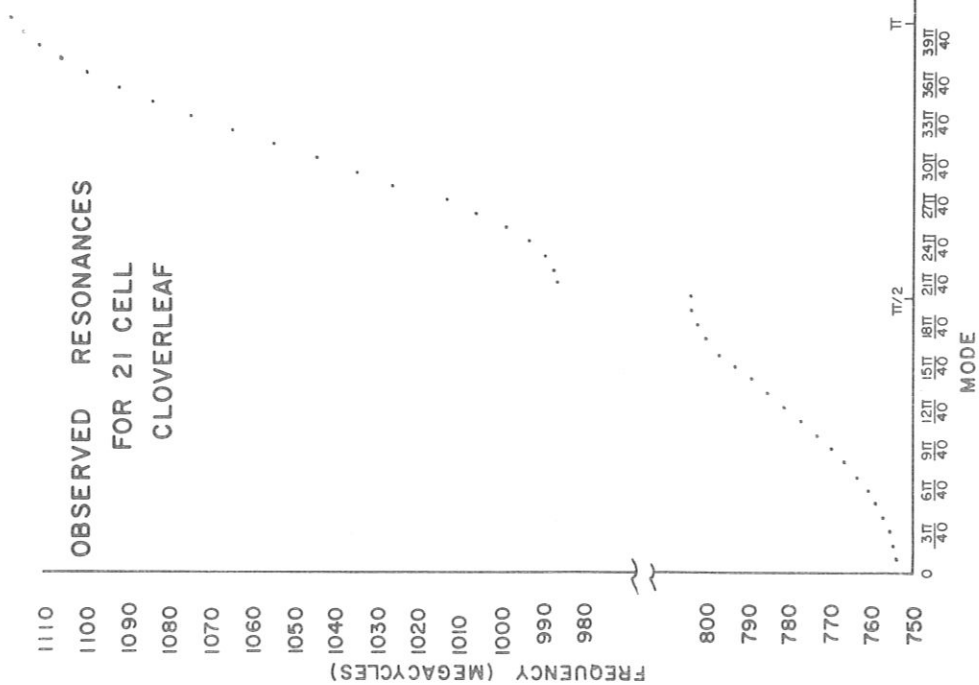
OBSERVED RESONANCES
FOR 21 CELL
CLOVERLEAF
FREQUENCY (MEGACYCLES)
1110
1100
1090
1080
1070
1060
1050
1040
1030
1020
1010
1000
990
980
800
790
780
770
760
750
0
3π/40
6π/40
9π/40
12π/40
15π/40
18π/40
21π/40
24π/40
27π/40
30π/40
33π/40
36π/40
39π/40
π/2
π
MODE

FIG. 23

A conservative set of parameters which we have investigated is:

g/ℓ	=	0.5
ω_{slot}	=	980 Mc (scaled from 840)
W_π	=	805 Mc/sec (scaled from 690)
k_{eff}	=	0.1042
L_{nose}/R	=	0.505
Hole size	=	1.25"
ZT^2	=	17 MΩ/m at β = 0.30 29 MΩ/m at β = 0.61 32 MΩ/m at β = 0.81

Figure 20 shows these data points plotted vs energy.

Higher values of shunt impedance could be obtained for various changes in the parameters above. It appears that decreasing g/ℓ will increase ZT^2 even more. Peak fields will set the limit for this change, and since no sparking measurements have yet been made, we do not feel justified in pushing this parameter. From dielectric bead measurements, we calculate peak fields on the drift tube surfaces of about 5 MV/m for 1 MV/m acceleration rate in the g/ℓ = 0.5 cavity at β = 0.6. This is certainly conservative. Flattening the ends of the noses will add a few per cent to the shunt impedance, but it is not felt worthwhile at this time.

21-Cell Prototype Model

Using approximately the above parameters, (β = 0.68), a 21-cell cavity has been constructed using the bent sheet metal technique with brazed joints. Figure 21 shows this model set up in our laboratory. The dispersion curve for this model is shown in Fig. 22. This was taken after the tank was flattened to about 1% in E. All points on this curve fit the calculated curve to better than 300 kc, the average error being about 75 kc. Figure 23 shows this dispersion curve with both passbands indicated. Analysis of these data gives an effective coupling k = 0.94, ω_1 = 803, and ω_2 = 934 Mc/sec.

The power flow phase shift has been measured in this model with the tank driven at one end (equivalent to a 40-cell tank driven in the middle). Figure 24 shows the measured values of phase shift along with the theoretical value given by

$$\Delta\phi_{n,o} = \frac{1 - k_{eff}}{k_{eff}\, Q} \quad n^2$$

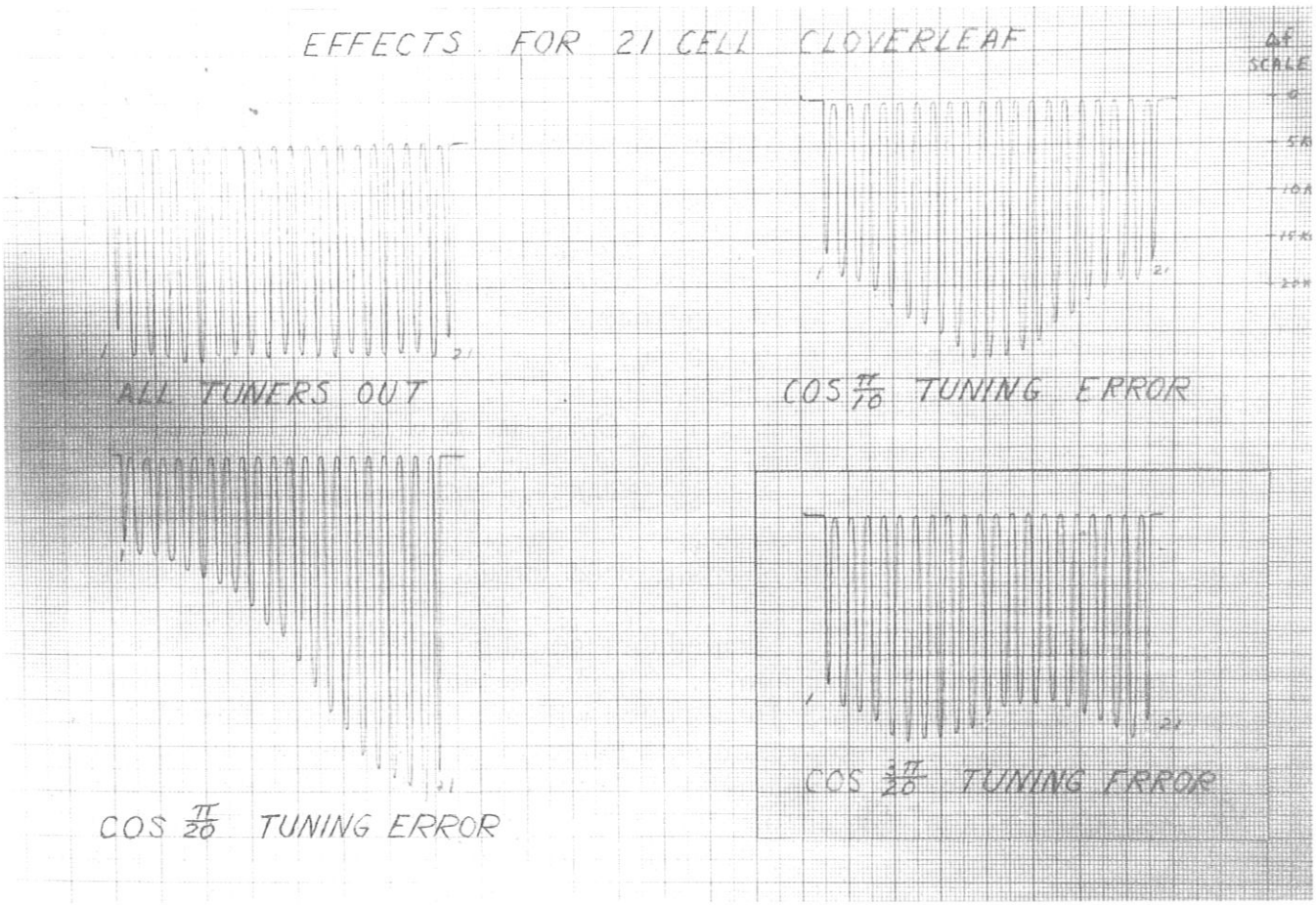
EFFECTS FOR 21 CELL CLOVERLEAF
ΔE SCALE
ALL TUNERS OUT
COS π/20 TUNING ERROR
COS π/10 TUNING ERROR
COS 3π/20 TUNING ERROR

FIG. 25

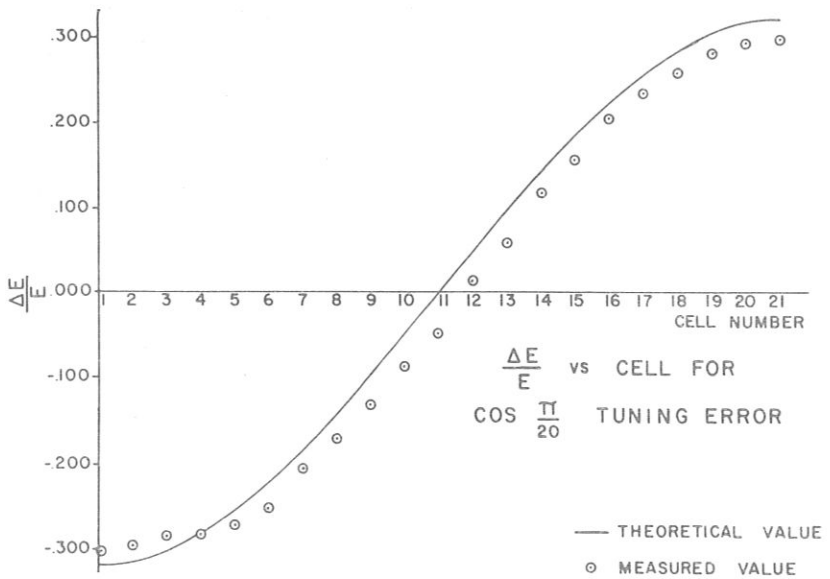
.300
.200
.100
.000
-.100
-.200
-.300
ΔE/E
1 2 3 4 5 6 7 8 9 10 11 12 13 14 15 16 17 18 19 20 21
CELL NUMBER
ΔE/E vs CELL FOR
COS π/20 TUNING ERROR
THEORETICAL VALUE
MEASURED VALUE

FIG. 26

where n is the number of cells downstream (away from the power source) from the cell in question.

The agreement between our theoretical expressions and the model measurements seems quite good.

For a π mode structure with effective coupling k we have the perturbation expression

$$\frac{\delta I_n^N}{I_n^N} = \frac{1}{k_{eff}} \sum_{r=1}^{N} \tilde{\epsilon}_r \frac{\cos \frac{\pi r n}{N}}{1 - \cos \frac{\pi r}{N}} .$$

If we introduce a tuning error $\frac{\delta \omega_n}{\omega_o} = a \cos \frac{\pi n p}{N}$ into our tank, we may check the predictions of the perturbation theory with the observed changes in field level in the tank. We have done this for p = 1, 2, and 3. Figure 25 shows the data for these measurements. A bead was pulled along the cavity axis at a constant rate, and the resonant frequency of the cavity scaled on a fast scaler. Frequency differences were recorded using a digital-to-analog converter; they were plotted directly by a x-y plotter, providing the records shown in the figure. The amplitude error induced may then be compared to the predictions of the perturbation theory. Figures 26, 27 and 28 show the comparison between the theoretical curves and the experimental points measured. Agreement seems quite good. From experience gained in flattening this prototype it appears that wall deformation will be adequate for tuning; no tuners should be required. Shunt impedance measurements indicate the same values quoted above for the shorter models.

Resonant Coupled Structures

Dunn, Sable and Thompson at Harwell were perhaps the first to point out some of the advantages of operating a structure with resonant coupling. The equivalent circuit theory used here allows even more advantages to be seen in the use of structures of this type. A resonant coupled π mode structure may be considered as a $\pi/2$ mode structure with cells of type 1 and 2 operating at the same resonant frequencies. Some properties of $\pi/2$ mode operation are

1. Every other cell (in this case the resonant coupling element) has no stored energy associated with it other than that required to transmit power to make up losses. This can be seen directly from the eigenfunctions of the chain

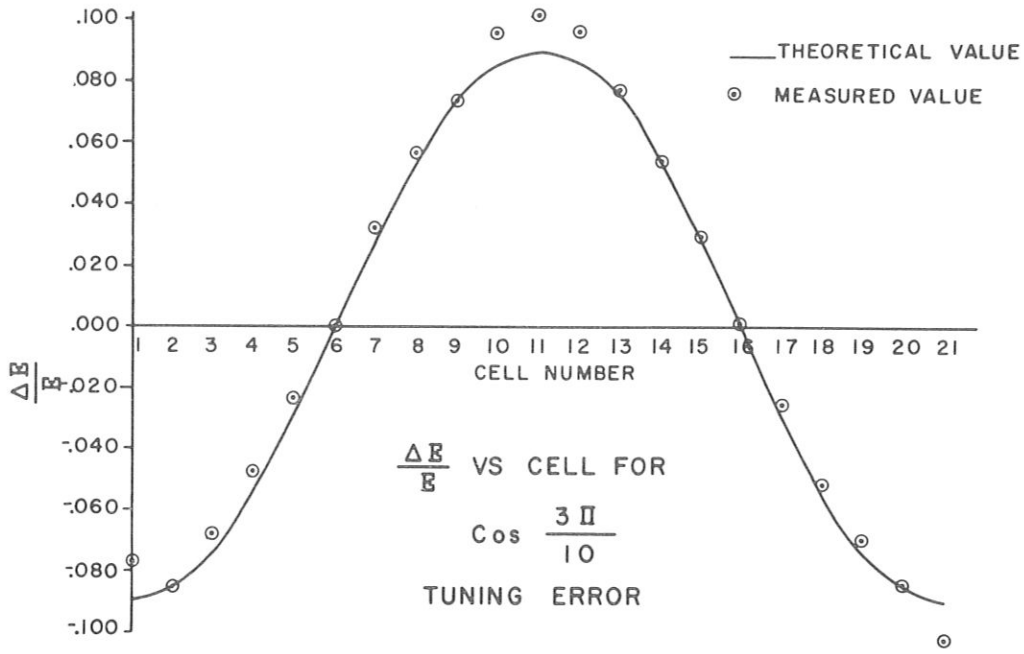
.100
.080
.060
.040
.020
.000
-.020
-.040
-.060
-.080
-.100
ΔE/E
1 2 3 4 5 6 7 8 9 10 11 12 13 14 15 16 17 18 19 20 21
CELL NUMBER
THEORETICAL VALUE
MEASURED VALUE
ΔE/E VS CELL FOR
Cos 3Π/10
TUNING ERROR

FIG. 27

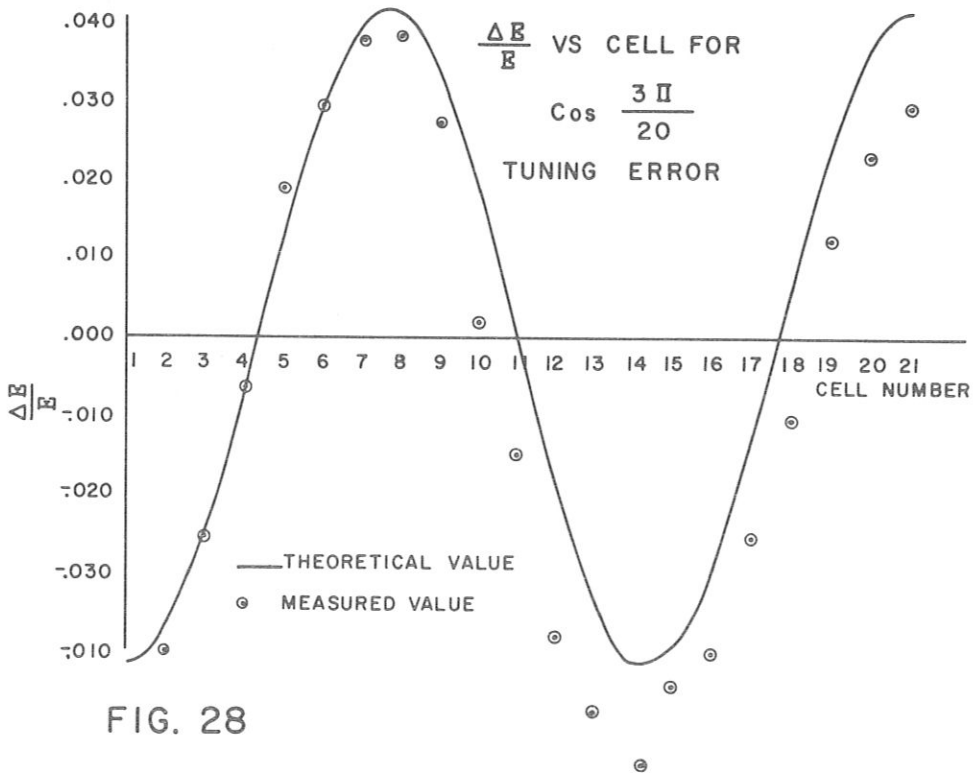
.040
.030
.020
.010
.000
-.010
-.020
-.030
-.010
ΔE/E
1 2 3 4 5 6 7 8 9 10 11 12 13 14 15 16 17 18 19 20 21
CELL NUMBER
ΔE/E VS CELL FOR
Cos 3Π/20
TUNING ERROR
THEORETICAL VALUE
MEASURED VALUE

FIG. 28

$$i_n^{N/2} = \cos \frac{\pi}{2} n .$$

Thus one should not have to worry about sparking in coupling elements, losses in coupling elements, etc.

2. The phase of all accelerating cells is locked at π, any variations occurring only through second-order effects in frequency errors. This may be seen by considering the circuit equation

$$X_{n+2} = -X_n + \frac{2}{k} \left(- \frac{2 \Delta\omega_{n+1}}{\omega} + \frac{i \omega_n}{\omega Q} \right) X_{n+1} ; \qquad (12)$$

if cell n + 1 is a coupling cell, its amplitude is small (point 1) and imaginary (for power flow). The phase shift is then the product of two numbers which are small, $\frac{\Delta\omega_n}{\omega}$ and X_{n+1}. For no errors, we see no phase shift.

3. The amplitude of the fields in the accelerating cells is independent of frequency errors in any cells in first-order theory. Second-order effects do occur but only for very large amplitude errors. This may also be seen from Eq. (12), amplitude variations being the quotient X_{n+1}/Qk which is very small indeed. If X_{n+1} has a real component (due to other frequency errors in accelerating cells), then some amplitude variation may take place due to coupling cell mistunings, but the sensitivity is very low.

4. From Eq. (12), if X_{n+2}, X_n are coupling cell amplitudes and X_{n+1} an accelerating cell amplitude, we see that as $\Delta\omega_{n+1}$ goes through zero we should see a minimum in the coupling cell field X_n. This provides an exceedingly easy way to tune a structure of this type, for now one can choose a frequency, and successfully tune coupling cell fields to minima by changing accelerating cell tuners, working from a point furthest from the drive point toward the drive. It can thus be tuned, one cell at a time, to any predetermined frequency.

5. Since operation is now at the center of the passband where the slope is steepest, mode separation is maximum, and considerably narrower bandwidth may be tolerated for satisfactory performance.

6. This allows us to separate the shunt impedance problem from the coupling problem to some extent and may allow better shunt impedance optimizations.

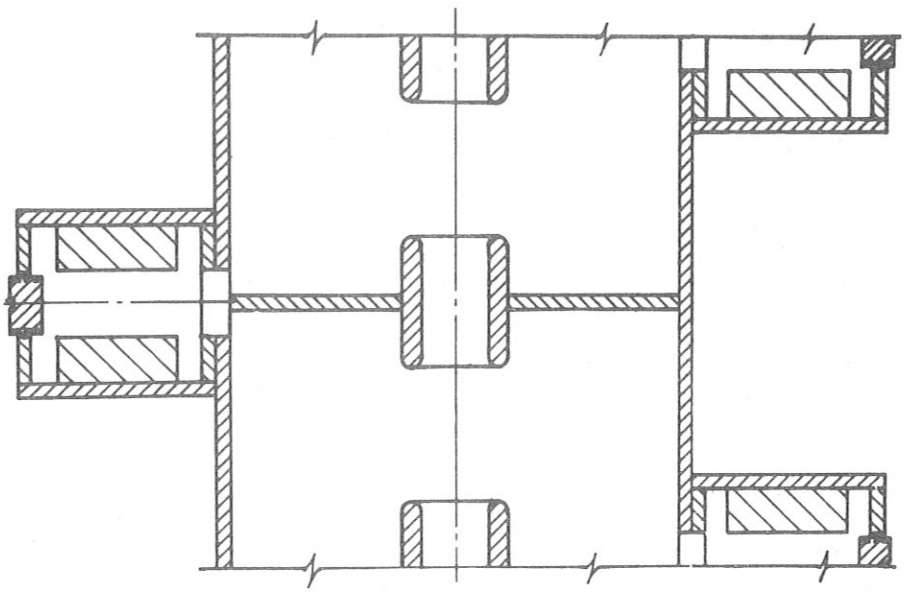

FIG. 29

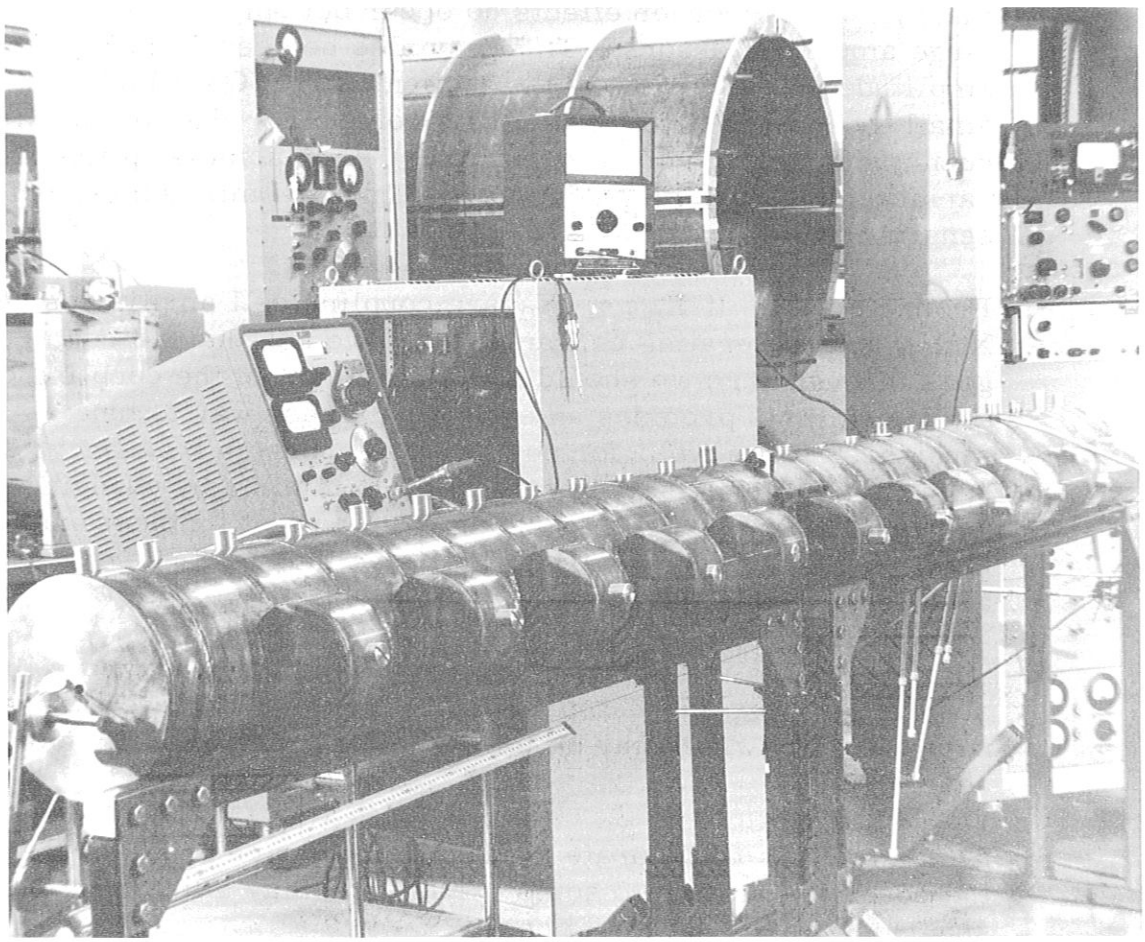

FIG. 30

We have built two models with resonant coupling devices and quite narrow bandwidths to investigate these properties. Figure 29 shows two accelerating cavities coupled by a side cavity which is resonant at the same frequency as the accelerating cavities. A slot cut in the mutual side walls of the cavities provides energy transfer from accelerating cell to coupling cell, etc. Since the coupling cell stores no energy in $\pi/2$ mode, its Q does not contribute to the shunt impedance values obtained, and thus this cavity may be made without too much regard to the Q obtained. We thus may heavily load the side cavity to make it small without affecting the shunt impedance appreciably. Since the slot which couples energy may be made quite small, one is free to modify the accelerating cavity at will in order to increase its shunt impedance. We have not tried to do this as yet. Figure 30 shows a photograph of a 24-cell model of a structure of this type. Shorter models have also been constructed of this configuration. After tuning up by the method described in point 4 above, a very reasonable dispersion curve is obtained near the $\pi/2$ mode with 1" x 2" slots. The structure shows a 20 Mc bandwidth at 810 Mc with 500 kc mode separation on either side of the $\pi/2$ mode. Near the zero and π modes, the Q curves overlap so badly no data are available.

In the limited time available before this meeting, we have seen no deviations from the predictions of the theory. When just tuned up, the tank was flat to $\sim \pm$ 5% in E, and we have not been able to change this with any reasonable tuning arrangement. Since construction of this tank was quite crude, we might expect geometrical errors to account for this. Measurement of field levels in coupling cells indicates negligible energy stored in them. No phase shift can be detected between one end and the other of the model. Detailed measurements and comparison with theory are under way and should be completed shortly. Shunt impedance values of 30 MΩ/m at $\beta = 0.7$ have been obtained with the models.

In closing I would like to note that the cloverleaf can also be run resonantly coupled. No field should develop in the slot for, as we have noted, alternate cells store no energy in the $\pi/2$ mode operation. This would make a structure which should be extremely stable.

Development work is continuing on these structures. We also hope to check sparking levels in a short cloverleaf cavity with 100 kw of pulsed rf at 805 Mc/sec soon.

CARNE: What was the Q of your 21-cell model?

KNAPP: The Q is about 16, 500.

CHARACTERISTICS OF SLOTTED IRISES

S. Giordano
Brookhaven National Laboratory

Some preliminary measurements of slotted iris structures are reported in the minutes of the Conference on Proton Linear Accelerators at Yale University, October 21-25, 1963, p. 153.

Although the above measurements were made with sheet metal irises, the results were sufficiently encouraging to warrant further investigation.

Before embarking on a full-scale modeling program, it was decided that some additional measurements would be useful. The purpose of these measurements was, first, to measure such parameters as shunt impedance, bandwidth, etc., and, second, to gain some experience in setting up a full-scale modeling program.

The measurements to be discussed in this paper were made on a limited number of available cavities. With the limited amount of data available, some interpolation and extrapolation of the data was necessary.

A slotted iris model was constructed as shown in Fig. 1. Measurements were made with two different bore hole diameters of D = 1.625" and D = 2.1", four different drift tube lengths of ℓ = 1.0", ℓ = 1.5", ℓ = 2.0" and ℓ = 2.5", and two different cell lengths of L = 4.0" and L = 6.0". All measurements were made in the "π" mode.

Figures 2 and 3 are plots of frequency vs β for various drift tube lengths. Figures 4 and 5 are plots of shunt impedance vs β for various drift tube lengths. In all of the above plots, straight lines were used to join the measured data points. (Results generally obtained on various structures in the range of β = 0.5 to β = 0.8 show that the variation of frequency and shunt impedance do not vary appreciably from a straight line.) In Figures 2, 3, 4, and 5, we see that the actual measured points are grouped around β = 0.5 and β = 0.8, so that the conclusions, which will be drawn in the neighborhood of these values of β, should have about the same accuracy as the measured data.

From Figs. 4 and 5, by drawing lines at constant β's of 0.5, 0.6, 0.7, and 0.8, it is now possible to draw curves of shunt impedance vs drift tube length for constant β as shown on Fig. 6 for a bore hole of 1.625" and Fig. 7 for a bore hole of 2.1". In Fig. 7, the region between the drift tube lengths of 2.0" to 2.5" may be in error by as much as 10% due to the lack of data points in this region. A comparison of Figs. 6 and 7 reveals some interesting features. There is a considerable change

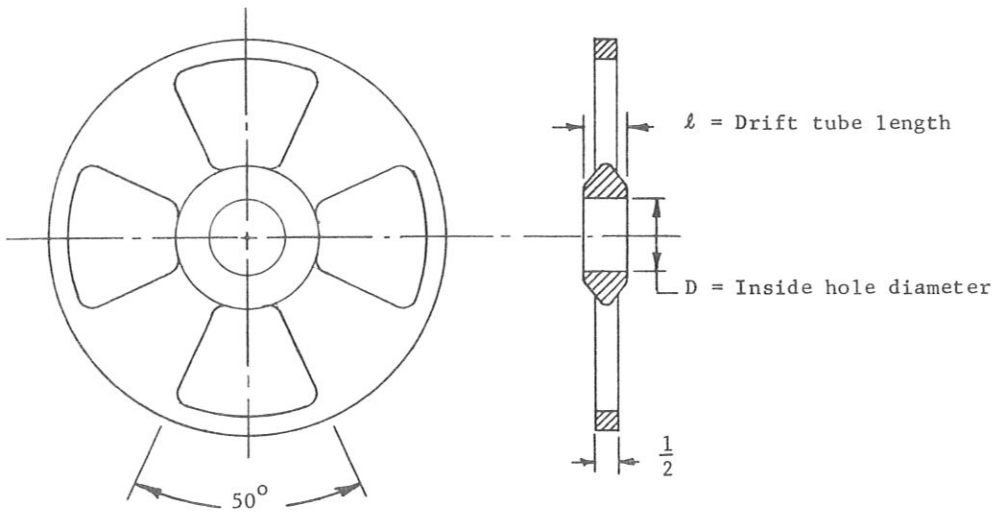

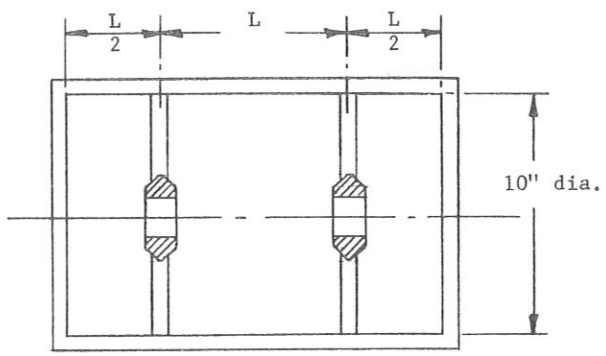

Fig. 1

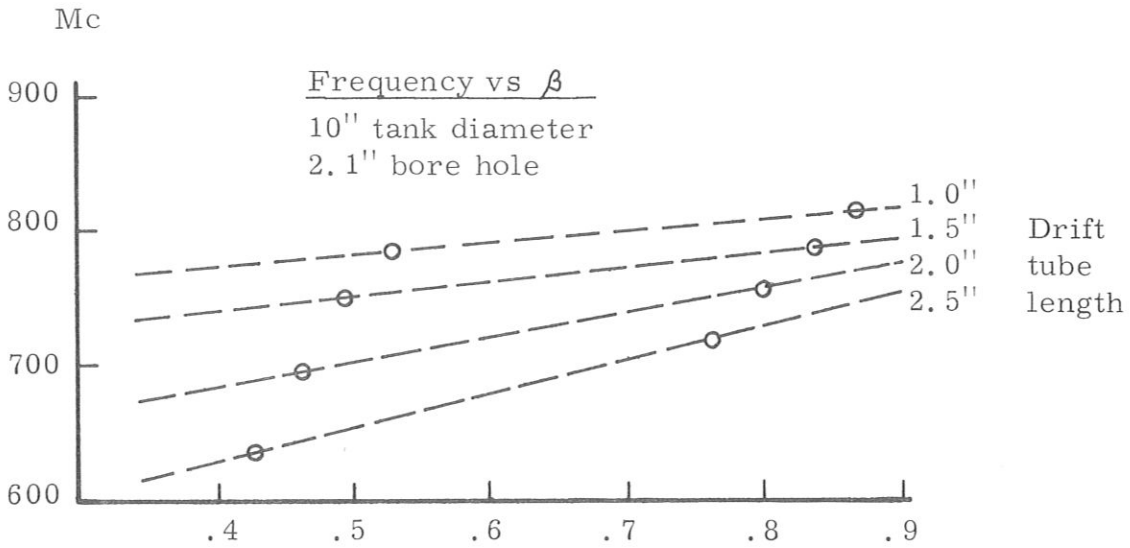
Mc
900
800
700
600
Frequency vs β
10" tank diameter
2.1" bore hole
1.0"
1.5"
2.0"
2.5"
Drift tube length
.4
.5
.6
.7
.8
.9

Fig. 2

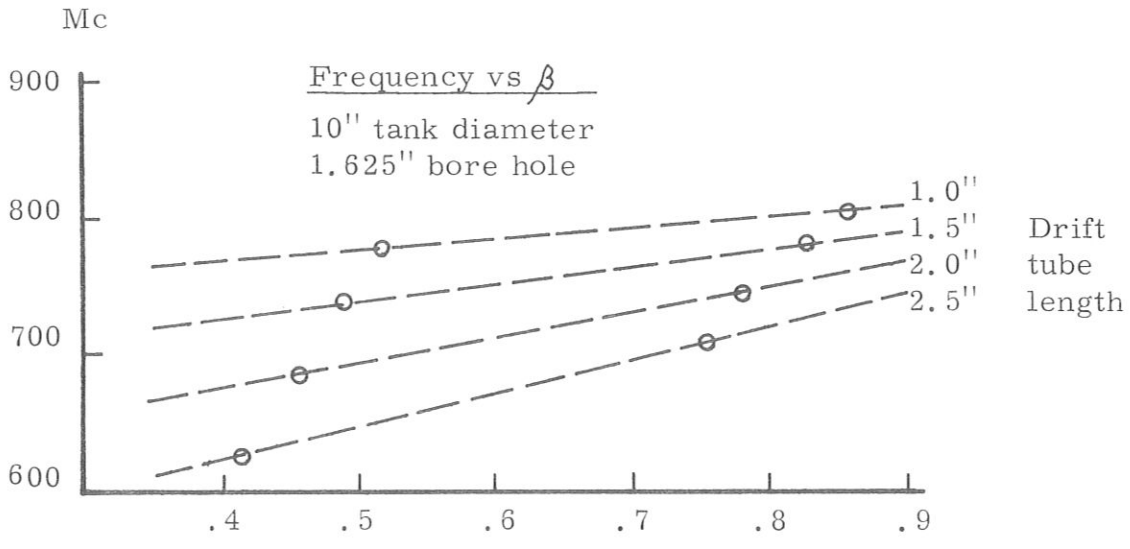
Mc
900
800
700
600
Frequency vs β
10" tank diameter
1.625" bore hole
1.0"
1.5"
2.0"
2.5"
Drift tube length
.4
.5
.6
.7
.8
.9

Fig. 3

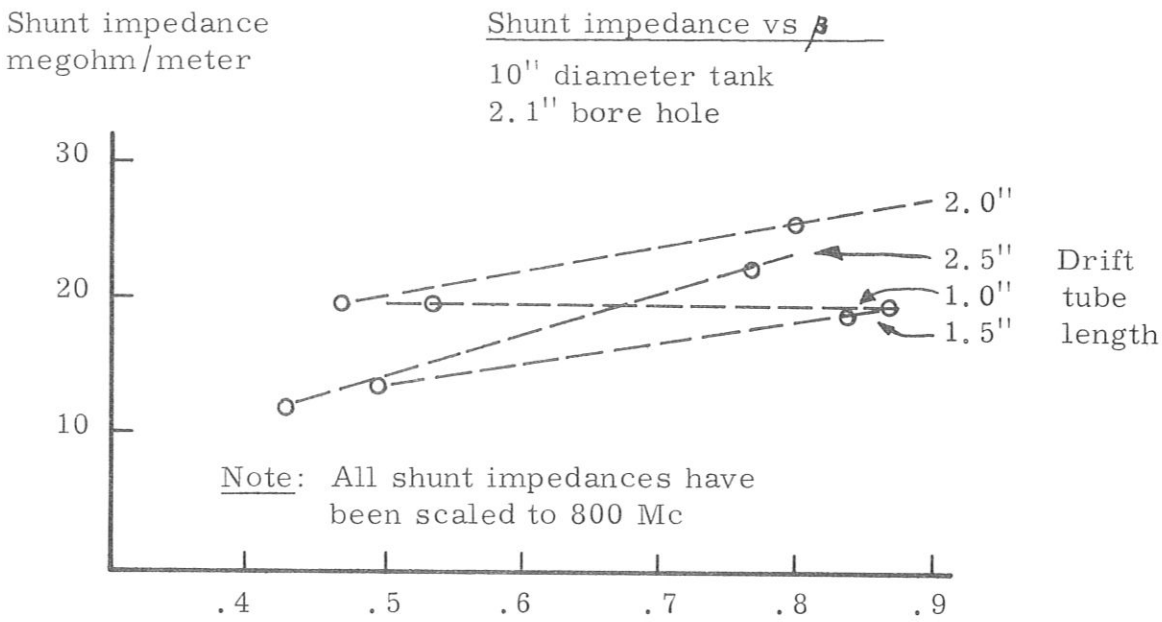
Shunt impedance
megohm/meter
Shunt impedance vs β
10" diameter tank
2.1" bore hole
30
20
10
2.0"
2.5"
1.0"
1.5"
Drift
tube
length
Note: All shunt impedances have
been scaled to 800 Mc
.4
.5
.6
.7
.8
.9

Fig. 4

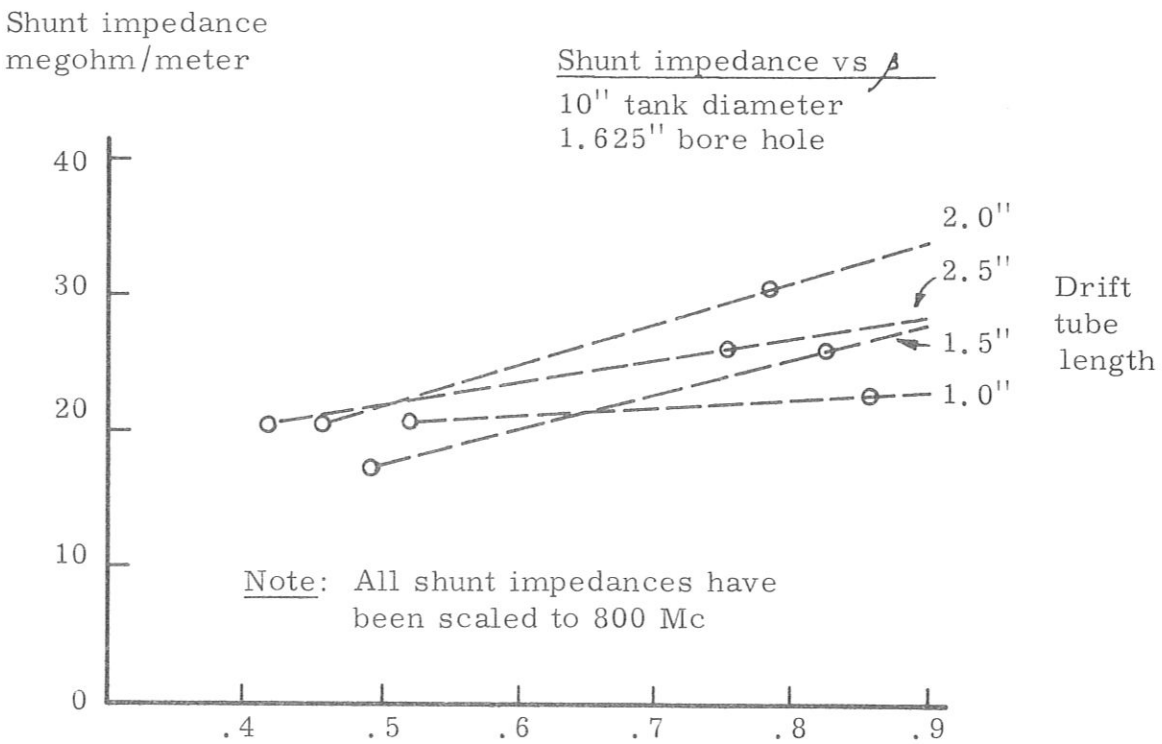
Shunt impedance
megohm/meter
Shunt impedance vs β
10" tank diameter
1.625" bore hole
40
30
20
10
0
2.0"
2.5"
1.5"
1.0"
Drift
tube
length
Note: All shunt impedances have
been scaled to 800 Mc
.4
.5
.6
.7
.8
.9

Fig. 5

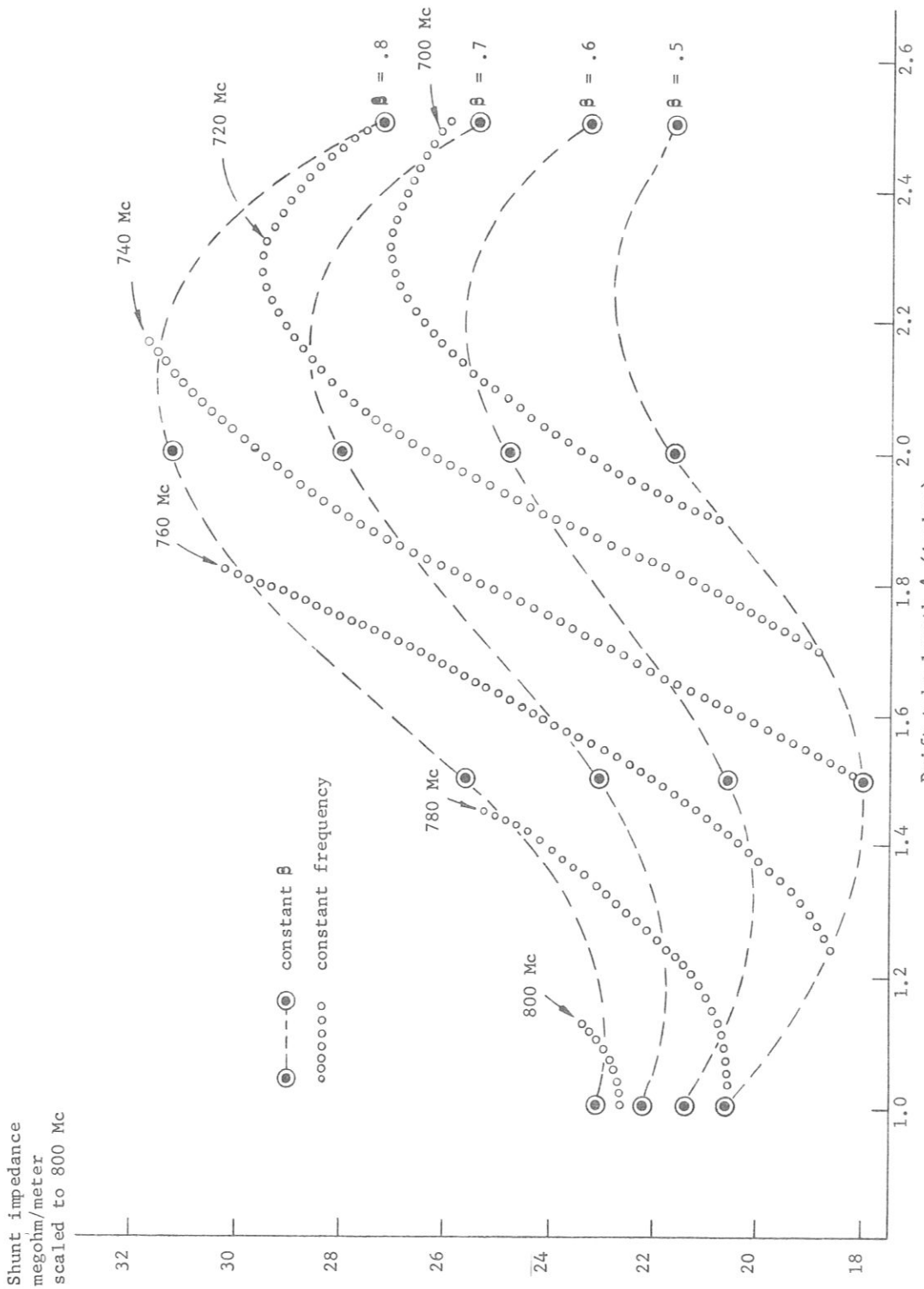

Fig. 6 Shunt impedance vs drift tube length for 50° slotted iris (1.625" bore hole)
(curves of constant frequency and β)

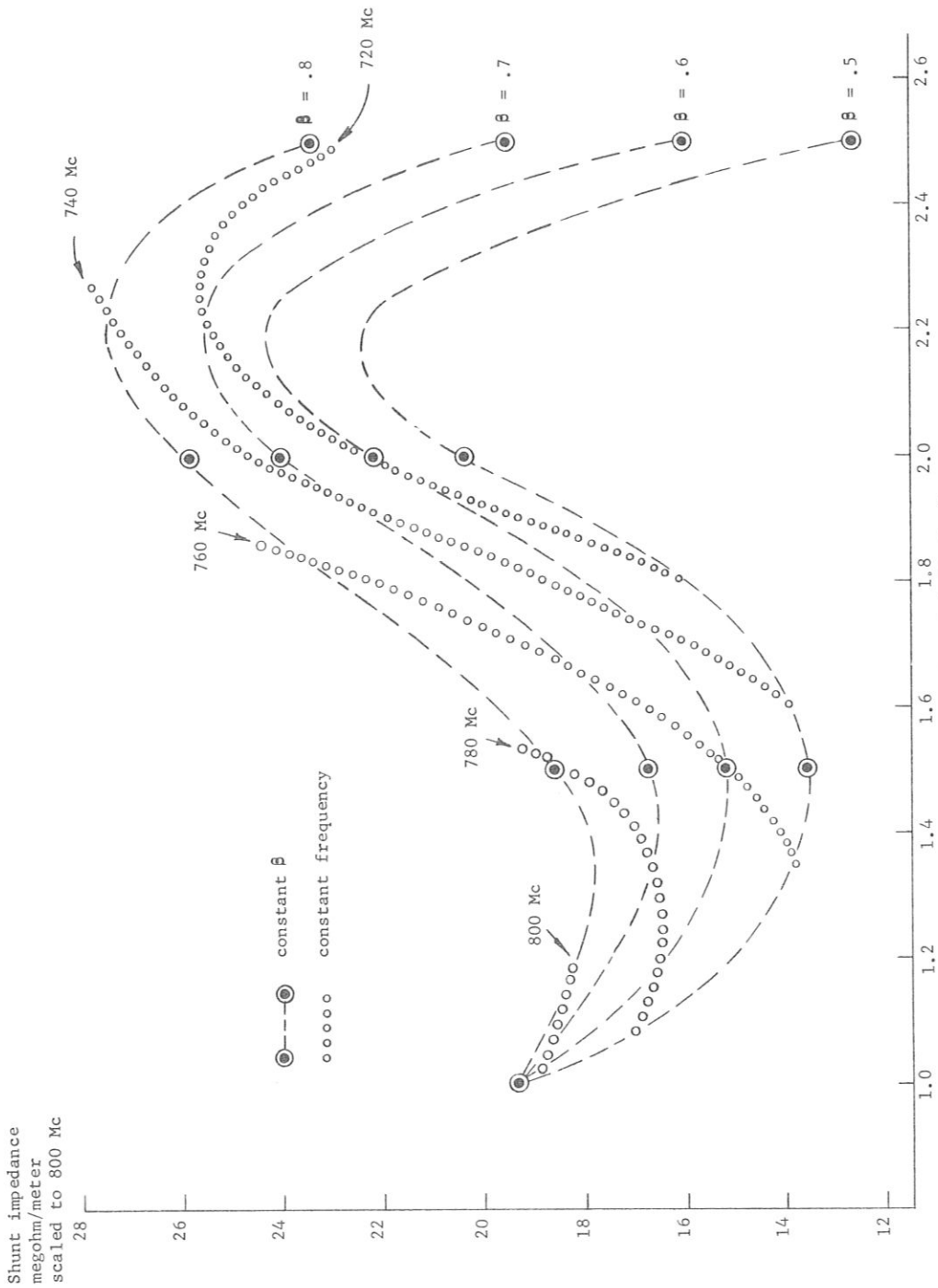

Fig. 7 Shunt impedance vs drift tube length for 50° slotted iris (2.1" bore hole)
(curves of constant frequency and β)

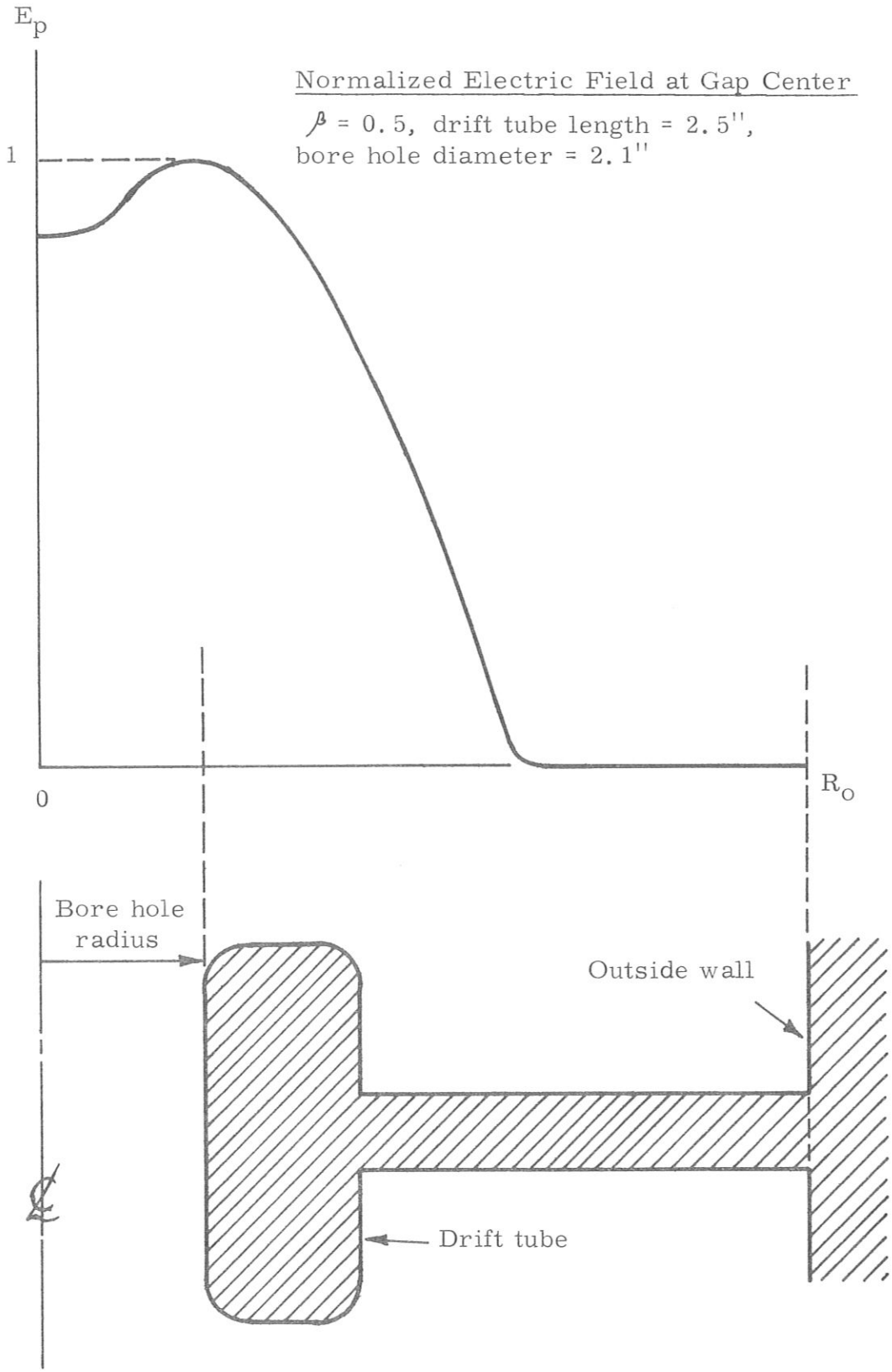
E_p
Normalized Electric Field at Gap Center
β = 0.5, drift tube length = 2.5",
bore hole diameter = 2.1"
1
0
R_o
Bore hole radius
Outside wall
Drift tube

Fig. 8

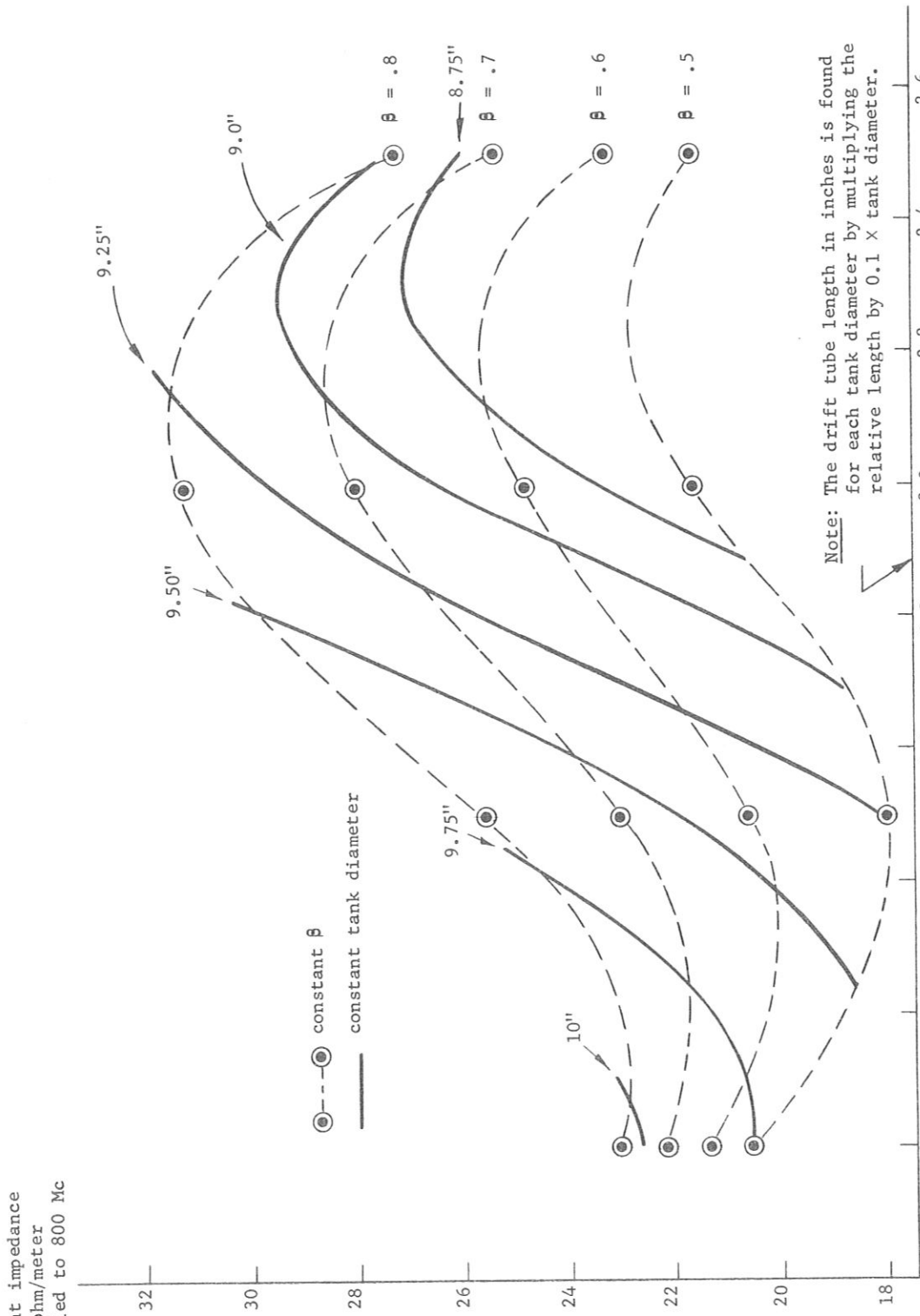

Fig. 9 Shunt impedance vs. drift tube length for 50° slotted iris (bore hole corresponding to 10" tank is 1.625") (curves of constant tank diameter and constant β) at 800 Mc

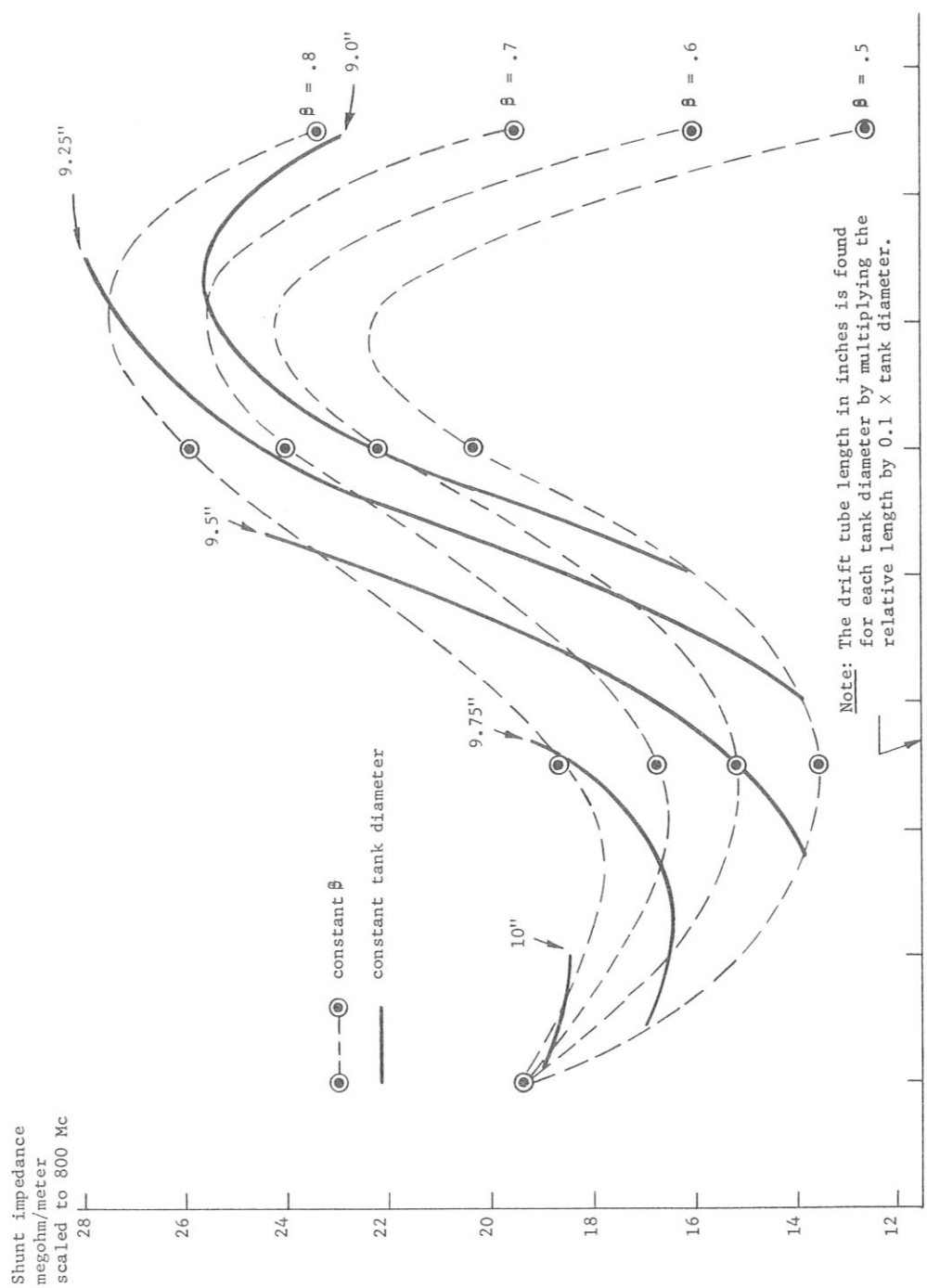

Fig. 10 Shunt impedance vs. drift tube length for 50° slotted iris (bore hole corresponding to 10" tank is 2.1") (curves of constant tank diameter and constant β) at 800 Mc

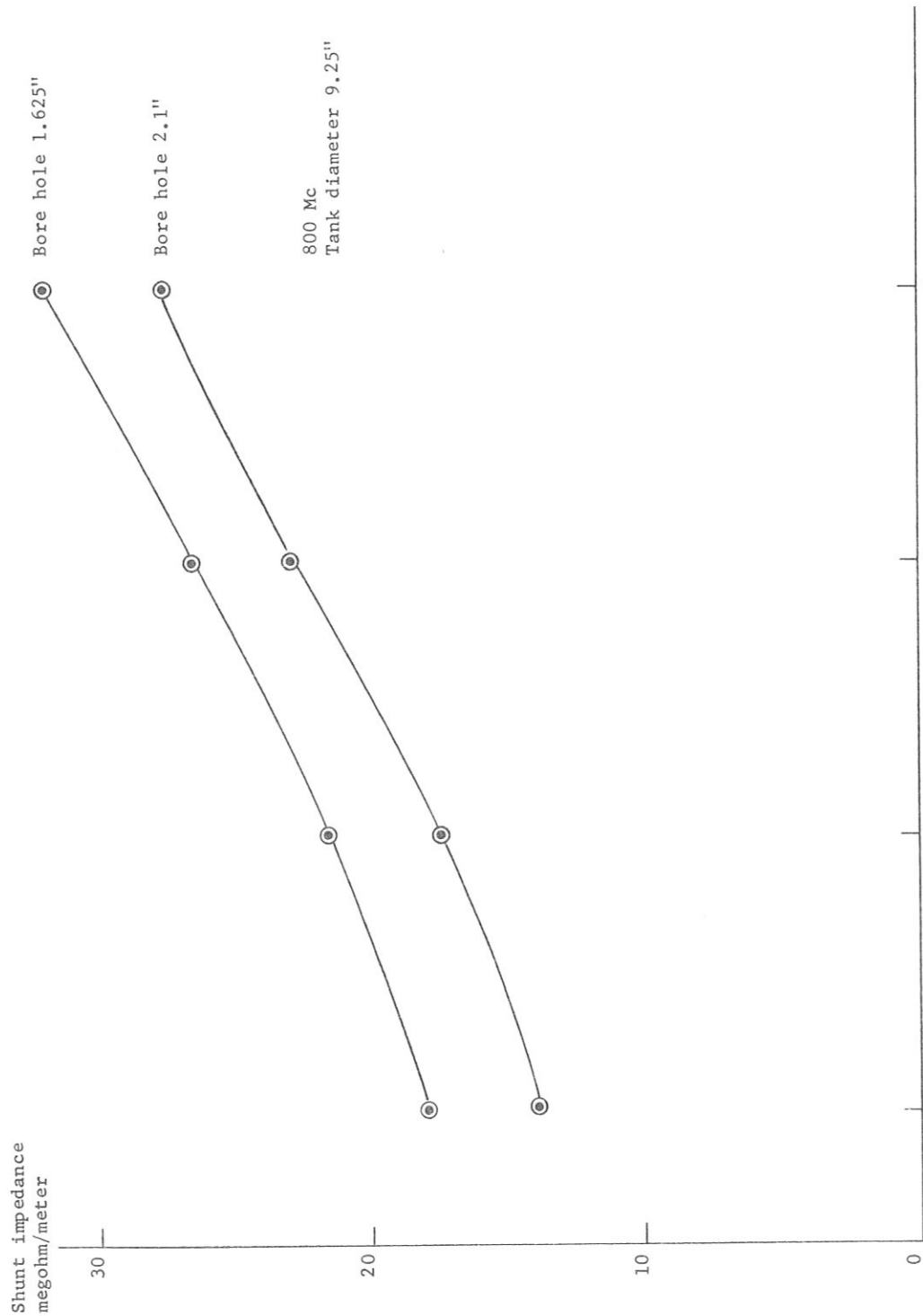

Fig. 11 Shunt impedance vs β for 50° slotted iris

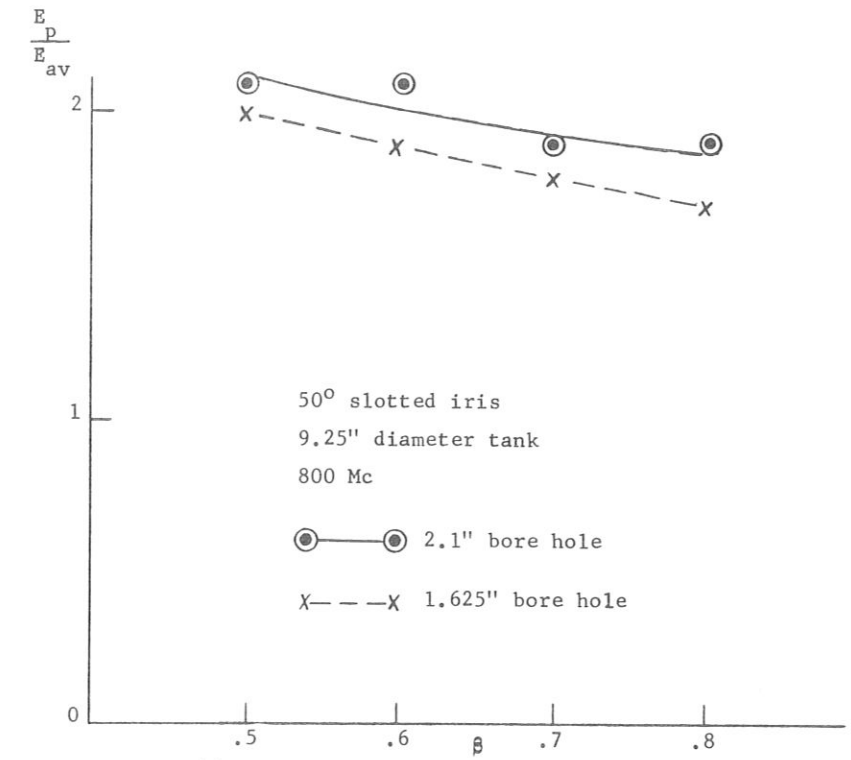

Fig. 12 Ratio of peak field to average field vs β for the 50° slotted iris

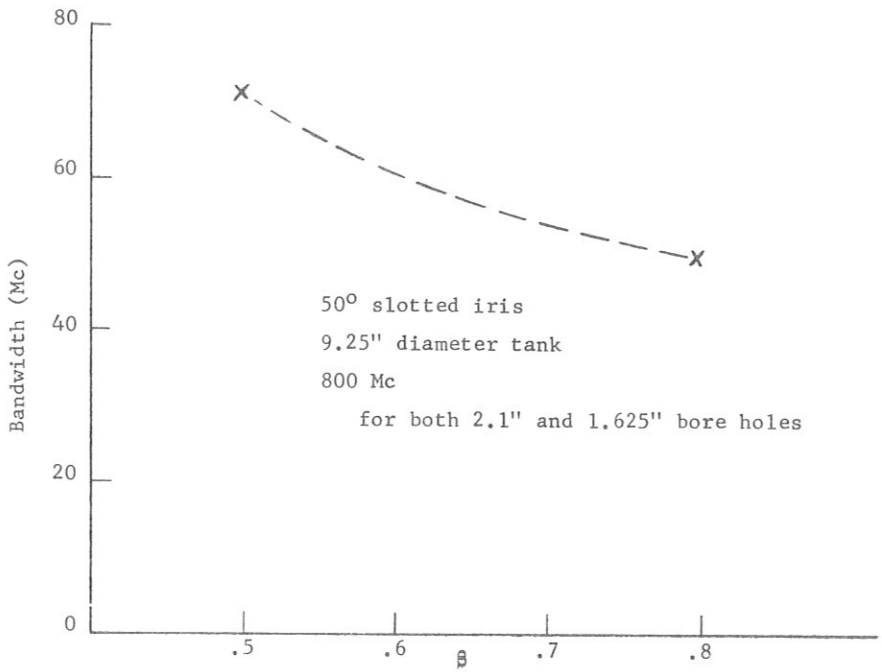

Fig. 13 Bandwidth vs β for the 50° slotted iris

in shunt impedance between the 1.625" bore hole and the 2.1" bore hole. Another interesting point is the rapid fall-off of shunt impedance with longer drift tubes. At β = 0.5 and a drift tube length of 2.5", we see that, with increasing drift tube length, fall-off of shunt impedance for the 1.625" bore hole is small as compared to the 2.1" bore hole. One reason for fall of shunt impedance can be seen in Fig. 8, which is a radial plot of the electric field at the center of a cell and shows a dip of 11% in the electric field on the axis for the larger bore hole.

From Figs. 2 and 3, by drawing lines of constant frequency at 800 Mc, 780 Mc, 760 Mc, 720 Mc, and 700 Mc, and by interpolating between the various drift tube lengths at β's of 0.5, 0.6, 0.7, and 0.8, we may sketch in the contours of constant frequency in Figs. 6 and 7. The data in Figs. 6 and 7 were made on a 10" diameter tank. It is interesting to note that the constant frequency contours in Figs. 6 and 7 can be made to represent constant tank diameters at some other frequency. If, for example, we select 800 Mc/sec as an operating frequency, and if we scale the dimensions of the original 10" diameter tank (used for the measurements in Figs. 6 and 7) by $\frac{780}{800}$, we get a tank whose diameter is 9.75", and the constant frequency contours of 780 Mc in Figs. 6 and 7 become constant tank diameter contours of 9.75" at an operating frequency of 800 Mc. We may now draw Figs. 9 and 10, noting that the drift tube length is scaled proportionately.

If an operating frequency of 800 Mc is selected, we see that a tank diameter of 9.25" would be a good choice. If one is willing to change tank diameters, some over-all improvement in the average shunt impedance can be gained. Figure 11 shows the shunt impedance as a function of β for a 9.25" diameter tank at 800 Mc. There may be as much as a $\pm$ 15% error in shunt impedance due to the original measurements of "$\overline{Q}$".

It can be shown that

$$\frac{E_p}{E_{av}} = \frac{1}{f} \sqrt{\left(\frac{L\,N}{2\,\pi^2\,\epsilon_o\,r_o^3} \right) \times \left(\frac{Q\,\Delta f}{R_s} \right)} ,$$

where E_p is the peak electric field at the center of a cavity, E_{av} is the average electric field as seen by a synchronous particle, f is the operating frequency, L is the length of the cavity in meters, r_o is the radius in meters of a small metal sphere placed at the center of the cavity, Δf is the frequency perturbation due to the metal sphere placed at the center of the cavity, and N is the number of cells. Figure 12 is a plot of

E_p/E_{av} scaled to a 9.25" diameter tank. Figure 13 is a plot of bandwidth vs β at 800 Mc/sec.

From the results of the above measurements, a new series of test cavities is being built, having a tank diameter of 9.25". Measurements will be made on four sets of irises with slots, subtending angles of 35°, 40°, 45°, and 50°, as shown in Fig. 1.

JOHNSTON: Was this a zero-mode structure?

GIORDANO: No, all these measurements were made in the π mode. It should be pointed out that the shaped iris cavity is a forward wave structure, and the slotted iris cavity is a backward wave structure.

CARNE: You gave us shunt impedance measurements at 800 Mc. What were the η/Q and the Q values?

GIORDANO: The Q values, as I recall, were around 14,000 at $\beta \cong 0.5$ and about 16,000 at $\beta \cong 0.9$.

NAGLE: What were the actual measurement frequencies? As I recall, they were about 700 Mc?

GIORDANO: For these particular measurements, the tank diameter was kept constant, and the only thing I varied was the drift tube length. The measured data points ran from about 625 Mc up to about 825 Mc.

NAGLE: Over what frequencies were the extrapolations made?

GIORDANO: In extrapolating from a 10-inch diameter tank to a 9-1/4 inch diameter tank, my actual frequency extrapolation was from 740 Mc to 800 Mc.

NAGLE: Were these models constructed with spring-ring contacts?

GIORDANO: Yes.

HUBBARD: I wanted to say that at Berkeley we have made some preliminary measurements on an 800 Mc slotted iris structure similar to one described by Giordano. I will put the numbers on the board:

β	R_{sh}
0.38	27 M Ω/meter
0.77	39 M Ω/meter

These values of R_{sh} are based on measured values of Q.

NAGLE: Does that have a transit time factor in it?

HUBBARD: Yes, I would also like to point out that our measured Q's are almost the same as yours. We did a fair amount of optimizing of the slot shape, but very little optimizing of the drift tubes.

GIORDANO: What was the bore hole size?

HUBBARD: That was for a 1.5-inch diameter hole.

GIORDANO: There should be very little difference in comparing the shunt impedance for your 1.5-inch diameter bore hole and my 1.625-inch diameter bore hole. I selected 50^{o} slots and optimized the shunt impedance by varying the drift tube lengths. You (Hubbard) selected a fixed drift tube length and varied the slot angle to optimize the shunt impedance. Both our results are in good agreement.

LOEW: Do you know what happens if you alternate the angles of the slots of the cavities, like the colverleaf?

GIORDANO: Very little. Actually for the particular model I have, which is terminated in half cells, the irises have to be alternated in pairs with the exception of the first and last iris. This is necessary to match the boundary conditions at the ends. I was hoping to change the shape of the dispersion curve, but found there was very little change.

LOEW: It remains backward?

GIORDANO: Yes.

HAGERMAN: Did you ever look for any azimuthal asymmetries in this? Since you seem to be taking the energy density stored on the axis by varying the slot width, you might wonder whether these things are azimuthally symmetric.

GIORDANO: Perturbation measurements of the azimuthal field were made. These measurements were made at $\beta \approx 0.5$, slot angles of 35^{o} and 50^{o}, with a drift tube length of one inch. The field was measured at the center of a cell at a radius approximately 0.75 inch. I could not detect any appreciable azimuthal asymmetries.

LOEW: I just wanted to mention something that might be useful to some of these studies. There was a man by the name of Mike Allen who wrote

his Ph. D. thesis on something very similar for a traveling wave tube a few years ago (he was a student of Chodorow), and he has a lot of curves put into it.

LEISS: Could you please tell me roughly what is the magnitude of the transit time correction in either one of the two cases described?

HUBBARD: About 85%.

LEISS: So about 15% is in other modes?

GIORDANO: The actual measurement of shunt impedance was made by the perturbation method, and numerically integrated.

LEISS: I'm asking for reasons of beam loading.

GIORDANO: Well, you actually have to compare the shape of the field here to the average field.

FABRICATION AND MEASURING METHODS FOR DISK-LOADED WAVEGUIDES

T. Nishikawa*
Brookhaven National Laboratory

I. Introduction

During the past ten years, extensive studies on electron linacs have been carried out in Japan. About ten machines, which were constructed by the universities or by Japanese manufacturers, are working well for various purposes. The author wishes to report on the new methods developed recently in that country to fabricate disk-loaded guides and to measure their performance precisely. This work was carried out by the group of the University of Tokyo and by the staffs of the Mitsubishi Heavy Industries, Inc. and the Toshiba Electric Company.

II. New Methods for Fabricating Guides with High Accuracies

Disk-loaded guides used in electron linacs are usually made either by a brazing or an electroforming method. These two methods were also tried in Japan and led to fairly good results in obtaining accurate guides.[1] However, in the former method, one needs to tune each cell after its fabrication unless one is extremely careful during the brazing process, while the usual electroforming method is expensive because of time consuming and troublesome procedures during fabrication. A new method has now been developed which is a combination of the strong points of these two and which eliminates those difficulties.[2]

In order to achieve and to maintain high accuracy throughout the fabrication process, copper disks and cylinders are machined separately and assembled by jigs. The outer surface of the assembled body is then electroplated to form a complete structure (Fig. 1). This method is considerably simpler than the brazing or electroforming technique previously used and eliminates a number of undesirable effects such as: 1) high temperature due to brazing, which results in dimensional distortion, and 2) use of aluminum spacers and the necessity for removing them by etching. Typical values of machining errors obtained are shown in Fig. 2. It should be stated that the resonant frequency of each cell is strongly dependent on the shaping of the cross section of the disk holes since the field strength should be strongest at that point. A rough

---

*On leave from the Department of Physics, University of Tokyo.

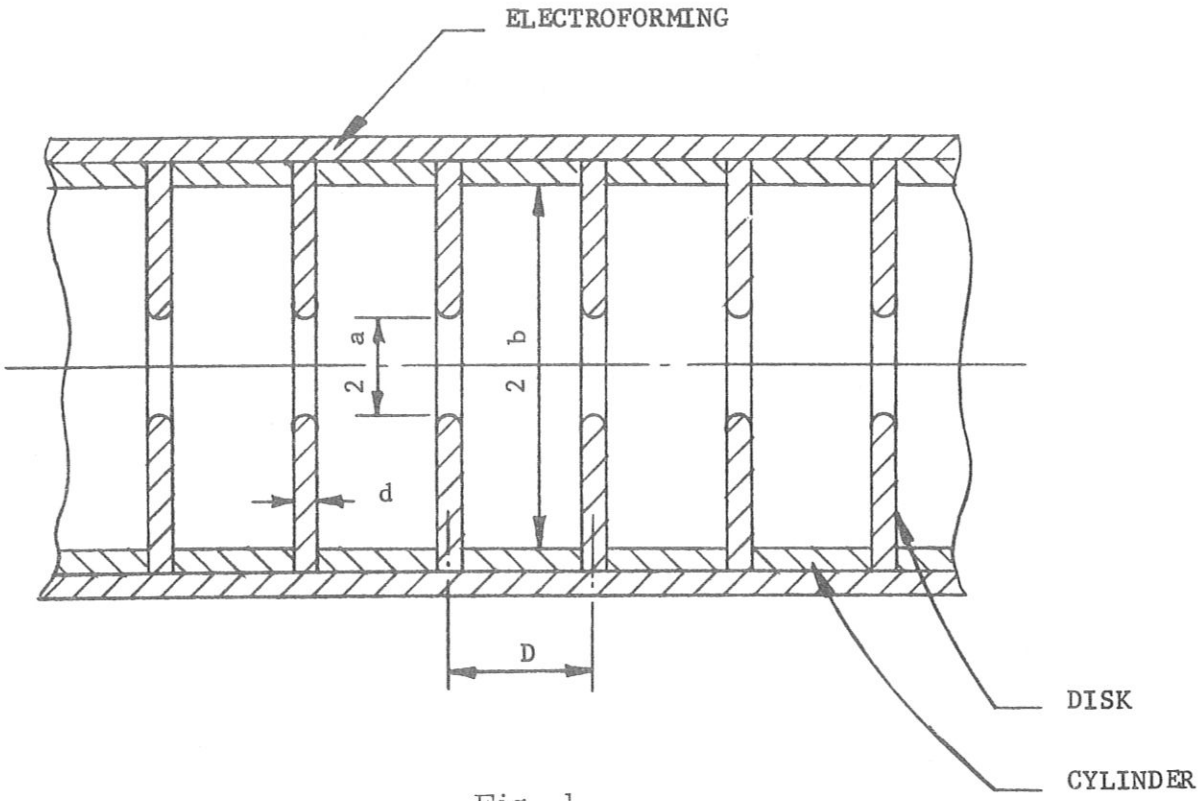

Fig. 1

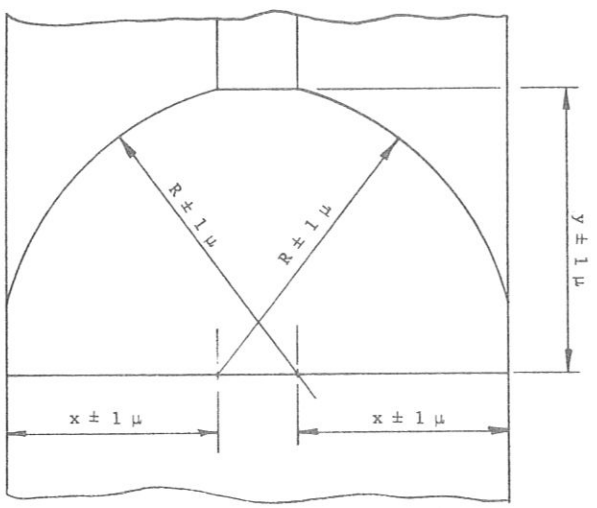

SHAPING OF DISK HOLE

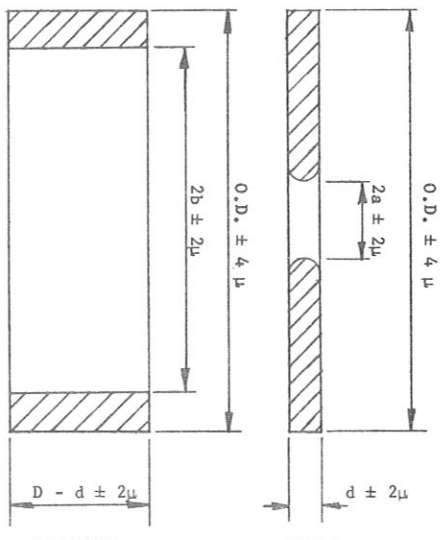

MATERIAL OFHC 99.99%

SURFACE ROUGHNESS 0.3 μ OR LESS

Fig. 2

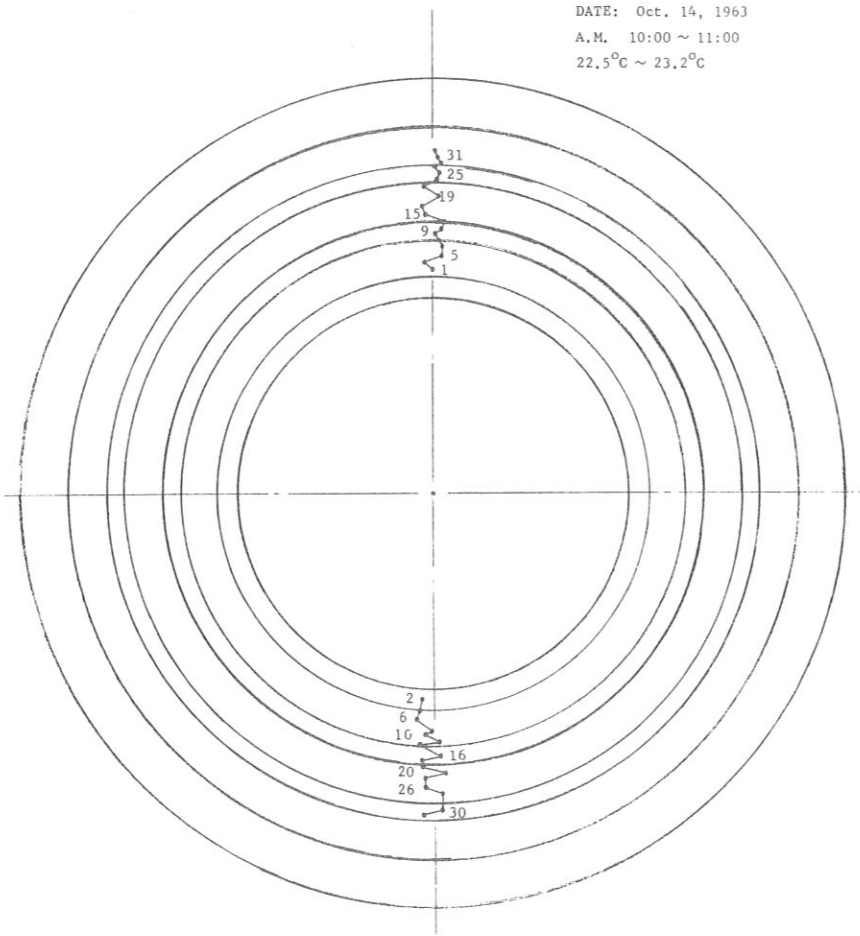
DATE: Oct. 14, 1963
A.M. 10:00 ~ 11:00
22.5°C ~ 23.2°C
31
25
19
15
9
5
1
2
6
10
16
20
26
30

Fig. 3

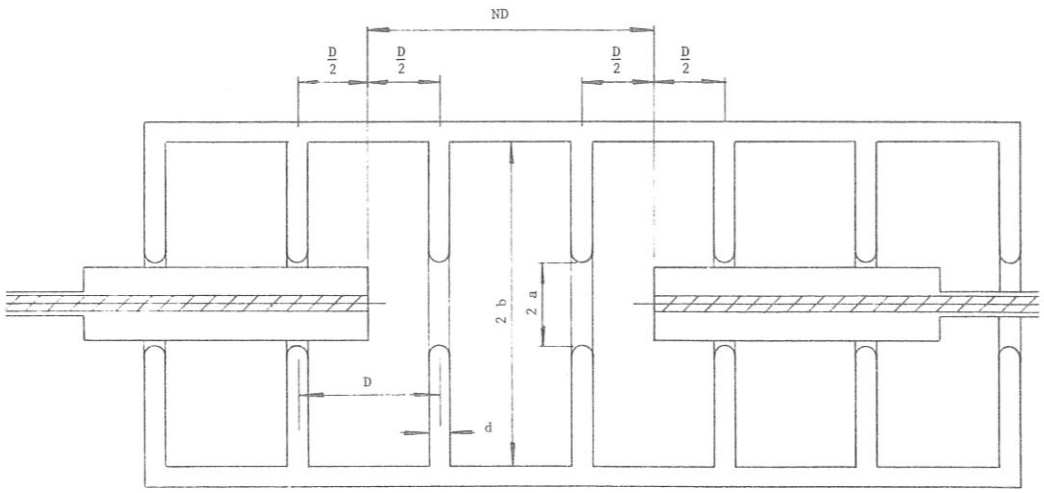
ND
D/2
D/2
D/2
D/2
2 b
2 a
D
d

Fig. 4

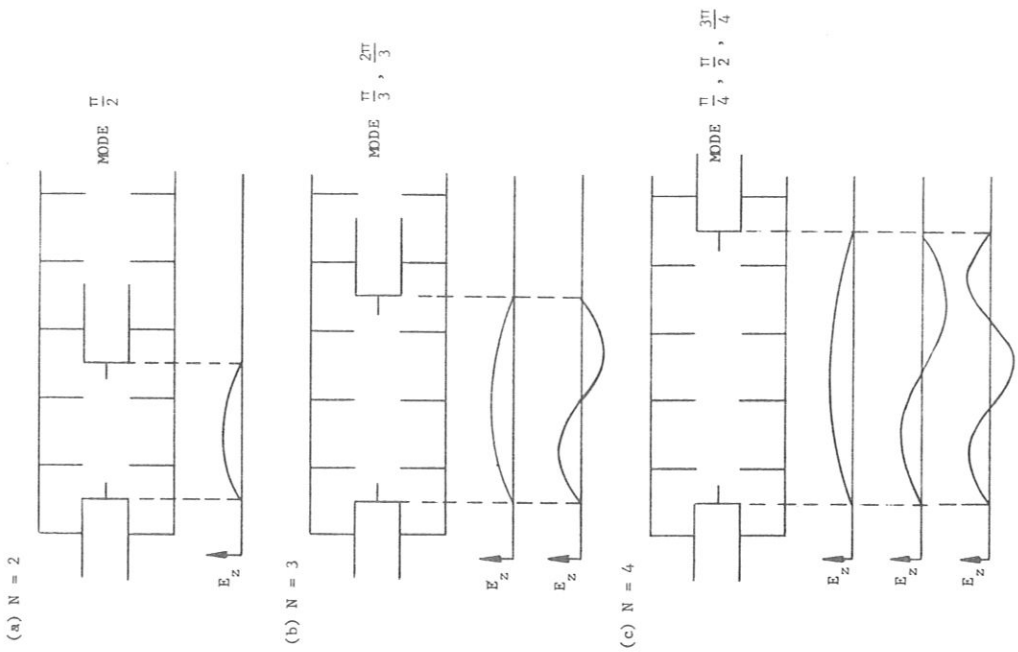
(a) N = 2
MODE $\frac{\pi}{2}$
E_z
(b) N = 3
MODE $\frac{\pi}{3}$, $\frac{2\pi}{3}$
E_z
E_z
(c) N = 4
MODE $\frac{\pi}{4}$, $\frac{\pi}{2}$, $\frac{3\pi}{4}$
E_z
E_z
E_z

Fig. 6

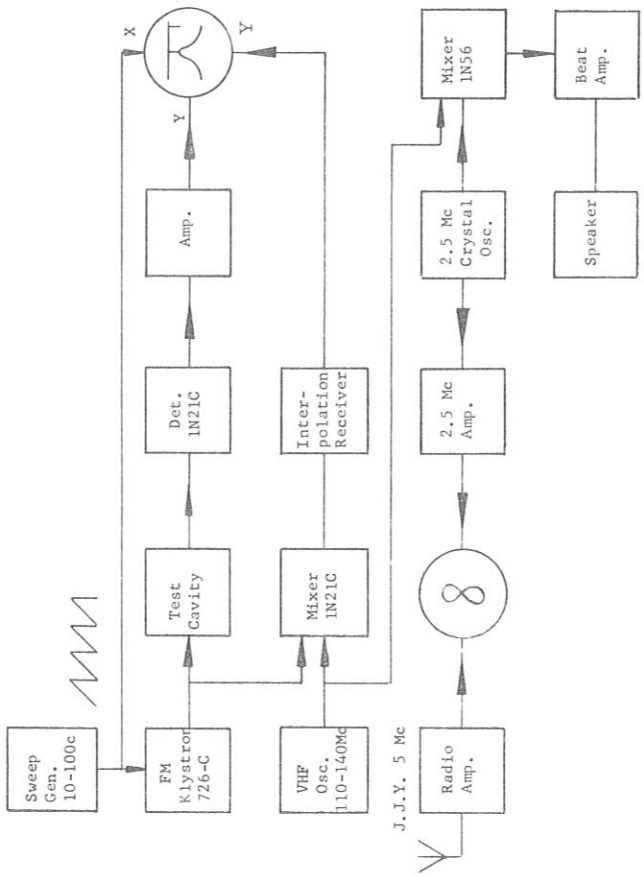
Sweep Gen. 10-100c
FM Klystron 726-C
Test Cavity
Det. 1N21C
Amp.
X
Y
Y
VHF Osc. 110-140Mc
Mixer 1N21C
Inter-polation Receiver
J.J.Y. 5 Mc
Radio Amp.
2.5 Mc Amp.
2.5 Mc Crystal Osc.
Mixer 1N56
Beat Amp.
Speaker

Fig. 5

estimate, using a perturbation calculation, shows that an accuracy of about one micron is necessary in order to keep the frequency error to less than 10^{-5}. Also the surface roughness of the finished disks is held to 0.3 microns to get high Q values.* Good rf contact between disks and cylinders is assured by a knife-edge contact with appropriate pressures leading to Q values as high as 13,000 for the S-band $2\pi/3$ mode guide.** The vacuum seal of the guide is obtained by electroforming; the gases escaping from a fabricated guide were measured to be about 2×10^{-8} $\ell\mu$/sec/cm^2. Figure 3 shows the results of a nodal-shift phase measurement for a one-meter section, giving an error of less than 2.5 degrees when plotted on a Smith chart, which is certainly the order of the experimental error in such a measuring method.

III. New Method for Measuring Performance of Guides

A simple new method for measuring the resonant frequency and the Q value of each cell has been developed.[3] A metallic plunger with an antenna probe is inserted from each end of the guide. Their positions are adjusted to be set at the center of a cell or at the center of a disk hole so as to make the distance between the two ND (D is the cell length and N is an integer) (Fig. 4). Such a position can easily be found by a slight shift from the correct position, as shown in Fig. 7, and the following description. The radio-frequency power is fed into one of the antennas and detected by the other. The radio-frequency power is frequency modulated by a sawtooth wave, and the resonance behavior is measured by comparison with a wavemeter. A block diagram of the typical electronic device used is shown in Fig. 5.

In the usual nodal-shift method with a metal plunger and a standing-wave detector, the axial electric field can take a maximum at the plunger surface. In the present method such a mode is detuned by the antenna probes, and only the mode having a zero field at the plunger surface should be excited, as shown in Fig. 6. If one moves the plunger position, the detected amplitude and the frequency of the resonance vary as shown in Fig. 7, giving the correct position of the plunger with a minimum detected power. In the nodal-shift method, the error in the measurements is caused by mismatching at the input coupler of the guide. Such an error

---

*Precise optical and matching techniques to measure and control the disk-hole shaping and the surface roughness are described also in Reference 1.

**Combined with the field measurement, the corresponding shunt impedance obtained is 59 MΩ/m.

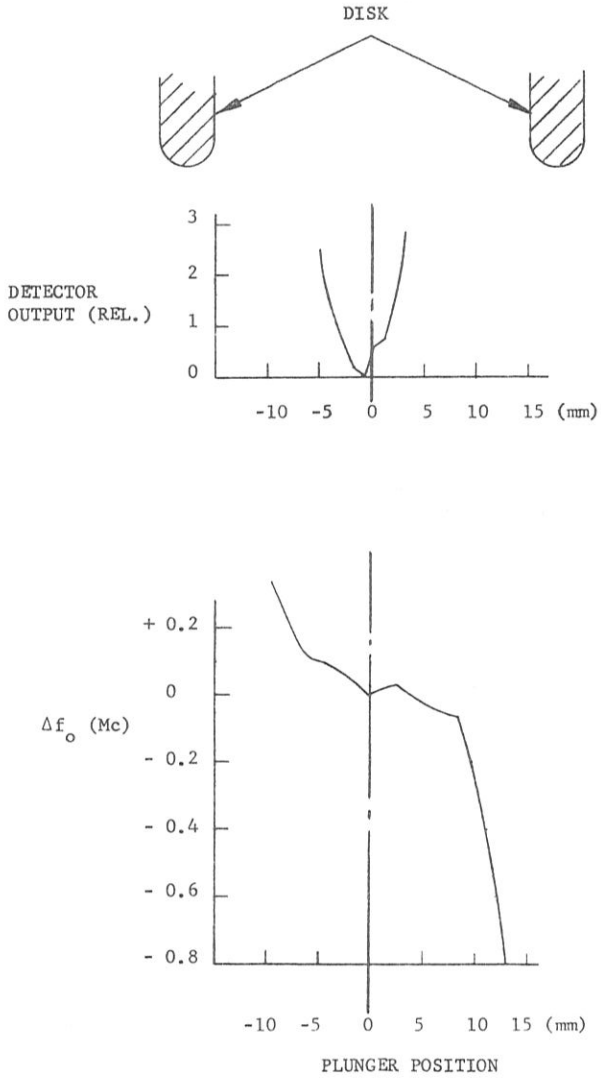
DISK
DETECTOR
OUTPUT (REL.)
3
2
1
0
-10 -5 0 5 10 15 (mm)
+ 0.2
0
- 0.2
- 0.4
- 0.6
- 0.8
Δf_o (Mc)
-10 -5 0 5 10 15 (mm)
PLUNGER POSITION

Fig. 7

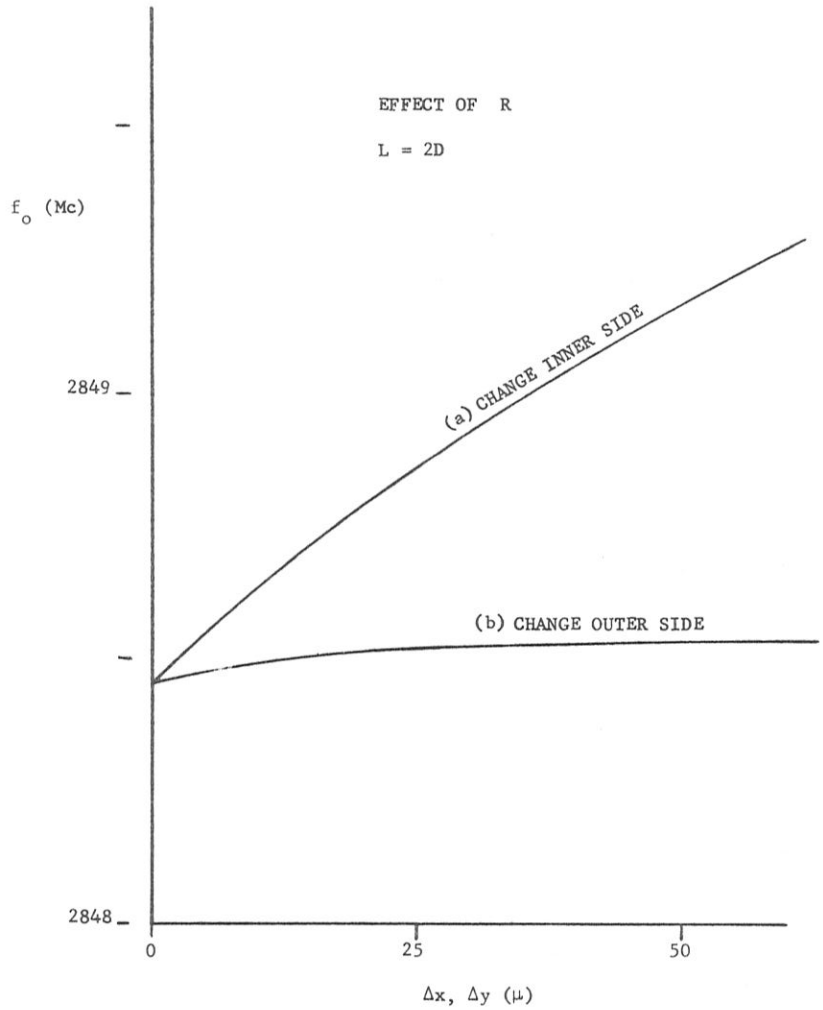
EFFECT OF R
L = 2D
f_o (Mc)
2849
2848
(a) CHANGE INNER SIDE
(b) CHANGE OUTER SIDE
0
25
50
Δx, Δy (μ)

Fig. 8

is eliminated in the present method, where the length of the antenna loops affects the frequency measurements. By an extrapolation of the results obtained for various antenna lengths, this measuring error can also be corrected.

IV. Some Typical Results of Performance Measurements

The resonant frequency of each cell fabricated by the new method is found by the above measuring method to be within $\pm$ 25 kc of the desired frequency (S-band, $2\pi/3$ mode). The corresponding phase error for a one-meter section should be 0.1° or 2×10^{-3} rad.* Some other interesting results follow:

1. The effect of hole shaping

A disk having an unsymmetrically shaped hole was used to examine the effect of hole shaping. It had a correct dimension on one half-side of the cross section and an incorrect dimension on the other side. The resonant frequency of a $\pi/2$ mode cell was measured with this disk. The disk was turned over, and measurements were done for both cases: (i) the incorrect side is inwards to the measuring cell (Fig. 8, curve a), and (ii) it is outwards (Fig. 8, curve b). The result indicates a frequency shift in case (i) but not in case (ii). Since, with the present measuring method, microwave energies are stored mainly in the inner cell and not in the half outer cells, the result obtained is quite understandable and means that we can inspect the performance of each cell separately by successive measurements. This assures also that one can make Q measurements without effects of end walls.

2. Tuning of each cell

If we had observed a big frequency error in one of the cells, we could easily make a correction by a tuning operation, observing the frequency of that cell. Some typical examples of tuning are shown in Fig. 9 where a small portion of the wall is pushed down in the usual manner, and the resonant frequency is corrected by a trial-and-error method. Also the aging effect of the deformed wall was examined over several days as shown in the right-hand side of Fig. 9.

3. Measurement of field distribution

One can also obtain the field distribution of a cavity by measuring the resonant frequency when the boundary is perturbed. An example of

*At the present stage, a guide having the total length of 3 m can be made with a similar performance.

TUNING BY PRESSURE METHOD

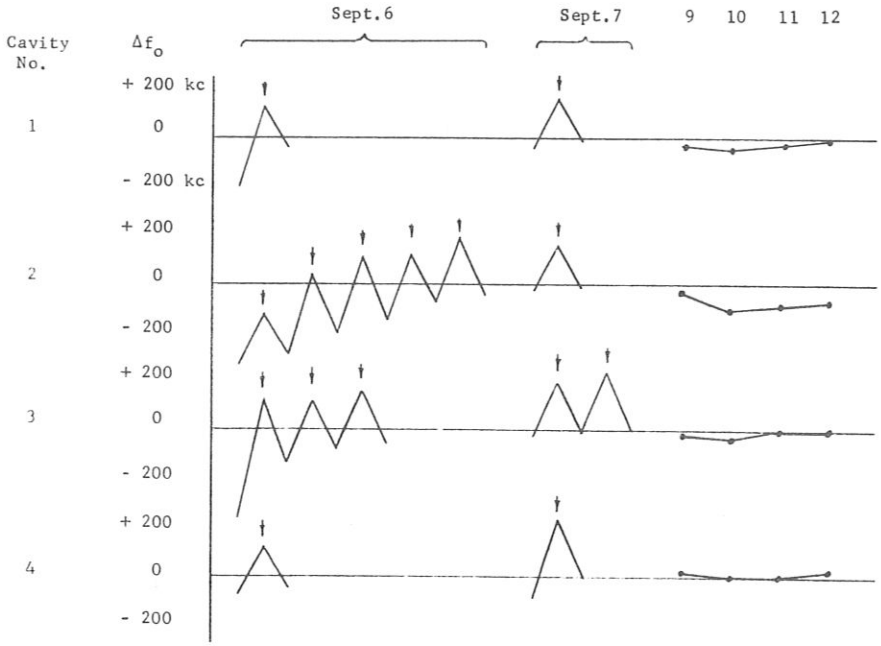

Fig. 9

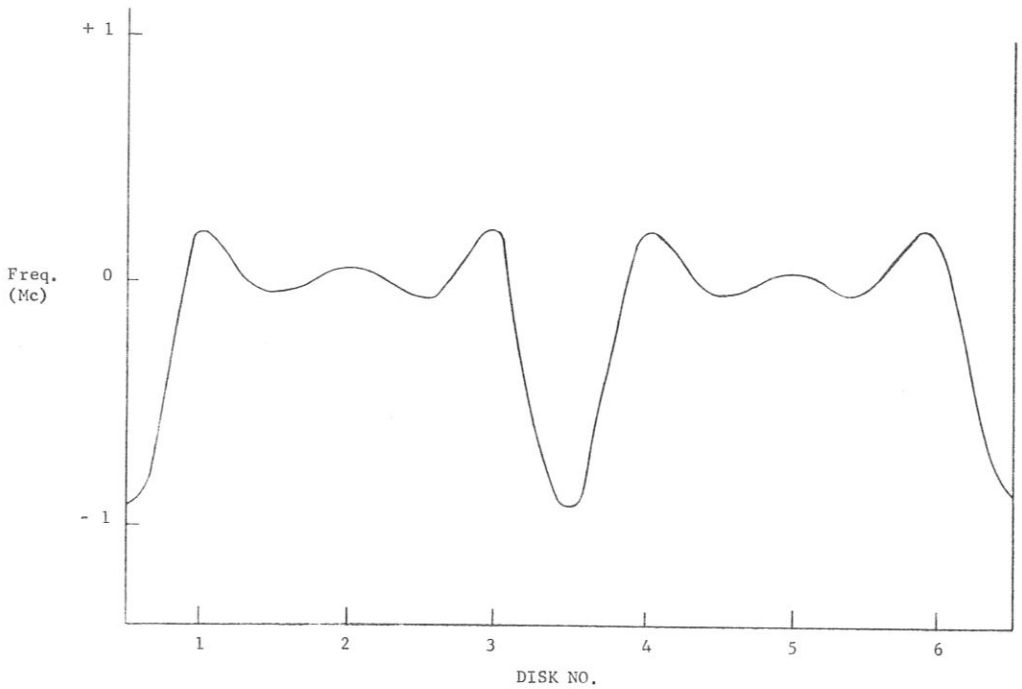

Fig. 10

the $\pi/2$ mode, in which a small teflon bead is slid down along the axis, is shown in Fig. 10.

LOEW: Do you plan to use this method and tune afterwards also, or do you plan to use only one method?

NISHIKAWA: We usually do not use the tuning, but if we have made an error, we can adjust it easily.

LOEW: Was the number 10^{-2}, for the total phase shift per cavity, expressed in radians?

NISHIKAWA: Yes, radians.

REFERENCES

1. J. Tanaka, "The Construction and Test Operation of INS Linear Electron Accelerator", J. Phys. Soc. Japan 16, 2081 (1961); J. Tanaka, T. Nishikawa, A. Miyahara et al., "On Electroforming of Disk-Loaded Waveguide for Linear Accelerators", Appl. Phys. in Japan 31, 146 (1962); J. Tanaka, T. Nishikawa, A. Miyahara, and K. Kobayashi, "Microwave Measurements on Disk-Loaded Waveguide for Electron Linear Accelerators", Internal Report of the Institute for Nuclear Study, University of Tokyo (March 1961, in Japanese).

2. "Mitsubishi Linear Accelerator Tube Manufactured by Electroforming Method with Copper Spacer", (July, 1964), issued by Mitsubishi Heavy Industries, Ltd., Nagoya, Japan.

3. T. Okada, N. Shigemura and K. Takeuchi, "A Measuring Method of Frequencies of Accelerator Guides", Report on the Meeting of the Physical Society of Japan (April 1964).

THE 500 MEV LINAC PROPOSED AS A NEW INJECTOR FOR THE AGS AT THE BROOKHAVEN NATIONAL LABORATORY

G. W. Wheeler
Yale University and Brookhaven National Laboratory

The Brookhaven National Laboratory has proposed a conversion program* to increase the intensity of the AGS to about 2×10^{13} protons per second. A major feature of this program is a new linac injector to replace the present 50 MeV machine. This paper will describe the general features of the new linac. The work presented here represents the efforts of a large group of people from BNL and Yale.

The principal characteristics of the linac are shown in Table I. The initial design goal is for 50 mA of peak current at 500 MeV. However, it is important that the linac ultimately be capable of 100 mA peak current. Consequently, the accelerator is designed for a 100 mA beam and all of the necessary power equipment and other features are included. At full energy, the energy spread will be about 0.3% and the area in transverse will be about $5\pi \times 10^{-4}$ cm-rad. Both of these figures include the effects of the estimated errors in alignment and adjustment of the accelerator.

A maximum of approximately 10 pps will be needed for injection into the AGS when it is being operated at reduced output energy. The design pulse rate for the linac is set at 30 pps which increases the cost by about 1%. This means that there can be at least 20 pps of 500 MeV protons available for use as an independent research facility should this prove desirable. Although the duty cycle of such a facility would be low, it would still have an average current capability between 200 and 500 μamp at 500 MeV which is adequate for the copious production of stopped mesons.

The preinjector will be a 750 kV Cockcroft-Walton generator. Existing proton linacs have used injection energies between 500 keV and 4 MeV. A lower limit is imposed by several considerations once the frequency of the drift tube linac is set. 1) The quadrupole field strength requirement increases and the cell length decreases as the injection energy is lowered, resulting in difficulty in installing the quadrupoles in the drift tubes. 2) As the drift tube gap decreases, the radial transit factor decreases, resulting in a worse radial distribution of field in the

---

*A Proposal for Increasing the Intensity of the Alternating Gradient Synchrotron at the Brookhaven National Laboratory, May, 1964, BNL 7956.

TABLE I

Principal Characteristics of the Proton Linac

1. Beam Energy

   (a) Maximum energy: 503 MeV.
   (b) Energy variable in steps of 5-6 MeV from 187 MeV to 503 MeV.
   (c) Energy spread at full energy: approximately $\pm$ 0.3% or or $\pm$ 1500 keV.

2. Beam Intensity

   (a) Average current: 0.3 mA or 2×10^{15} protons/sec.
   (b) Peak pulse current: 50 mA (eventually 100 mA).
   (c) Pulse length and rate: 200 μ sec, 30 pps.
   (d) Beam duty cycle: 0.6%.
   (e) The rf microstructure of the beam will consist of 0.2 nsec pulses separated by 5 nsec.
   (f) Average beam power: 150 kW.
   (g) Beam quality, area in transverse phase space, $5\pi \times 10^{-4}$ cm-rad at 500 MeV.

3. Physical Characteristics

   (a) Total length: 1200 feet.
   (b) Total peak rf power: 77 MW (at 50 mA beam current).
   (c) Preinjector: 750 kV Cockcroft-Walton generator.
   (d) Drift tube accelerator: 0.75 to 187 MeV at 201.25 Mc/sec. One cavity $\sim$ 8 m long followed by six cavities each $\sim$ 21 m long.
   (e) Loaded waveguide accelerator: 187 to 503 MeV at 805 Mc/sec: 54 cavities each 3 m long, 54 rf amplifiers.
   (f) Transverse focusing by magnetic quadrupoles.

gap which in turn can adversely affect the quality of the beam. 3) At lower injection energies, space-charge blow-up of the beam will be more serious in the space between the preinjector and the linac. The upper limit on the injection energy is set by the dc generator. The maximum voltage for an air-insulated set is about 1.25 MV and about 12 MV for a pressurized machine. Furthermore, as the injection energy is increased, the amount of phase oscillation damping is decreased which could lead to serious difficulty at the transition in structures. For a linac frequency of 200 Mc/sec, there is little to be gained by going above 750 keV, at which energy the technology is well developed.

It is planned to install two completely independent preinjector systems with a switching magnet in the drift space so that either may be used to inject into the linac. The duplication of the preinjector is necessary to insure high reliability of the linac and also will provide facilities for a polarized ion source and for ion source development.

In order to achieve accelerated beams of 50 mA and eventually 100 mA from the linac, the ion source must be capable of delivering 200 and 400 mA, respectively, with sufficiently small emittances. The present choice is a modified duoplasmatron which should be capable of 200 mA output with a minimum of development. At present, no source is clearly capable of delivering 400 mA with a sufficiently small emittance to be injectable into the linac. Thus considerable design and development will be needed on the source before the linac can deliver 100 mA.

A buncher will be used to increase the capture efficiency and particularly to concentrate the particles near the synchronous phase. This latter function is particularly important because particles which are near the boundaries of the stable region at injection may be lost at higher energies, contributing to activation of the structure or at best will emerge from the linac with poor quality and hence be of little use. Several new designs for high efficiency bunchers are now being developed, and one of these will be used.

The drift tube section of the linac will operate at 201.25 Mc/sec and will accelerate the beam to 187 MeV. The general parameters of the drift tube section are shown in Table II. The possibility of operating the drift tube section at 400 Mc/sec has been considered but abandoned for the following reasons. A pressurized preinjector at about 3 MeV would be required which would greatly complicate the preinjector design. Even at this injection energy, the design of the first cavity of the linac would be very difficult. Furthermore, the loss of damping between 750 keV and 3 MeV would be serious. However, if the new high efficiency bunchers are successful, it may prove desirable to change from 200 Mc/sec

TABLE II

General Parameters of the Drift Tube Section

Input energy (MeV)	0.75	
Output energy (MeV)	187	
Energy gain (MeV)	186	
Peak beam current (mA)	50	(100)*
Beam duty cycle (%)	0.6	
Beam pulse length (μsec)	200	
Pulse repetition rate (pps)	30	
Rf pulse length (μsec)	400	
Rf duty cycle (%)	1.2	
Operating frequency (Mc/sec)	201.25	
Wavelength (cm)	148.97	
Number of cavities	7	
Peak excitation power (MW)	13.3	
Peak beam power (MW)	9.3	(18.7)
Total peak rf power (MW)	22.6	(32)
Average excitation power (kW)	160	
Average beam power (kW)	56	(112)
Total average power (kW)	271	(384)
Total length of cavities (m)	133.7	
Total intercavity drift space (m)	5.3	
Buncher space (m)	7	
Transition drift space (m)	10	
Total length (m)	156	

*Numbers in parentheses are for a peak beam current of 100 mA.

to 400 Mc/sec at an energy near 20 MeV which could lead to a reduction in the cost of the linac.

There will be seven independent cavities containing a total of 261 drift tubes. The cavities will be of conventional copper-clad steel construction. The first cavity will be about 8 m long and will operate at a reduced gradient (about 5 MV/m) to avoid the sparking problems which have been encountered at the low energy end of some linacs. The design of this cavity is intended primarily to assure good shaping of the beam in both transverse and longitudinal phase space. A very short drift space will be used between the first and second cavities. About 30 cm is the maximum allowable distance because of the debunching of the beam. It is planned to make the vacuum envelope continuous for the two cavities. The details of the drift tube cavities are given in Table III.

The second through seventh cavities will use shaped drift tubes, and the cost will be minimized with respect to shunt impedance and the sparking limit. It is expected that the MURA method of calculating cylindrical drift tubes will be used. The length of each cavity is so chosen that the peak power required per cavity will be about 5 Mw at 100 mA of beam current which will match the capability of one power amplifier. The lengths will vary from about 24 to 19 m which is short enough to assure reasonable ease in flattening the cavities.

The drift spaces between these cavities will be about 1 m long, and matching triplets may be required in the drift space, depending on the final choice of focusing arrangement. The details of the focusing system and of the particle motion will be treated in another paper.

The final rf amplifier stages will use the RCA 7835 triode which should be capable of delivering 5 MW peak power output in this service. Thus, there will be six final stages. The power to drive these six stages and the power for the first cavity will be obtained from another 7835 stage with power splitters and phase shifters in each drive line. Each 7835 will have its own hard tube modulator and power supply.

The vacuum system, cooling and other support systems will be generally conventional. Ion pumps will be used throughout. The rough tuning of each cavity to resonance will be accomplished by temperature control.

Following the drift tube section, there will be a drift space between 5 and 10 m long before the beam enters the loaded waveguide section. Because of the debunching of the beam, it is desirable to keep this distance as short as possible, but there is a considerable amount of equipment to be

TABLE III

Summary of Drift-Tube Tables

Cavity No.	1	2	3	4	5	6	7
β_{in}	0.040	0.140	0.294	0.383	0.443	0.487	0.522
β_{out}	0.140	0.294	0.383	0.443	0.487	0.522	0.552
Energy in (Mev)	0.75	9.33	43.34	77.35	108.07	135.79	162.01
Energy out (Mev)	9.33	43.34	77.35	108.07	135.79	162.01	187.09
Energy gain (Mev)	8.58	34.01	34.01	30.72	27.72	26.22	25.08
E_{gap} (Mv/m)	5.0	8.0	12.0	12.0	12.0	12.0	12.0
Range of R_s (MΩ/m)	41.0	50.0	56/40	40/31	31/25	25/21	21/18
Excitation power (Mw)	0.38	1.69	1.67	2.06	2.26	2.50	2.70
Beam power[1] (Mw)	0.43 (0.86)	1.70 (3.40)	1.70 (3.40)	1.54 (3.07)	1.38 (2.77)	1.31 (2.62)	1.26 (2.51)
Total power (Mw)	0.81 (1.24)	3.39 (5.09)	3.37 (5.07)	3.60 (5.13)	3.64 (5.03)	3.81 (5.12)	3.96 (5.21)
Accumulated power (Mw)	0.81 (1.24)	4.20 (6.33)	7.57 (11.40)	11.17 (16.53)	14.81 (21.56)	18.62 (26.68)	22.58 (31.89)
Cavity length (m)	7.78	21.81	23.66	21.51	20.06	19.53	19.19
Cavity diameter (cm)	94.8	95.0	89.4	87.9	86.4	84.9	84.0
Range of D.T. diameter (cm)	17.6	23.9/16.5	11.74/14.4	14.4/16.4	16.6/18.3	18.6/20.0	20.1/21.4
Range of D.T. length (cm)	4.65/13.9	16.3/32.9	33.7/38.0	38.6/41.0	41.8/43.3	44.1/45.2	45.7/46.6
Range of gap (cm)	1.50/6.97	4.93/10.9	10.1/18.7	18.3/24.7	24.2/30.0	28.4/32.4	32.1/35.5
Range of g/L ($\times 10^3$)	247/332	234/248	230/329	321/375	366/401	392/417	413/432
$\Delta W/L$ (Mev/m)	1.10	1.55	1.44	1.43	1.38	1.34	1.31
$\Delta W/P_{excit.}$ (Mev/Mw)	22.5	20.1	20.4	14.9	12.2	10.5	9.4
Bore diameter (cm)	2.0	2.0 & 2.5	3.0	3.5	4.0	4.5	4.5
No. of unit cells	59	67	47	35	29	26	24
Accum. No. of full D.T.[2]	58	124	170	204	232	257	280
Drift space length[3] (m)	7.0 + 0.3	1.0	1.0	1.0	1.0	1.0	10.0
Accumulated length[3] (m)	15.1	37.9	62.6	85.1	106.1	126.7	155.8
No. of quadrupole magnets	58	66	15	9	6	5	4
No. of magnets between cavities[4]	6 + 0	3	3	3	3	3	12
Accumulated No. of magnets[4]	64	133	151	163	172	180	196

(1) Numbers in parentheses are for a peak beam current of 100 ma.

(2) There are N_{cell}-1 full D.T.'s in each cavity plus 2 half D.T.'s

(3) The buncher space preceding Cavity No. 1 is 7.0 m and the space between Cavities No. 1 and No. 2 is 0.3 m. The accumulated length is measured from the start of the buncher space to the end of the transition section following Cavity No. 7.

(4) There are two triplet lenses in the buncher space, none between Cavities No. 1 and No. 2, one lens each between Cavities No. 2 - No. 7, and three lenses in the transition section.

installed in this space. There will be one or more quadrupole triplets for matching the beam emittance from the drift tube section into the transverse acceptance of the waveguide section. It seems clear that the analysis of the beam from the drift tube section can best be done here rather than drifting the low energy beam through the entire waveguide section. Consequently, a deflecting magnet must also be installed in the drift space. Complete beam analysis equipment and a small beam stop will be provided.

The choice of frequency for the loaded waveguide section is based primarily on the longitudinal dynamics of the particles at the transition. Extensive numerical calculations have been made and lead to the conclusion that 800 Mc/sec is the highest frequency which can be used safely when the drift tube section is operated at 200 Mc/sec. In the ideal case, it would be possible to transfer the beam from a 200 Mc/sec to a 1200 Mc/sec accelerator section at about 200 MeV, without loss of beam from the phase stable region. However, when the effects of improper adjustments and a reasonable safety factor are included, it becomes clear that 800 Mc/sec is a reasonable figure.

The conventional iris-loaded waveguide is clearly a usable structure in the standing wave mode for the acceleration of protons. However, better structures have been developed, as discussed in another paper. The slotted iris structure has been chosen for the high energy section of this linac because it gives the best compromise between bandwidth, shunt impedance, ease of fabrication and other factors. The operating frequency will be 805 Mc/sec, and there will be 54 independent standing wave cavities which will accelerate the beam from 187 to 503 MeV. The general parameters of the waveguide section are given in Table IV.

The cost minimization procedure has been applied to the design and results in a rather low acceleration rate which increases from 1.67 MeV/m to 2.06 MeV/m. This leads to a maximum value of E_o of about 4.1 MV/m so that the peak fields on the surfaces should not exceed 10 MV/m which should be well below the sparking limit. Each cavity will be about 3 m or 8.5 λ long so that flattening should present no problem. The number of unit cells per cavity will vary from 30 to 22. The excitation power per cavity will be about 0.7 MW, and the total power per cavity at 100 mA will be about 1.25 MW. The energy gain per cavity varies from 5.1 to 6.4 MeV.

Each cavity will be powered by a single amplifier tube so that power splitting at high power levels will not be needed. The final amplifier tubes will be type RCA A15191 negative grid triode coaxitrons. It is believed that klystrons are not suitable for this application. Drive power for the 54 final amplifiers will be supplied by seven A15191's, each capable of driving eight finals through the appropriate power splitting networks.

TABLE IV

General Parameters of the Waveguide Section

Input energy (MeV)	187	
Output energy (MeV)	503	
Energy gain (MeV)	316	
Peak beam current (mA)	50	(100)*
Beam duty cycle (%)	0.6	
Beam pulse length (μsec)	200	
Pulse repetition rate (pps)	30	
Rf pulse length (μ sec)	250	
Rf duty cycle (%)	0.75	
Operating frequency (Mc/sec)	805.00	
Wavelength (cm)	37.241	
Number of cavities	54	
Peak excitation power (MW)	38.4	
Peak beam power (MW)	15.8	(31.6)
Total peak rf power (MW)	54.2	(70)
Average excitation power (kW)	288	
Average beam power (kW)	95	(190)
Total average power (kW)	406	(525)
Total length of cavities (m)	165	
Total intercavity drift space (m)	34	
Drift space at end of accelerator (m)	6	
Total length (m)	205	

*Numbers in parentheses are for a peak beam current of 100 mA.

These seven drivers in turn will be driven by an intermediate power amplifier employing a single A15191. Thus, there will be 62 A15191's and a single low level drive chain. Each tube will have a separate hard tube plate modulator in order to allow individual control of the field amplitube in each cavity. Phase control between cavities will be accomplished by servo-controlled phase shifters in the drive lines to the final amplifiers. By including only the final amplifier in the servo-loop, the number of elements introducing phase noise is minimized.

The frequency of the accelerator is set by a highly stabilized 805 Mc/sec oscillator, and all of the cavities are tuned to this frequency. For the drift tube section, a 201 Mc/sec oscillator is phased locked by a signal taken from the first 805 Mc/sec cavity.

The cavities will be assembled in subsections consisting of two cavities separated by a 30 cm drift space which will be used as the vacuum pumping connection. The subsections are connected by a 1 m long drift space. Transverse focusing will be accomplished by quadrupole doublets placed in each 1 m drift space.

The vacuum system will employ ion pumps throughout and will operate at a pressure below 10^{-6} Torr. The cooling system and other accelerator support equipment will be generally conventional. Because the coaxitrons are fixed tuned and have no mechanical adjustments, they will be placed directly alongside the waveguide to minimize the length of waveguide. The accelerator will be located in a shielded tunnel, separated from the support equipment by a wall which varies from about 2 to 11 feet thick.

More detailed discussion of the design of this linac is included in several other papers presented at this Conference and in the Brookhaven Proposal BNL 7956.

WROE: I would like to know why you have so much more injected current than accelerated current. It seems to me that one should be able to accelerate more than half of the current from the injector.

VAN STEENBERGEN: In the conventional bunchers which are in use now, the effective capture in the linac is less than 50%. One wishes to operate the buncher to achieve good beam quality rather than for maximum capture. Hence, it seems that 400 mA from a source is not too much to assure 100 mA of accelerated beam at the end of the linac.

WHEELER: I think it is necessary to stress the importance of beam quality in these high intensity, high energy linacs. One must not lose many particles at energies above the neutron production threshold, so that particular care must be taken when the beam is transferred from the drift tube linac to the waveguide section at about 200 MeV. We have made estimates of the radiation background and activation of the accelerator. These will be very severe if more than about 0.1% of the beam is lost. Beam quality is also most important in an injector linac in order to assure good capture by the synchrotron.

CARNE: Why do you set a field strength of 10 MV/m at 800 Mc/sec?

WHEELER: That is an estimate (see text of paper). The cost minimization procedure indicates an average acceleration rate of about 1.75 MeV/m, and from this it is estimated that the peak surface fields should not exceed 10 MV/m. I think that this figure is conservatively below the sparking limit.

WROE: Are there any parts of the preinjectors which are more unreliable than the others?

WHEELER: Particularly at these high currents, the source itself is the biggest problem. However, since the source is in the high voltage terminal, you must shut off the Cockcroft-Walton set in order to get at the source. Hence, in order to allow rapid change over to a new source, two complete preinjectors are required. These can be switched by simply changing a magnet in the buncher space. The amount of money involved is small compared to the improved operating efficiency of the linac.

THE LASL MESON FACTORY*

D. E. Nagle
Los Alamos Scientific Laboratory, University of California
Los Alamos, New Mexico

The LASL accelerator group has been engaged for the past two years in the design of a high current, medium energy (800 MeV) proton linac and associated experimental areas and equipment. A complete facility is planned, comprising experimental areas, office building, branch shops, data-handling equipment, high level radiochemistry laboratories, etc. It would have supporting it the libraries, computers, and other services presently available at Los Alamos. This facility would become a major tool for the program of research by physicists and chemists into the structure of the nucleus. The facility would be used by qualified scientists at LASL and throughout the country, with a natural emphasis on faculty and students from the Rocky Mountain and Southwest universities. It would be the only accelerator above the low energy range between the West Coast on the one hand and Chicago on the other.

Although nuclear physics is a relatively mature science, qualitative improvements in the tools of research are still giving rise to qualitative changes in our understanding of nuclear structure. We are confident that this will be true of this instrument as well.

The characteristics which make the linac especially valuable for this application are:

1) Completely extracted proton beam
2) Variable energy
3) Small radial and angular spread of the beam
4) Small energy spread of the beam
5) Complete rf debunching possible, i.e., 100% micro duty factor
6) Possibility of extending the energy range
7) Ease of servicing accelerator components
8) High rf efficiency
9) Low activation of the machine by lost beam.

Table I gives the basic parameters of the machine as a research tool.

Tables II and III give the characteristics of some of the secondary beams as calculated by A. McGuire and H. Butler.

---

*Work performed under the auspices of the U. S. Atomic Energy Commission.

A method of complete debunching of the microstructure has been studied by W. Visscher and will be discussed later in the week. It seems quite practical. This gives the linac an overall duty factor of six per cent which compares favorably with most circular machines.

Table IV shows the principal parameters of the machine. The injector is a conventional 750-keV Cockcroft-Walton with von Ardenne source and accelerating tube, followed by a prebuncher. The first 175 MeV of the linac is the Alvarez-type operating at 201.25 Mc. The present design layout of this part of the machine is given in Table V.

H. Hoyt and W. Visscher will discuss the LASL programs that do the same type of calculations. LASL is, of course, participating in the effort to see if joint designs can result in savings in hardware costs for the several linacs now proposed in this country.

Table V gives the present 200-Mc design. Figure 1 shows the acceptance fish corresponding to this design, calculated by M. Rich.

As you have heard this morning, one of the very interesting features of the last year's work has been the rapid development of new structures for the 800-Mc part of the linac. As E. Knapp said, the cloverleaf structure offers a factor of two or more improvement in shunt impedance and a factor of 10 or more in coupling over the center-coupled iris at this frequency. The other electrical properties, e.g., field patterns, higher cell modes, and tank behavior are now understood in great detail as a result of a very satisfactory agreement between theory and measurements.

The fabrication problem appears to be tractable. We regard the cloverleaf, therefore, as a practical solution to the problem of finding a better 800-Mc structure. The present design of the 800-Mc linac is based on the cloverleaf, although the side-coupled structure is an attractive alternative.

Table VI shows the basic 800-Mc layout. Forty-five (45) power amplifiers, each driving two resonant π-mode tanks of 40 cells each, are used to get to 793 MeV. The phase velocity is constant in each tank. The final amplifier tubes, RCA A15191 coaxitrons, have a design power of 1.25 MW. We have rated them at 1.0 at the tanks, including beam loading.

The problem of the phase and amplitude control of the tank voltages is an interesting and important one. Bob Jameson will discuss one system for doing this.

The choice of transition energy is a compromise between considerations of power economy and beam dynamics. Power economy considerations would argue for a transition at less than 140 MeV. However, the cost is not very sensitive to a 30 MeV change. With 40 cells per section, the computer runs predict a resonance between the radial and phase oscillation at about 130 MeV. Above 130 MeV, the curves for radial and phase oscillation diverge quite rapidly as shown in Fig. 2. The problem of fitting in focus magnets is much easier at the higher energy. Finally, the additional phase damping helps the 800-Mc fish to digest the 200-Mc fish. All of these considerations together point to 175 Mev as a suitable transition energy.

The remaining part of the talk is to show you some slides which illustrate the artist's conception of the physical appearance of the accelerator and the buildings. They are Figs. 3 through 8. Figures 9 through 11 show the 800-Mc test stand and development models of the 200-Mc and 800-Mc structures.

TABLE I

Research Characteristics of the LASL Linac

1. Average proton beam 1 mA.
2. Extraction efficiency 100%.
3. Micro duty factor can be 100% from 200-700 MeV.
4. Macro duty factor 6%.
5. Energy variable 300-800 MeV, with possibility of extending energy later.
6. Radial emittance $\cong \pi$ mr-cm.
7. Energy spread $\cong$ 0.3% (rms, with errors).
8. 800-MeV phase width, if not debunched = $\pm 15^{o}$.
9. Beam loading 26%.

TABLE II

Pion Beam Intensities

Conditions: 1 mA Proton Beam - 800 MeV
6 gm/cm^2 Target
3 x 10^{-3} Steradian Pion Channel Acceptance
$\Delta p/p$ = 0.04 - Momentum Acceptance of Pion Channel
Channel Length = 40 Ft. (Minimum $\Delta p/p$ of Channel = 0.007)

Pion Energy MeV	Positive Pion Intensity	Negative Pion Intensity
100	2.5 x 10^8/sec	4 x 10^7/sec
200	1.6 x 10^9/sec	2.8 x 10^8/sec
300	2.2 x 10^9/sec	3.1 x 10^8/sec
400	1.7 x 10^9/sec	2.8 x 10^8/sec
500	1.0 x 10^9/sec	1.6 x 10^8/sec

TABLE III

Muon Beam Intensities

Conditions: 1 mA - 800 MeV Proton Beam
30 gm/cm^2 Target
$\Omega = 10^{-2}$ Steradian = Acceptance of Pion Matching Channel
X_1 = 45 Ft. = Length of Pion Matching Channel
$\Delta p/p)_\pi$ = Momentum Acceptance of Pion Channel = 0.10
$\Delta p/p)_\mu$ = Momentum Interval of Muons Considered = 0.10
F = Probability of Muon Remaining in Channel = 0.2 for 50 Ft. Channel
= 0.1 for 100 Ft. Channel

Pion Energy MeV	Positive Pion Beam at μ Channel in	Muon Energy	Positive Muon Beam Intensity		Negative Muon Beam Intensity	
			50 Ft. Channel	100 Ft. Channel	50 Ft. Channel	100 Ft. Channel
100	9×10^9/sec	70 MeV	2×10^7/sec	--	3×10^6/sec	--
200	6×10^{10}/sec	175 MeV	2×10^9/sec	--	3×10^8/sec	--
300	8.5×10^{10}/sec	265 MeV	2×10^9/sec	1.3×10^9/sec	3×10^8/sec	2×10^8/sec
400	7×10^{10}/sec	360 MeV	1.3×10^9/sec	1.0×10^9/sec	2×10^8/sec	1.6×10^8/sec
500	5.5×10^{10}/sec	435 MeV	8.8×10^8/sec	6.9×10^8/sec	1.4×10^8/sec	1.1×10^7/sec

TABLE IV

Machine Characteristics

Proton Energy	792 million electron volts
External Average Beam Current	1000 microamperes
Length of Beam Channel	2330 feet
Radiofrequency	201.25 Mcps below 176 MeV
	805.0 Mcps above 176 MeV
Total Peak Rf Power	62 MW
Total Average Rf Power	3.8 MW
Macroscopic Duty Factor	6.0 %
Injection Energy	750 keV
Total Facility Power	33 MW
Average Beam Loading	26 %

TABLE V

200-Mc Linac Design

MURA Shape Drift Tubes

Tank	1	2	3	4	5
E in	0.75	10.76	60.50	103.1	142.2
E out	10.76	60.50	103.1	142.2	176.5
ΔE	10.01	49.74	42.6	39.1	34.3
L	9.01	30.25	29.62	30.53	30.15
$\Delta E/L$	1.11 MeV/m	1.64	1.44	1.28	1.14
Z_p	30	29	19	15	12
P_{cu}	0.47 MW	2.84	3.20	3.34	3.25
P_B	0.20	0.995	0.85	0.78	0.685
P_T	0.67	3.84	4.05	4.12	3.92
Cavity D	94 cm	90	88	86	84
DT D's	18	16-14	16	16	16
Hole d	2	2.5	3	3.5	4
R_c	2	4	4	4	4
Range G/L	.2-.3	.19-.33	.35-.42	.40-.44	.43-.46
No. Unit Cells	64	81	51	44	39
Drift Space	30.5 cm	61	61	61	
No. Quads	64	41	26	22	20
Quad Power	32 kW	16	10	8.8	8.0
Quad Cooling(B)	30 gpm	16	10	9	8
Final Power amp	2:4616's	RCA 7835	RCA 7835	RCA 7835	RCA 7835

TABLE VI

805-Mc Accelerator Summary

Section Number	1 to 90
Input Energy (MeV)	176.5
Accelerator Section Length (meters)	4.0741 to 6.2960
Quad Length $4\beta\lambda/2$ (meters)	0.4096 to 0.6302
Drift Length $4\beta\lambda/2 + 0.4$ (meters)	0.8096 to 1.0302
Accumulated Length (meters)	575.3462
Structure Power (MW)	0.387 to 0.350
Beam Power (MW)	0.113 to 0.150
$\Delta w/L$ (MeV/m)	1.389 to 1.192
Final Energy (MeV)	792.0

JOHNSTON: Did you say that in a given cavity you do change the length of the cell as beta increases?

NAGLE: No, we do not; we keep it constant until the next cavity.

JOHNSTON: Doesn't this shake the phase oscillations too badly for each proton?

NAGLE: No.

OHNUMA: I should like to ask about your choice of the final energy. You mentioned that this machine will be primarily for nuclear physics. What would be the particular advantage of getting 800 MeV instead of say 500 MeV?

NAGLE: Well, there is certainly no precise energy that you must reach. The difference between an accelerator that runs at 500 MeV and one that runs at 800 MeV is primarily in the range of high energy pion and muon beams that are available, and the range of high energy nucleon beams that are available. If you go to 500 MeV, you will not have many pions above 190 MeV because there's just not much phase space available. If you go to 800 MeV, you could have 300-350 MeV pions.

SYMON: I think it is a little amusing that the figure 800 MeV first arose because that was the natural dynamical limit for AVF cyclotrons. When we first discovered this, we were a little unhappy because it seemed one would like to go higher to get over the strange particle thresholds. We looked very hard to try to find reasons to justify building a machine at 800 MeV. Now I guess the tables are turned and the AVF cyclotrons are no longer so attractive. But this particular energy seems to be attractive still.

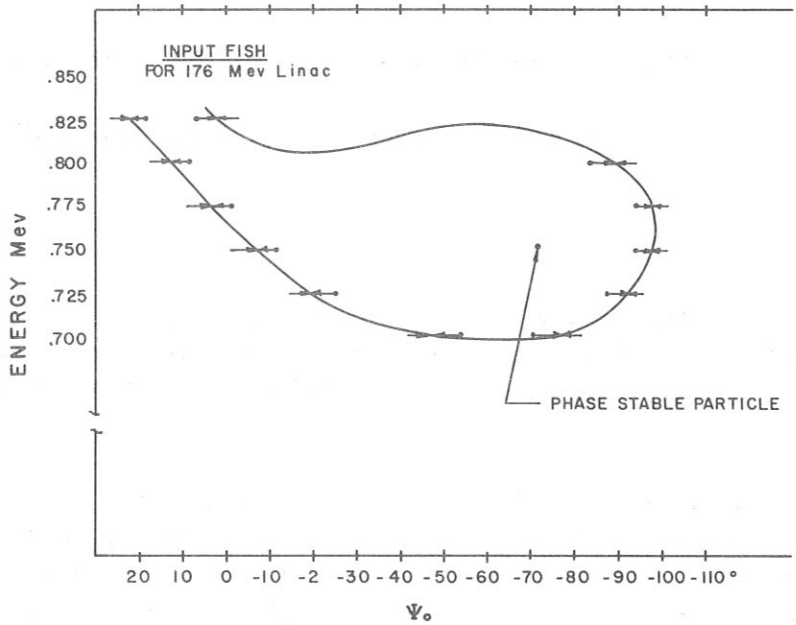
INPUT FISH
FOR 176 Mev Linac
ENERGY Mev
.850
.825
.800
.775
.750
.725
.700
PHASE STABLE PARTICLE
20 10 0 -10 -2 -30 -40 -50 -60 -70 -80 -90 -100 -110°
Ψo

Fig. 1

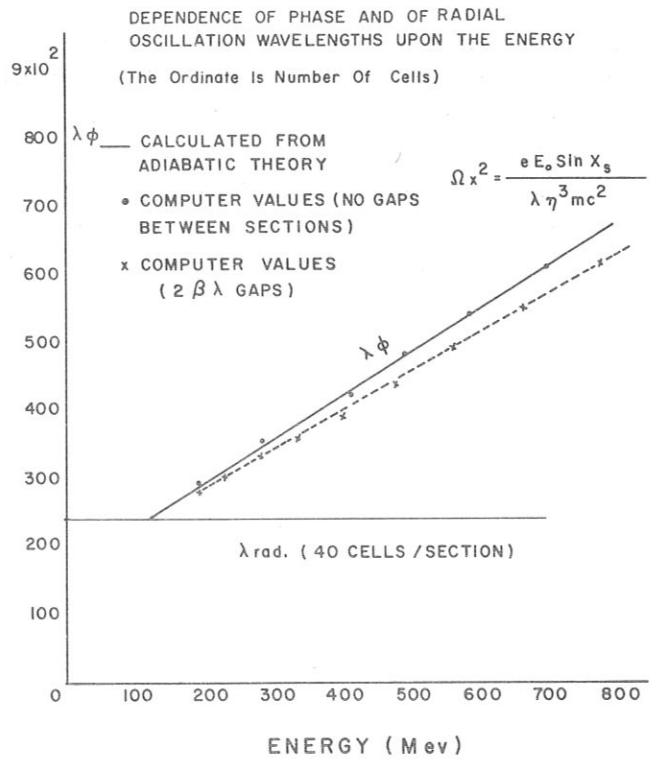
DEPENDENCE OF PHASE AND OF RADIAL
OSCILLATION WAVELENGTHS UPON THE ENERGY
(The Ordinate Is Number Of Cells)
9x10 2
λφ CALCULATED FROM
ADIABATIC THEORY
• COMPUTER VALUES (NO GAPS
BETWEEN SECTIONS)
x COMPUTER VALUES
(2 β λ GAPS)
Ωx2 = e Eo Sin Xs / λ η3 mc2
λφ
λ rad. (40 CELLS / SECTION)
800
700
600
500
400
300
200
100
0
100 200 300 400 500 600 700 800
ENERGY (Mev)

Fig. 2

MESON FACILITY SITE LAYOUT

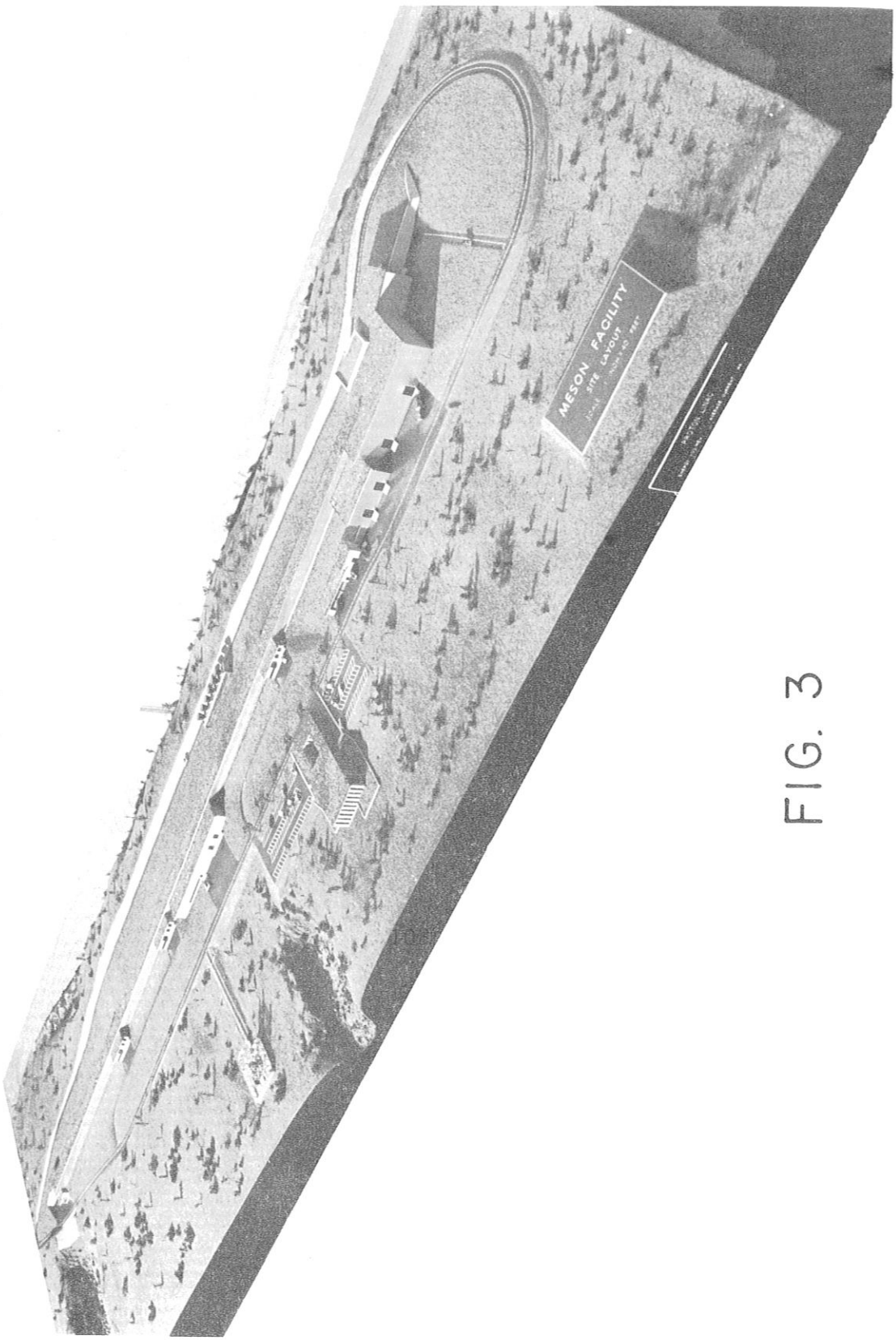

FIG. 3

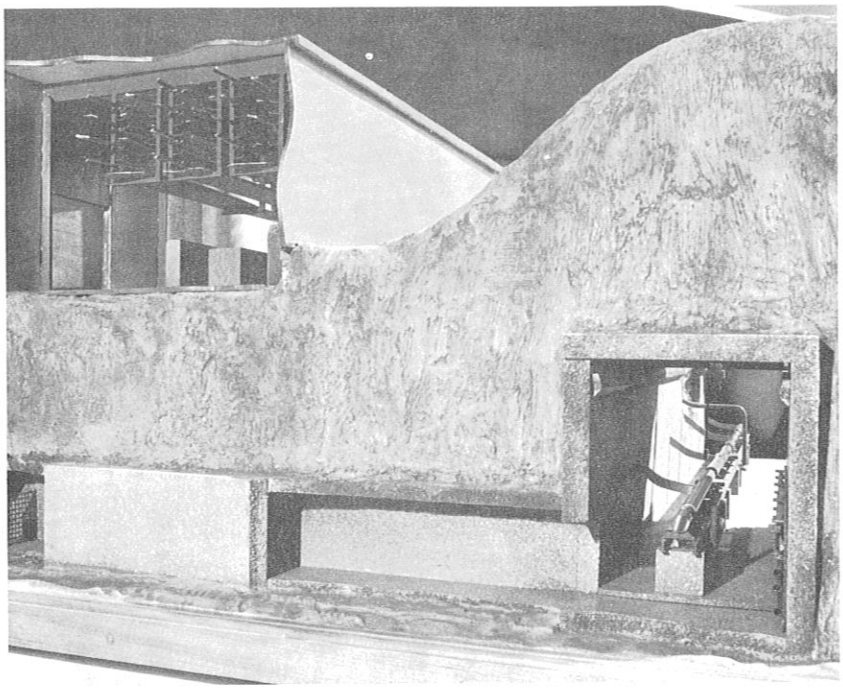

Fig. 4 ACCESS CORRIDOR AND ACCELERATOR CHANNEL

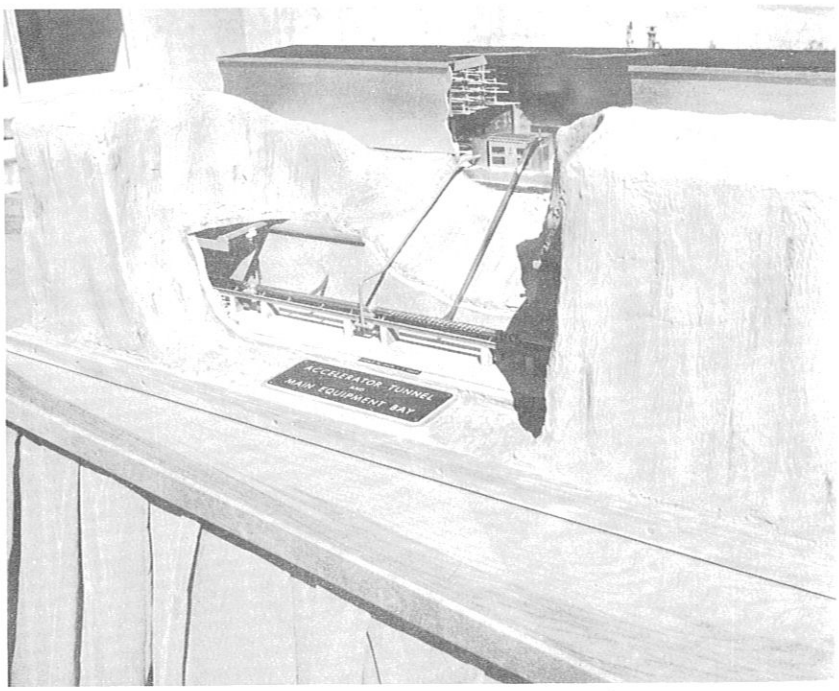

Fig. 5 ACCELERATOR CHANNEL AND MAIN EQUIPMENT AISLE

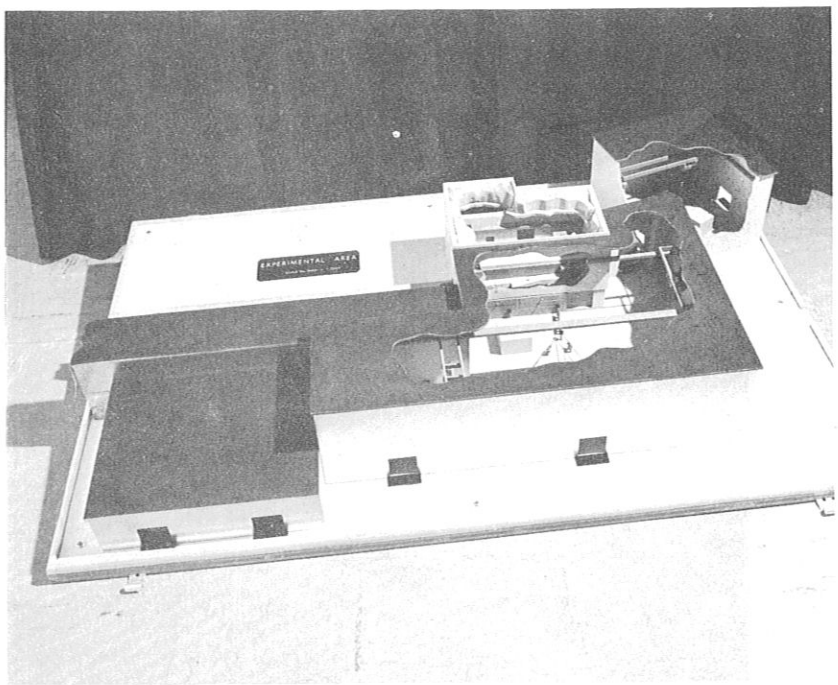

Fig. 6 EXPERIMENTAL AREA LAYOUT

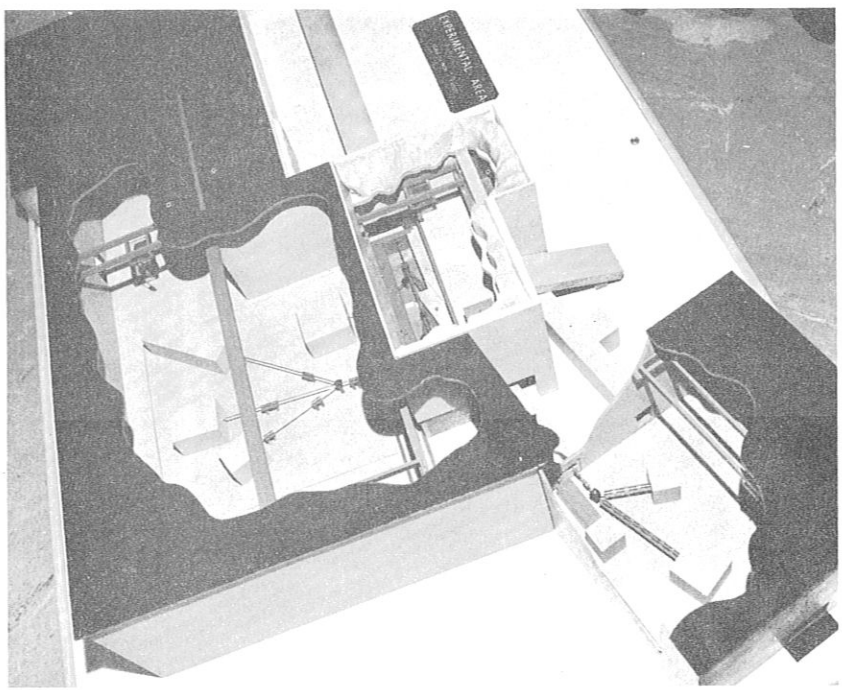

Fig. 7 EXPERIMENTAL AREA SHOWING TARGET ROOM
PION AND MUON BEAMS

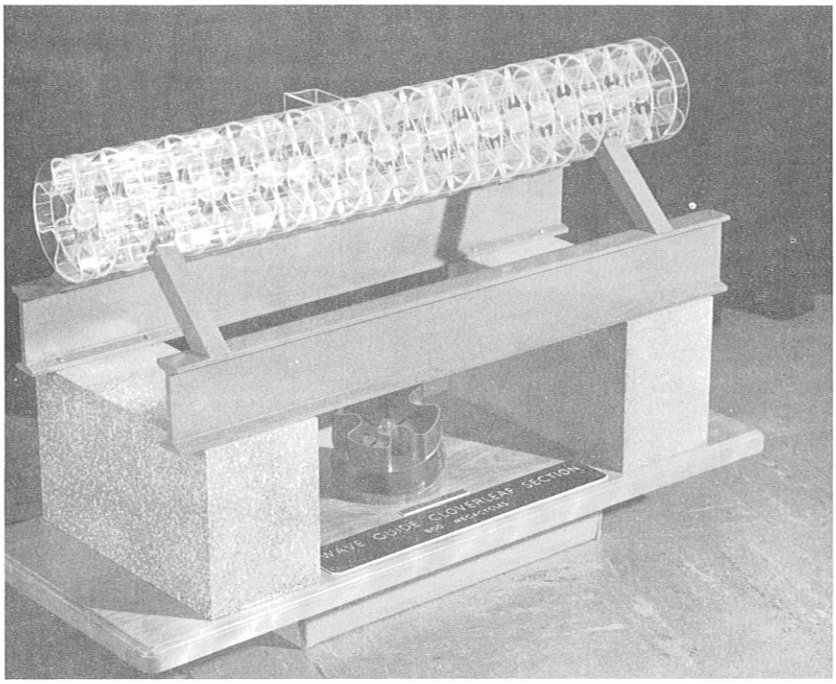

Fig. 8 PLASTIC MODEL OF WAVEGUIDE CLOVERLEAF TANK

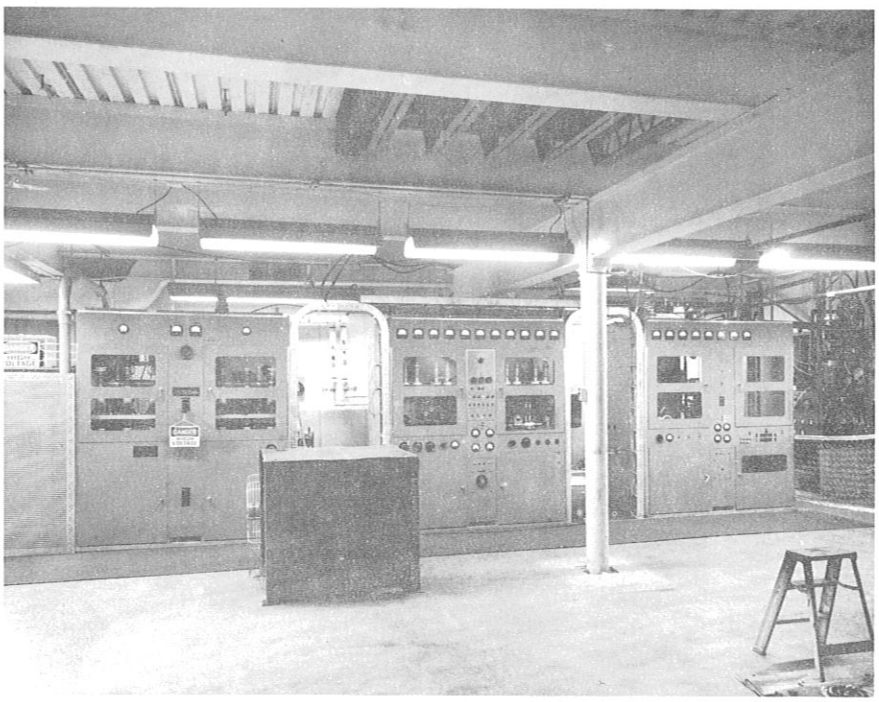

Fig. 9 800-Mc HIGH POWER TEST STAND